ULTRAFAST SPECTROSCOPY OF SEMICONDUCTOR NANOSTRUCTURES

Xiaoming Wen

Thesis submitted in fulfilment of the requirements for the degree of
Doctor of Philosophy

Centre for Atom Optics and Ultrafast Spectroscopy
Swinburne University of Technology, Melbourne, Australia

January 2007

SWINBURNE UNIVERSITY OF TECHNOLOGY

CANDIDATE DECLARATION

I certify that the thesis entitled: Ultrafast Spectroscopy of Semiconductor Nanostructures submitted for the degree of Doctor of Philosophy contains no material that has been accepted for the award of any other degree or diploma. To the best of my knowledge, this thesis contains no material previously published or written by another author, except where due reference is made in the text of the thesis. All work presented is primarily the result of my own research.

Full Name: Xiaoming Wen

Signed:..... Date:.....

To My Family

Abstract

Semiconductor nanostructures exhibit many remarkable electronic and optical properties. The key to designing and utilising semiconductor quantum structures is a physical understanding of the detailed excitation, transport and energy relaxation processes. Thus the nonequilibrium dynamics of semiconductor quantum structures have attracted extensive attention in recent years. Ultrafast spectroscopy has proven to be a versatile and powerful tool for investigating transient phenomena related to the relaxation and transport dynamics in semiconductors.

In this thesis, we report investigations into the electronic and optical properties of various semiconductor quantum systems using a variety of ultrafast techniques, including up-conversion photoluminescence, pump-probe, photon echoes and four-wave mixing. The semiconductor quantum systems studied include ZnO/ZnMgO multiple quantum wells with oxygen ion implantation, InGaAs/GaAs self-assembled quantum dots with different doping, InGaAs/InP quantum wells with proton implantation, and silicon quantum dots. The spectra of these semiconductor nanostructures range from the ultraviolet region, through the visible, to the infrared. In the UV region we investigate excitons, biexcitons and oxygen implantation effects in ZnO/ZnMgO multi-quantum wells using four-wave mixing, pump-probe and photoluminescence techniques. Using time-resolved up-conversion photoluminescence, we investigate the relaxation dynamics and state filling effect in InGaAs self-assembled quantum dots with different doping, and the implantation effect in InGaAs/InP quantum wells. Finally, we study the optical properties of silicon quantum dots using time-resolved photoluminescence and photon echo spectroscopy on various time scales, ranging from microseconds to femtoseconds.

Acknowledgments

I am very grateful to have had the opportunity to undertake PhD research that has been challenging, enjoyable and worthwhile.

First and foremost I would like to express my deep gratitude to my coordinating supervisor, Professor Peter Hannaford, who accepted me as a PhD student and offered a scholarship, and for his professional supervision and guidance. He has always given me great support throughout my PhD project. Without his consistent encouragement, I would not have been able to complete this thesis. I would also like to thank my associate supervisor, Professor Lap Van Dao, for his intellectual suggestions and helpful discussions. His comments and questions were very insightful and helpful. I am so lucky and happy to have been able to work with them. I am also particularly grateful to Dr. Jeffrey Davis for his fruitful contributions to the ZnO project.

I wish to thank Mr. Martin Lowe and Dr. James Wang for their valuable advice. I am also grateful to Mr. Craig Lincoln, Ms Tra My Do and Mr. David McDonald for their assistance and discussions. I also wish to express my thanks to the staff members and students of the Centre for Atom Optics and Ultrafast Spectroscopy for their kind help.

My special thanks go to Dr. Eunchel Cho from the University of New South Wales who provided the silicon quantum dot samples; to Ms Victoria Colman, Ms Sudah Mokkapati and Mr. Paulus Lobo Gareso from the group of Professor Chennupati Jagadish at the Australian National University who provided the ZnO/ZnMgO quantum well samples, the InGaAs quantum dot samples and the InGaAs/InP quantum well samples. They also provided the relevant data for their samples.

Finally, I reserve my deepest gratitude to my wife and daughter for their constant love and support.

List of Publications

[1] J. A. Davis, L. Van Dao, X. M. Wen, P. Hannaford, V. A. Coleman, H. H. Tan, C. Jagadish, K. Koike, S. Sasa, M. Inoue, and M. Yano, "Observation of coherent biexcitons in ZnO/ZnMgO multiple quantum wells at room temperature," *Applied Physics Letters,* vol. 89, p. 182109 (3 pages), Oct 2006.

[2] L. Van Dao, X. M. Wen, M. T. T. Do, P. Hannaford, E. C. Cho, Y. H. Cho, and Y. D. Huang, "Time-resolved and time-integrated photoluminescence analysis of state filling and quantum confinement of silicon quantum dots," *Journal of Applied Physics,* vol. 97, 013501 (5 pages), Jan 1 2005.

[3] X. M. Wen, P. Xu, and P. B. Lukins, "Characterization of enhanced emission from excimer laser treated ZnO ceramics using one- and two-photon luminescence spectroscopy and microscopy," *Journal of Luminescence,* vol. 106, pp. 1-7, Jan 2004.

[4] X. M. Wen, P. Xu, P. B. Lukins, and N. Ohno, "Confocal two-photon spectroscopy of red mercuric iodide," *Applied Physics Letters,* vol. 83, pp. 425-427, Jul 21 2003.

[5] P. L. Gareso, M. Buda, L. Fu, H. H. Tan, C. Jagadish, L. V. Dao, X. M. Wen, and P. Hannaford, "Proton irradiation-induced intermixing in $In_xGa_{1-x}As$/InP quantum wells—the effect of In composition," *Semiconductor Science and Technology,* vol. 21 pp. 1441-1446, 2006.

[6] P. Xu, X. Wen, Z. Zheng, E. Kable, G. Cox, and H. Zhu, "Two-photon optical characteristics of zinc oxide in bulk, low-dimensional and nano-forms," *Journal of Luminescence* (available online 2 January 2007).

[7] X. Wen, L. V. Dao, P. Hannaford, S. Mokkapati, H. H. Tan, C. Jagadish, "Carrier dynamics in p-type InGaAs/GaAs quantum dots", *Journal of Science Material: Material Electronics* (in press).

[8] X. Wen, J. A. Davis, L. V. Dao, P. Hannaford, V. A. Coleman, H. H. Tan, C. Jagadish, K. Koike, S. Sasa, M. Inoue, and M. Yano, "Temperature quenching variation of photoluminescence in ZnO/ZnMgO multiple quantum wells by oxygen implantation," (submitted to *Applied Physics Letters*).

[9] X. Wen, L. V. Dao and P. Hannaford, "Temperature dependence of photoluminescence in silicon quantum dots," (submitted to *Journal of Physics D: Applied Physics*).

Contents

Chapter 1 Introduction 1
1-1 Semiconductor nanostructures 1
1-2 Ultrafast spectroscopy 2
1-3 Layout of thesis 5
Chapter 2 Ultrafast Laser Spectroscopy 7
2-1 Ultrafast laser system 7
2-2 Basic theory of interaction between light and semiconductors 10
2-2-1 Density matrix 10
2-2-2 Bloch equations 13
2-3 Time-resolved photoluminescence 16
2-3-1 Direct detection technique 16
2-3-2 Up-conversion spectroscopy 16
2-4 Photon echoes 20
2-5 Pump-probe spectroscopy 23
2-4 Four-wave mixing 25
Chapter 3 Semiconductor Quantum Structures 28
3-1 General theory of semiconductors 28
3-2 Quantum confinement in semiconductors 30
3-3 Semiconductor nanostructures 33
3-4 Optical transitions in semiconductor nanostructures 34
3-4-1 Carrier-phonon scattering 36
3-4-2 Carrier-carrier scattering 37
Chapter 4 ZnO/MgZnO multiple quantum wells 38
4-1 Introduction 38
4-2 Experiments 39
4-2-1 Sample growth and oxygen implantation 39
4-2-2 Spectroscopy 41
4-3 Experimental results and discussion 42
4-3-1 Implantation effect in temperature quenching of photoluminescence 42
4-3-2 Implantation effect in thick multiple quantum wells 49
4-3-3 Observation of biexcitons in four-wave mixing experiment 51

4-3-4 Pump-probe experiment 57
4-4 Conclusions 60
Chapter 5 InGaAs Quantum Structures 61
5-1 Electron dynamics in InGaAs quantum dots 61
5-1-1 Experiment 66
5-1-2 Time-integrated photoluminescence 67
5-1-3 Time-resolved photoluminescence 71
5-2 State filling effect in InGaAs quantum dots 75
5-3 Implantation effect in InGaAs quantum wells 85
5-3-1 Experiment 87
5-3-2 Time-integrated photoluminescence 87
5-3-3 Time-resolved photoluminescence 90
5-4 Conclusions 95
Chapter 6 Silicon Quantum Dots 96
6-1 Introduction 96
6-2 Experiment 98
6-3 Photoluminescence and time-resolved photoluminescence 100
6-3-1 Photoluminescence 100
6-3-2 Time-resolved photoluminescence 105
6-3-3 Temperature dependence 109
6-3-4 Discussion 111
6-4 Transient grating experiment 114
6-4 Conclusions 118
Chapter 7 Summary and Recommendations for Further Work 119
Bibliography 122

List of Tables

Table 5-1 Rise time and decay time of the three samples from fits at 77 K.....72
Table 5-2 Rise time and decay time of the three samples from fits at room temperature.....72
Table 5-3 PL effective capture times (τ_C) and lifetimes (τ_{LW}) in the quantum well region for the reference and intermixed samples 92
Table 5-4 PL effective lifetime of carriers localized in the barrier layer for the reference and intermixed samples.....92
Table 6-1 Lifetimes for different detection wavelengths with β=0.6 107

List of Figures

Figure 2-1 The ultrafast laser system....8
Figure 2-2 Principle of OPA for extending the wavelengths through nonlinear interaction 9
Figure 2-3 Principle of up-conversion spectroscopy....17
Figure 2-4 Experimental setup of photoluminescence up-conversion....19
Figure 2-5 Two-colour three-pulse photon echoes....21
Figure 2-6 Transmission pump-probe experiment 24
Figure 2-7 Two-beam degenerative four-wave mixing....26

Figure 3-1 Density of states as a function of energy in bulk, quantum well, quantum wire and quantum dot materials. 32
Figure 3-2 Band diagram and optical transitions in a single quantum well 36

Figure 4-1 ZnO/ZnMgO multiple quantum well structure and band alignment of type I....40
Figure 4-2 Displacement profile in the oxygen implantation for various thicknesses of multiple quantum wells 41
Figure 4-3 Photoluminescence of ZnO/ZnMgO multiple quantum well samples with a well width of 2 nm (a), 3 nm (b) and 4 nm (c) 42
Figure 4-4 Photoluminescence of ZnO/ZnMgO MQW samples: reference and implanted samples....43
Figure 4-5 Temperature dependence of photoluminescence as-grown and implanted samples....44
Figure 4-6 Photoluminescence as a function of temperature, showing how with increasing temperature, the emission of the quantum wells decreases and is washed out by the band edge emission of ZnO bulk at 200 K 45
Figure 4-7 Temperature dependence of integrated intensity of the excitonic band of ZnO/ZnMgO MQWs. The inset is a fit with equation (4-2) for one of the implanted samples....46
Figure 4-8 Activation energy (circles) and peak intensity in 2 nm thick MQW samples. Ref and Ann refer to reference and annealed, respectively....48
Figure 4-9 Comparison of PL spectra for the thick reference and implanted MQW samples....50

Figure 4-10 Temperature dependence of intensities as a function of peaks a, b, c 51
Figure 4-11 Spectrally resolved FWM signal for different excitation intensities as a function of time delay between pulses.....53
Figure 4-12 Wavelength integrated FWM signal at different excitation intensities 54
Figure 4-13 Spectra of time-integrated FWM signals with one-colour excitation for a negative delay of 40 fs and different excitation intensities (a) and different time delays at high intensity (b) 55
Figure 4-14 FWM signal for two-colour excitation at 350 and 360 nm.....56
Figure 4-15 Time evolution of transmission at probe wavelength of 350 nm and 370 nm, which shows a single exponential decay 58
Figure 4-16 Comparison of the decay time between reference (squares) and implanted (circles) ZnO/ZnMgO MQWs as a function of probe wavelength for a pump wavelength 340 nm.....59

Figure 5-1 Primary difference between undoped, n-doped and p-doped QDs.....64
Figure 5-2 Structures of undoped, direct p-doped and modulation p-doped InGaAs QDs.....65
Figure 5-3 Integrated photoluminescence of InGaAs/GaAs QDs with undoped (a), direct p-doped (b) and modulation p-doped (c) sample at 77 K at low excitation.....67
Figure 5-4 Emission energy shift for charged quantum dots 68
Figure 5-5 PL spectra of undoped QDs at high excitation intensity.....69
Figure 5-6 Variation in the PL spectrum excited by a femtosecond laser at 77 K for the undoped and direct doped samples 70
Figure 5-7 Evolution of the PL for the undoped, direct doped and modulation doped with low intensity excitation of 800 nm at 77 K and 293 K.....71
Figure 5-8 Time-resolved PL spectrum of modulation p-doped InGaAs/GaAs QDs excited at various intensities of 800 nm laser at room temperature.....77
Figure 5-9 Evolution of the photoluminescence of InGaAs/GaAs modulation p-doped QDs in the ground state and excited states of the QDs.....77
Figure 5-10 PL plateau at high excitation intensity indicates saturation due to state filling.....78
Figure 5-11 Rise time and decay time as a function of excitation intensity in modulation p-doped InGaAs/GaAs QDs. 80
Figure 5-12 Numerical simulation for the rate equation for the ground state and excited state transitions corresponding to different excitation intensity.....82

Figure 5-13 Peak intensity dependence of the excitation intensity at different wavelengths for modulation p-doped InGaAs QDs....83
Figure 5-14 Saturation factor as a function of photon energy deduced from time-resolved photoluminescence for modulation p-doped InGaAs quantum dots....84
Figure 5-15 Structure of InGaAs/InP quantum wells....86
Figure 5-16 PL spectra of InGaAs QW samples at 77 K....88
Figure 5-17 The PL energy shift of lattice matched, compressively strained and tensile strained InGaAs/InP QWs as a function of implantation dose after annealing....89
Figure 5-18 Time evolution of PL of InGaAs/InP quantum wells at room temperature for the reference samples and samples implanted with $1\times10^{15} H/cm^2$ and $5\times10^{15} H/cm^2$ with lattice matched, compressively-strained and tensile-strained....91
Figure 5-19 Time evolution of PL of InP barriers at room temperature for the reference samples and samples implanted with $1\times10^{15} H/cm^2$ and $5\times10^{15} H/cm^2$ with lattice matched, compressively-strained and tensile-strained....93

Figure 6-1 The band structure of bulk silicon and possible optical transitions....97
Figure 6-2 TEM image (a) and high resolution TEM image (b) of Si quantum dots in an oxide matrix....99
Figure 6-3 PL spectra of QDs excited by the 1 kHz laser at various intensities....101
Figure 6-4 PL spectra of Si QDs excited by the 82 MHz laser at various intensities....101
Figure 6-5 Comparison of PL spectra for different excitation intensities at room temperature....102
Figure 6-6 Transmission of silicon QD sample at room temperature....103
Figure 6-7 Excitation dependence of PL intensity extracted from the PL spectra....103
Figure 6-8 Saturation factor as a function of detection wavelength. The points are the saturation factor deduced from experiment and the solid line is a linear fit....104
Figure 6-9 Time evolution of PL at various detection wavelengths as labelled....106
Figure 6-10 Evolution of the PL at various detection wavelengths (points) and fit with stretched exponential function (solid line)....107
Figure 6-11 Dependence of the degeneracy on detection energy deduced from the evolution of the PL....108

Figure 6-12 Temperature dependence of the PL spectra for an excitation wavelength of 400 nm. The S-band and F-band are clearly observed 109
Figure 6-13 PL intensity as a function of temperature at various detection wavelengths.....110
Figure 6-14 Decay time as a function of temperature for various detection wavelengths 110
Figure 6-15 Time evolution of the signal intensity at the peak of the probe pulse versus population time t_{23} for fixed t_{12}=0 for different combinations of laser wavelengths 115
Figure 6-17 Scheme for relaxation and recombination channels in Si QDs. E-excitation, R-relaxation, PL-radiative recombination of interior exciton, T-carrier trapping to the surface states, SPL-recombination of the surface trapped carriers 116

Abbreviations

BBO	β-barium borate crystal
CB	conduction band
CL	cathode luminescence
CWPL	time integrated photoluminescence
CS	compressively-strained
DFWM	degenerate four-wave mixing
FWHM	full width at half maximum
FWM	Four-wave mixing
IR	infrared
LA	longitudinal acoustic
LM	lattice-matched
LO	longitudinal optical
MBE	molecular beam epitaxy
MOCVD	metalorganic chemical vapour deposition
MQW	multiple quantum well
MSM	metal-semiconductor-metal
OPA	optical parameter amplifiers
OPO	optical parameter oscillators
PL	photoluminescence
PMT	photomultiplier tube
Q	quality factor

QD	quantum dot
QW	quantum well
QWI	quantum well intermixing
RTA	rapid thermal annealing
SAQD	self-assembled quantum dot
SFG	sum frequency generation
SHG	second harmonic generation
SRO	silicon rich oxide
TA	transverse acoustic
TEM	transmission electron microscopy
THG	third harmonic generation
TI-FWM	time-integrated four-wave mixing
TO	transverse optical
TRPL	time-resolved photoluminescence
TS	tensile strained
UV	ultraviolet
VB	valence band
WL	wetting layer

Chapter 1

Introduction

1-1 Semiconductor nanostructures

Semiconductors are the cornerstone of the modern electronics industry. They have been used extensively in communication, information and computer industries since the semiconductor transistor was invented. During the latter half of the twentieth century, miniaturization of semiconductor devices has been a major focus in order to increase integration, enhance functionality, and reduce energy consumption. As a result, semiconductor devices have evolved from millimeter-sized devices capable of manipulating electric currents into micrometer-sized devices that can handle both electricity and light. In the twenty-first century, the challenge is nanometer-sized semiconductor devices that can directly interact with individual atoms and molecules at the nanometer level [1-3].

The idea of using quantum effects in thin layers of materials has been discussed since the late 1950s [4]. Esaki and Tsu proposed the use of superlattices for the observation of negative differential resistance [5]. In 1971 Kazarinov and Suris proposed the idea of a unipolar laser using quantized subbands in a thin semiconductor quantum well and 25 years later the idea was finally implemented in a quantum cascade laser [6, 7]. The development of the AlGaAs/GaAs material system, with a nearly perfect match in lattice constant, stimulated further development of these pioneering ideas and studies of superlattices and quantum wells quickly became a mainstream of semiconductor research.

Advanced epitaxial growth techniques, such as molecular beam epitaxy and metalorganic chemical vapour deposition, have been specially developed to enable the growth of high-quality semiconductor alloys under precisely controlled conditions. Impressive progress in the fabrication of low-dimensional semiconductor structures made it possible to reduce the effective dimension from three dimensional bulk materials, to quasi-two dimensional quantum well systems, to quasi-one dimensional quantum wires, and even to quasi-zero dimensional quantum dots [8-13]. The introduction of quantum wells in the early

1970s became a turning point in the direction of electronic structure research [14]. A quantum well is a very thin layer of a semiconductor, with a small energy bandgap, sandwiched between two layers of another semiconductor with a larger energy bandgap. The motion of electrons in the quantum-well structure is confined in the growth direction if the thickness of the quantum-well layer is of the order of the de Broglie wavelength ($\lambda = h / p = h / \sqrt{3kTm_{eff}}$), where m_{eff} is the effective mass. The quantum confinement effects in such semiconductor systems with reduced space dimensions have attracted considerable attention. Especially interesting are the modified electronic and optical properties of these structures, which are controllable to a certain degree through the flexibility in the structure design. This feature makes quantum confined semiconductors very promising for possible device application in microelectronics, nonlinear optics and many other fields [15-17].

In the 1980s the interest of researchers shifted toward structures with further reduced dimensionality: quantum wires with one-dimensional confinement and quantum dots (QDs) with zero-dimensional confinement. The localization of carriers in all three dimensions breaks down the classical band structure of the continuous dispersion of energy as a function of momentum. Unlike quantum wells and quantum wires, the energy level structure of quantum dots is quite discrete. The unique discrete energy level structure of semiconductor quantum dots opens a new chapter both in fundamental physics in which they can be regarded as artificial atoms and in potential applications as devices [18-20]. Quantum dot materials have found potential application in quantum dot lasers, photon detectors, and quantum computing, etc. However, the full impact of quantum dot technology is yet to come.

1-2 Ultrafast Spectroscopy

Optical spectroscopy is a very powerful technique for investigating the electronic and vibrational properties of various systems and has provided extensive information about the properties of atoms and molecules [21]. Spectroscopy has also played an important role in semiconductor physics and application research. It is well known that linear optical spectroscopy of semiconductors has provided invaluable information on many diverse aspects of semiconductors such as electronic band structure, phonons, coupled phonon-plasma modes, single-particle excitation spectra of electrons and holes and the properties of defects, surfaces and interfaces through the techniques of absorption, reflection, luminescence and light-scattering spectroscopy. These are essential contributions to our understanding of

semiconductors, but optical spectroscopy can do much more by exploiting its additional unique strengths that make it a preferred technique for obtaining fundamental new information about the non-equilibrium, nonlinear and transport properties of semiconductors.

Optical excitation has the ability to generate non-equilibrium distributions of carriers and excitons, and optical spectroscopy provides the best means of determining such distribution functions. When these unique strengths are combined with ultrafast laser and spatial imaging techniques, ultrafast spectroscopy becomes a powerful tool for investigating a broad range of phenomena related to relaxation and transport dynamics in semiconductors. Ultrafast spectroscopy of semiconductors has been an active field of research and has led to many new insights into phenomena of fundamental importance in semiconductor physics and in many optoelectronic and electronic devices. Ultrafast coherent phenomena in semiconductor and other complex molecular systems have great potential importance but they are still essentially unexplored due to the complexity and the ultrashort time scale. Multi-dimensional coherent spectroscopy techniques, such as multiple pulse photon echoes [22-24], have become an important tool to explore ultrafast coherent dynamics.

The aim of ultrafast spectroscopy of semiconductors is to study the carrier relaxation dynamics and transport dynamics after ultrashort pulse excitation. Impressive progress has been made in ultrafast spectroscopy since the femtosecond laser was introduced. Practical applications and many of the ultrafast spectroscopy techniques have been developed or improved towards shorter time and smaller spatial and frequency resolution, and provide multi-dimensional information, such as the pump-probe technique [25], streak camera detection, up-conversion photoluminescence [26], micro-photoluminescence [20], four-wave mixing [27] and photon echoes [28, 29], etc.

The main time scale of ultrafast spectroscopy is usually femtoseconds or picoseconds, which includes four temporally overlapping regimes [30] in the carrier relaxation dynamics processes. In the coherence regime, normally within 200 fs after the laser pulse, a polarization is created by the ultrashort pulse in the semiconductor with well-defined phase relationship. Many important phenomena are included in this regime, such as exciton and biexciton dephasing, quantum beats of excitons, Bloch oscillations and so on [31]. Coherences in semiconductors have not been extensively investigated although coherence in atomic and molecular systems and defects in solids have received considerable attention. The main reason is that the scattering processes that destroy the coherence are extremely fast in semiconductors, so that femtosecond techniques are essential in order to study the coherence regime in semiconductors and their nanostructures. The destruction of the coherence created by an

ultrashort pulse by various scattering processes provides important new information about the fast dynamical processes in semiconductors [32, 33]. The newly developed spectrally resolved two-colour three-pulse photon echoes and four-wave mixing techniques are powerful tools for studying this regime.

Following the destruction of coherence through dephasing, the distribution of carriers or excitons is likely to be in non-thermal equilibrium. In this non-thermal regime, the distribution function cannot be characterized by a temperature. Some of the important scattering processes are included in this regime, such as electron-hole scattering, electron-optical phonon scattering and carrier capture in a quantum well [34-36].

The hot-carrier regime is classified as the third regime. In this regime, carrier-carrier or exciton-exciton scattering is primarily responsible for the redistribution of energy and results in a thermalized distribution function of the carrier or exciton system which can be characterized by a temperature. The temperature can be higher than the lattice temperature and may be different for the different sub-systems (electrons, holes, excitons). The thermalization times depend strongly on many factors such as carrier density and details of the scattering mechanism, such as carrier-acoustic phonon scattering, decay of optical phonons and intersubband scattering. The optical spectroscopy investigation of the dynamics of cooling of carriers to the lattice temperature can provide information about various carrier-phonon, exciton-phonon and phonon-phonon scattering processes [37-39]. In general, femtosecond time resolution is required for the above regimes. Therefore, femtosecond resolution techniques, such as up-conversion photoluminescence and pump-probe are suitable for these regimes.

In the isothermal regime all the carriers, phonons and excitons are in equilibrium with each other and can be characterized by the same temperature, the lattice temperature. Electron-hole pairs (or excitons) recombine either radiatively or non-radiatively and retune the semiconductor to the thermodynamical equilibrium. Normally this process is not shorter than hundreds of picoseconds [40, 41]. The streak camera is a very good tool for this regime with picosecond time resolution, a long scan time, high sensitivity and broad spectral response. Up-conversion and direct detection are also used for the short and long time region.

It should be emphasized that many of the processes leading to relaxation in the different regimes occur simultaneously due to the complexity in semiconductors and semiconductor quantum structures. For example, the processes of destroying coherence may also contribute to thermalization of carrier distribution functions and emission of phonons

may occur while the electrons and holes are thermalizing to a hot distribution. The non-thermal carrier distribution function created by a femtosecond pulse is influenced by dephasing of the coherent polarization during the pulse.

1-3 Layout of thesis

The key to the design and improvement of semiconductor quantum structures is a physical understanding of the detailed excitation and energy relaxation processes. Therefore, the nonequilibrium dynamics of semiconductor quantum structures has attracted considerable attention in recent years [32, 34]. Ultrafast spectroscopy provides a suitable means to investigate dynamical processes. However, many techniques of ultrafast spectroscopy are still being explored and further improvements are required for the effective application to semiconductors [28, 30].

In this thesis, we study the coherent and incoherent carrier dynamics in various semiconductor quantum systems, including ZnO/ZnMgO multiple-quantum wells with ion implantation, InGaAs /GaAs doped quantum dots, silicon quantum dots and InGaAs/InP quantum wells with proton implantation, using various ultrafast techniques, including time-resolved photoluminescence, pump-probe, FWM and photon echoes. The samples used in this study involve different wavelength regions in the ultraviolet, visible and infrared. A broad wavelength femtosecond laser system covering wavelengths ranging from the ultraviolet to the infrared region, together with a suitable detection system, is essential for the ultrafast spectroscopy.

The thesis is organized as follows. The first chapter is an introduction to ultrafast spectroscopy and applications to semiconductor nanostructures. Chapter 2 presents a brief description of the ultrafast laser system, basic density matrix theory and Bloch equations involving the interaction between light and matter based on a simple two-level system used in semiconductors carrier dynamics. The fundamental principles and general experimental setup of the ultrafast spectroscopy techniques are introduced in this chapter, including time-resolved photoluminescence, the pump-probe technique, FWM and photon echoes. We also discuss the detailed experimental setups used in our experiments.

The basic concepts of semiconductors and semiconductor quantum structures are described in chapter 3. The electronic energy band structures in quantum wells, quantum

wires and quantum dots are depicted and the corresponding state densities are compared with bulk semiconductors in this chapter.

In chapter 4 we provide the detailed experimental results and interpretation for ZnO/ZnMgO implanted multiple-quantum wells. Coherence phenomena in ZnO multiple-quantum wells, such as dephasing of excitons and biexcitons, are observed using FWM experiments. We apply integrated photoluminescence and pump-probe to detect the carrier dynamics on various time scales and to identify the effect of oxygen implantation.

Chapter 5 presents the experimental results for InGaAs/GaAs p-doped quantum dots and discusses the carrier dynamics and state filling effect. We investigate the carrier capture, carrier relaxation and recombination in different growth and doped self-assembled InGaAs/GaAs quantum dots using up-conversion photoluminescence and time-integrated photoluminescence. The state filling effect in the modulation doped self-assembled InGaAs/GaAs quantum dots is discussed and described using simplified rate equations. The detailed experimental results and interpretation for InGaAs/InP quantum wells with proton implantation are presented. In the samples with different lattice match and hence a different strain between the quantum well and the barrier, the effect of implantation on the band edge shift and luminescence efficiency and the dynamics of carrier capture and recombination is investigated using time-integrated and up-conversion photoluminescence.

The experimental results for another kind of quantum dot, silicon quantum dots, which emit in the visible region, is presented in chapter 6. We observe not only a significant state filling effect and different electron-hole recombination rates using both integrated and time-resolved luminescence spectroscopy but also the ultrafast dynamics using two-colour transient grating. A summary and suggestions for further work are briefly described in chapter 7.

Chapter 2

Ultrafast Laser Spectroscopy

2-1 The ultrafast laser system

The ultrashort pulse laser is an essential part of ultrafast spectroscopy. During the past thirty years extensive research has been performed and several important techniques have been developed to generate ultrashort laser pulses, increase the pulse energy, improve the laser mode quality and extend the range of wavelengths. In ultrafast spectroscopy, ideally the laser source should provide ultrashort pulses with the desired pulse width, a broad range of tunable wavelengths, and sufficient pulse energy with excellent mode structure and suitable repetition rate. With progress in technology, so far the femtosecond laser has become the popular ultrafast laser source which is used extensively in ultrafast spectroscopy. However, no single laser source can cover the whole range of parameters required in spectroscopy due to the broad range of wavelength applications. In order to satisfy the requirement it is necessary to set up a laser system that consists of not only a laser oscillator but also other nonlinear equipment or amplifiers [1-3].

The development of short pulse lasers started soon after the invention of the first laser. The technique of switching the quality factor (Q) of the laser oscillator cavity normally generates nanosecond pulses. Mode-locking techniques, in which many longitudinal modes are locked in phase, can generate ultrashort pulses down to femtoseconds, especially in solid-state lasers with a broad gain spectrum and a saturable absorber in the laser cavity.

Organic dye lasers, which were invented in the late 1960s and have a broad gain spectrum, are a versatile tool for spectroscopy because of their ultrashort pulse width and tunability in the visible and near infrared range. Significant progress has been made in the generation of ultrashort laser pulses since the first solid-state mode-locked laser was invented. New solid state materials with broad gain spectra have been developed and used to generate pulses shorter than 10 fs directly from the laser oscillator. Recently, these solid state lasers have practically replaced the dye laser as the basic spectroscopy source. It is possible to make

the ultrafast laser oscillator into a compact ultrafast source pumped by advanced semiconductor diode lasers.

Other laser techniques, such as amplifying and compressing the ultrashort pulses, nonlinear techniques for generating various frequencies using second harmonic generation (SHG), third harmonic generation (THG) and sum frequency generation, generating ultrashort pulses of white-light continuum by passing an intense ultrashort pulse through a liquid or solid state material, have been significantly developed. Optical parameter oscillators (OPO) and optical parameter amplifiers (OPA) pumped by ultrashort pulses have increased the tunability range. By combining the above techniques one can obtain various repetition rates, wavelengths extending from ultraviolet (UV) to infrared (IR), widths as short as a few femtosecond, and sufficient pulse energy to satisfy the requirements of ultrafast spectroscopy.

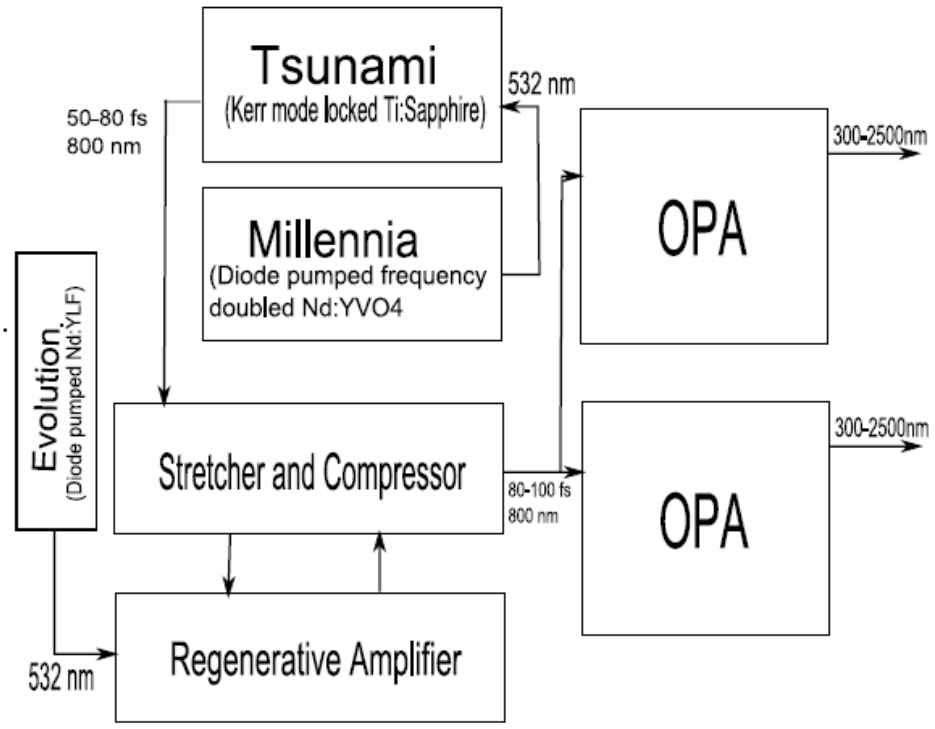

Figure 2-1 The ultrafast laser system

A typical ultrashort laser system which is used in our laboratory is shown in figure 2-1. The laser oscillator is a Kerr mode-locked Ti: Sapphire laser (Tsunami) pumped by a diode pumped frequency doubled Nd:YVO_4 532 nm laser (Millennia) and emits laser pulses tunable

around 800 nm with pulse widths 60-80 fs, repetition rate 82 MHz and average power about 700 mW. In order to generate higher peak power laser pulses, the laser pulses are seeded into the regenerative amplifier system, where the ultrashort pulses are first stretched to long pulses (about 200 ps) and then amplified to a higher pulse energy (~1 mJ), and finally compressed back to 80 fs but with much higher peak power and lower repetition rate (1 kHz). These powerful ultrashort pulses are then split into two beams to pump two independent OPAs for various wavelength applications.

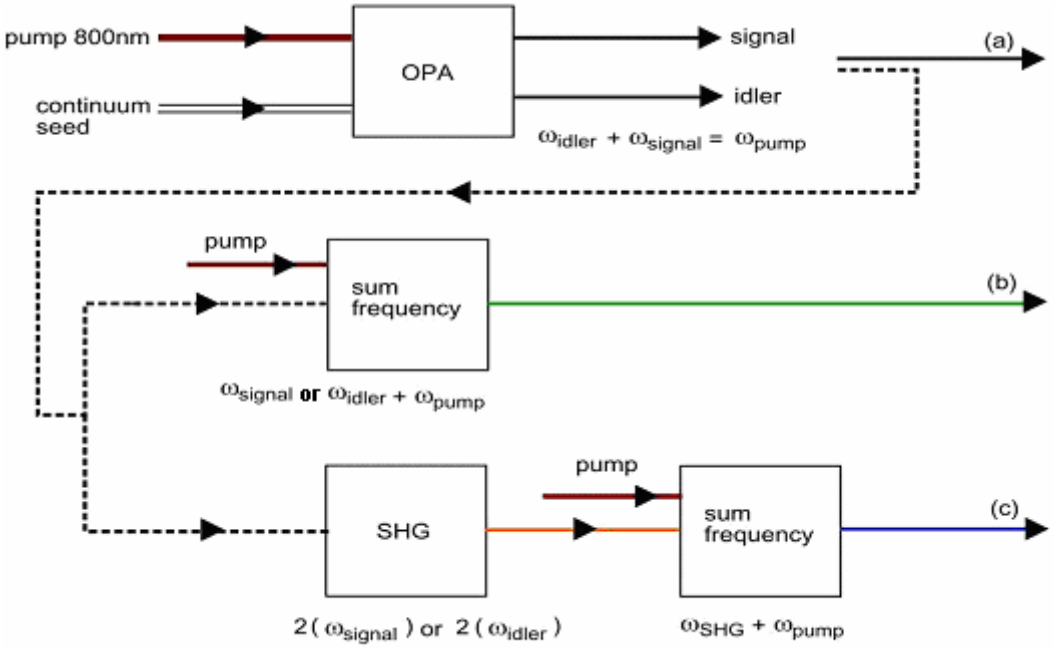

Figure 2-2 Principle of OPA for extending the wavelengths through nonlinear interaction

Figure 2-2 shows the principle of the OPA for extending the wavelengths. Firstly, 800 nm ultrashort pulses can be easily obtained as the fundamental, and 400 nm and 266 nm pulses can be obtained by nonlinear second harmonic generation (SHG 400 nm) and third harmonic generation (THG 266 nm), respectively.

A white-light continuum pulse with ultrashort width is generated as a seed by a focused pulse (800 nm) passing through a sapphire plate. Pumped by the fundamental, the

OPA oscillates and emits both signal and idler beams with perpendicular polarizations and tunable near infrared wavelengths. Then the signal and idler can mix with the fundamental to generate visible wavelengths through sum frequency generation (SFG). The second harmonic of the signal or idler can also mix with the fundamental to generate visible and ultraviolet output. Thus, the OPA system, through nonlinear techniques, can produce ultrashort pulses with wavelengths extending from the near infrared to the ultraviolet.

2-2 Basic theory of interaction between light and semiconductors

The excitation laser creates a macroscopic polarization in the system which is an ensemble average of the individual photoexcited dipole moments. During the coherence regime, which is the temporal regime immediately following the ultrashort laser excitation, the photoinduced polarizations retain a definite phase relationship with the excitation laser. This macroscopic polarization acts as a source term in Maxwell's equations, and determines the linear and nonlinear response of the system. Thus, investigation of the linear and nonlinear response of the system can provide information about the induced macroscopic polarization and hence the coherence regime.

In semiconductors, investigation of the coherence regime can provide the opportunity of learning not only about fundamental quantum mechanical processes, but also about the various scattering processes and scattering rates because the scattering processes result in the eventual loss of coherence [4]. The dephasing time of a semiconductor system is normally in the femtosecond or picosecond regime due to the extremely high scattering rate. Thus ultrafast laser spectroscopy is an essential tool for the investigation of the coherent response of transition semiconductor systems.

2-2-1 Density matrix

The coherence phenomena of atoms or molecules are generally analyzed using a simplified model, involving an ensemble of independent two-level systems. In this model, it is assumed that the excitation photon is nearly resonant with the transition between the two levels and far off-resonance with other transitions. The transitions can have different

broadening mechanisms, inhomogeneous or homogeneous. The electronic states of a semiconductor are considerably more complicated than those of atoms. However, in the simplest approximation of a semiconductor, each exciton can be considered as a two-level system and the continuum states can be considered as inhomogeneously broadened in momentum space in the absence of any interaction between the states. Thus a two-level system is still a good approximation for semiconductor systems.

In an ensemble of two-level systems, the statistical properties of the ensemble are generally described in term of the density matrix operator [6, 7]:

$$\rho = \sum_j P_j \mid \Psi_j >< \Psi_j \mid \qquad (2\text{-}1)$$

where P_j is that fraction of the system that has state vector |Ψj>. The density matrix obeys the Liouville variant of the Schrödinger equation:

$$i\hbar\dot{\rho} = [H, \rho] \qquad (2\text{-}2)$$

The Hamiltonian operator of the system can be written as:

$$H = H_0 + H_{\text{int}} + H_R \qquad (2\text{-}3)$$

The three terms H_0, H_{int}, H_R represent the Hamiltonian of an isolated two-level system, the Hamiltonian describing the interaction between the radiation field and the two-level system and the Hamiltonian describing the relaxation of the ensemble back to thermal equilibrium, respectively.

For a two-level system with a ground state with state vector |g> and energy E_g and an excited state with state vector |e> and energy E_e, the density operator matrix can be written as:

$$\rho = \begin{pmatrix} \rho_{ee} & \rho_{eg} \\ \rho_{ge} & \rho_{gg} \end{pmatrix} \qquad (2\text{-}4)$$

The diagonal elements of the density matrix represent the probability of finding the system in the two energy eigenstates, i.e., the populations of the two eigenstates ($\rho_{gg} + \rho_{ee} = 1$). The off-diagonal elements represent the coherence intrinsic to a superposition state.

The unperturbed Hamiltonian is given by

$$\mathrm{H}_0 = \begin{bmatrix} E_e & 0 \\ 0 & E_g \end{bmatrix} \tag{2-5}$$

For an electric dipole-allowed transition, one neglects the electronic quadrupole and magnetic interactions in the interaction Hamiltonian. For a monochromatic plane wave with linear polarization and assuming the rotating-wave approximation, the interaction Hamiltonian can be written as

$$\mathrm{H}_{\mathrm{int}} = \begin{bmatrix} 0 & \Delta_{eg} \\ \Delta_{eg}^{*} & 0 \end{bmatrix} \tag{2-6}$$

where

$$\Delta_{eg} = (\hbar/2)\,\chi_R \cdot \exp\{i[\mathbf{q}\bullet\mathbf{R} - (\omega \cdot t - \phi)]\} = \Delta_{ge}^{*} \tag{2-7}$$

where χ_R is the Rabi frequency at resonance $\omega = (E_e - E_g)/\hbar$ and ϕ is a phase factor.

The relaxation processes, which bring the ensemble back to thermal equilibrium, include carrier recombination, collisions with phonons and the interaction with other electronic states. Assuming the Markovian approximation and relaxation-time approximation, one approximates the relaxation Hamiltonian by

$$[H_R, \rho]_{ee} = -\rho_{ee}/T_1 \tag{2-8}$$

$$[H_R, \rho]_{eg} = -\rho_{eg}/T_2 \tag{2-9}$$

where T_1 is the lifetime of the excited state e and T_2 is the transverse relaxation time or the lifetime of the coherence.

The relaxation term describes the scattering processes between states |g>, |e> and the host medium, which lead to depopulation of the excited state with a lifetime T_1 and to dephasing of the polarizations with a phase relaxation time T_2. Dephasing consists of two contributions, the dephasing due to depopulation and a pure dephasing described by T_2^*:

$$\frac{1}{T_2} = \frac{1}{T_2^*} + \frac{1}{2T_1} \tag{2-10}$$

The scattering mechanisms leading to depopulation and dephasing have to be considered in more detail for the particular system under investigation.

2-2-2 Bloch equations

Some of the coherent phenomena may be readily seen using a simple optical Bloch equation treatment for a two-level system. Substituting $n = \rho_{ee}$, $1-n = \rho_{gg}$, and using equation (2-2) and the definitions of T_1 , T_2 , Δ_{ge} , one can get the optical Bloch equations [8]:

$$\rho = \begin{bmatrix} n & \rho_{eg} \\ \rho_{eg}^* & 1-n \end{bmatrix} \tag{2-11}$$

$$\dot{n} + n/T_1 + (i/\hbar)(\Delta_{ge}\rho_{ge}^* - \rho_{ge}\Delta_{ge}^*) = 0 \tag{2-12}$$

$$\dot{\rho}_{ge} + (i\Omega + 1/T_2)\rho_{ge} + (i/\hbar)\Delta_{ge}(1-2n) = 0 \tag{2-13}$$

where $\Omega = (E_e - E_g)/\hbar$. The optical Bloch equations are the basis for analysing coherent transient experiments in isolated two-level systems.

In the general case, it is not possible to obtain analytical solutions of the optical Bloch equations. Thus one generally resorts to expanding the density matrix into a Taylor series of the incident field amplitudes to obtain a solution to the desired order. The density n and polarization P can written as

$$n = n^{(0)} + n^{(1)} + n^{(2)} + n^{(3)} + \cdots \tag{2-14}$$

and

$$P = P^{(0)} + P^{(1)} + P^{(2)} + P^{(3)} + \cdots \tag{2-15}$$

In a semiconductor system, for the lowest conduction band and highest valence band, each state has a well-defined energy and momentum. In the simplest picture in the absence of Coulomb interaction, these continuum electron-hole states can be regarded as inhomogeneously broadened in momentum space. In this simplest approximation, one can neglect all the continuum electron-hole pair states and consider only the ground state and one excited state corresponding to the exciton bound state in which the oscillator strength is concentrated. Many of the experimental results of FWM and photon echoes have been interpreted in this simplest picture. However, the Coulomb interaction of electron-hole pairs plays an important role in semiconductor systems and leads to significant modification of this simplest picture, not only for the linear but also the nonlinear optical properties. In particular, the Coulomb interaction between excitons results in important effects, such as exciton bleaching and band-gap renormalization. A theoretical framework to deal with the many-body Coulomb interaction is known as the semiconductor Bloch equations.

In the case of a spatially homogeneous system, the density matrix is given in momentum space [9]

$$\rho_k = \begin{pmatrix} n_{ek} & P_k \\ P_k^* & n_{hk} \end{pmatrix} \tag{2-16}$$

where n_{ek} (n_{hk}) describes the nonequilibrium electron and hole distribution function of state k and P_k describes the polarization induced by the coherent pump field in the momentum state indexed by k. The coherence Hamiltonian includes the electronic system and the interaction with the radiation

$$\mathrm{H}_{coh} = \begin{pmatrix} \varepsilon_{ek}^0 & \Delta_k^0 \\ \Delta_k^{0*} & \varepsilon_{hk}^0 \end{pmatrix} - \sum_{k' \neq k} V_{kk'} \rho_{k'} \tag{2-17}$$

where $\varepsilon_{ek}^0 = (E_g/2) + \hbar^2 k^2/2m_e$ and $\varepsilon_{hk}^0 = -(E_g/2) - \hbar^2 k^2/2m_h$ are the electron and hole energy in the absence of Coulomb interaction, respectively, $\Delta_k^0 = -\mathbf{d}_k \mathbf{E}(\mathbf{R},t)$ with $\mathbf{d}_k = -e\mathbf{r}_k$ is the dipole matrix element for the electron and hole state, and E_g and m_e (m_h) are the energy bandgap and effective mass. The diagonal and off-diagonal components of the coherence Hamiltonian can be written as

$$\varepsilon_{ik} = \varepsilon_{ik}^0 - \sum_{k \neq k'} V_{k,k'} n_{ik}, \quad i = e \text{ or } h \tag{2-18}$$

$$\Delta_k = \Delta_k^0 - \sum_{k' \neq k} V_{k,k'} P_{k'} \tag{2-19}$$

Equations (2-18) and (2-19) show the primary effects of introducing the Coulomb interaction, e.g., renormalizing the electron and hole energies and the interaction strength.

Similarly, with the optical Bloch equations, substituting these expressions into the Liouville equation (2-2), the semiconductor Bloch equations can be written as

$$(\dot{P}_k + g_k P_k) + (i\Delta_k/\hbar)(1 - n_{ck} - n_{hk}) = 0 \tag{2-20}$$

$$\dot{n}_{ek} + n_{ek}/T_{1e} + (i/\hbar)(\Delta_k P_k^* - \Delta_k^* P_k) = 0 \tag{2-21}$$

$$\dot{n}_{hk} + n_{hk}/T_{1h} + (i/\hbar)(\Delta_k P_k - \Delta_k^* P_k) = 0 \tag{2-22}$$

where $g_k = \Omega_k + 1/T_2$. The semiconductor Bloch equations cannot be solved analytically in the general case. One has to resort to extensive numerical calculations to obtain results and compare with the experiments.

2-3 Time-resolved photoluminescence

2-3-1 Direct detection technique

The simplest technique of time-resolved photoluminescence (TRPL) involves the measurement of the luminescence dynamics directly using a fast response detector and broadband electronics. A typical method is to use a fast response photomultiplier tube (PMT) or photodiode connected to a broadband oscilloscope as the recording system.

In this technique the total time resolution usually depends on the response time of the detector and the bandwidth of the electronics. A normal PMT can provide up to a few nanosecond resolution and very good detection sensitivity due to its excellent signal amplification ability. For even shorter time resolution it is possible to use a fast channel-plate PMT with a time resolution of tens of picoseconds and very large dynamic range. Recently, new high-speed metal-semiconductor-metal (MSM) photodetectors have been developed and commercialized which have an impulse response below 10 ps. Essentially the spectral response of the cathode material of the PMT determines the suitable spectral range and usually the visible is the best range. The suitable detection range can be extended to the ultraviolet or infrared range with ultraviolet or infrared enhancement technology in the cathode. So the direct detection technique is a good supplement to other ultrafast techniques to cover the dynamics from milliseconds to nanoseconds.

2-3-2 Up-conversion spectroscopy

Up-conversion spectroscopy (sum frequency generation) provides a versatile means of measuring the luminescence signals with a time resolution limited by the laser pulse width and has been applied to a wide range of investigations in semiconductors.

In principle, up-conversion spectroscopy is based on the nonlinear interaction, sum frequency generation, of the optical fields between the luminescence and an ultrashort pulse, the gating pulse. Two ultrafast laser pulses are applied in the technique; one is used to excite

luminescence and the other for gating, as shown in figure 2-3. The luminescence from the sample is collected in the normal manner and focused on a nonlinear crystal, usually BBO or $LiIO_3$. The gating pulse is suitably delayed and also focused on the nonlinear crystal to overlap the luminescence spot. The angle between the two beams and the angle of the nonlinear crystal are adjusted for phase-matching so that sum frequency signal is generated at a given luminescence photon energy. The sum frequency signal is generated only when the gating pulse is present. Thus, frequency mixing acts as a light gate and provides time resolution comparable to the laser pulse width. The time resolution is limited by both the gating pulse width and group velocity dispersion in the nonlinear crystal. Thus it is necessary to use a sufficiently thin nonlinear crystal in order to reduce the group velocity dispersion.

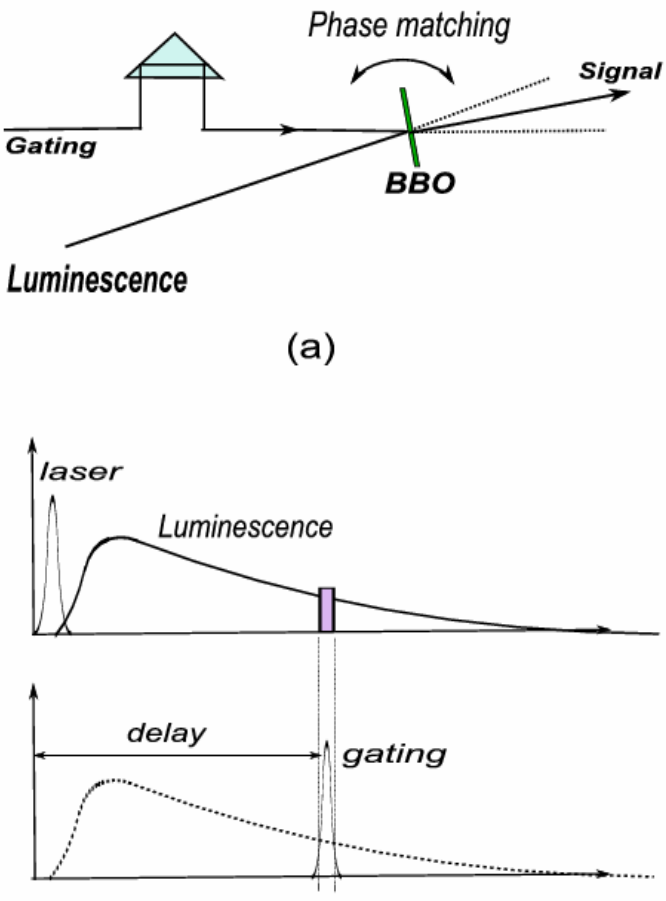

Figure 2-3 Principle of up-conversion spectroscopy. (a) The gating pulse mixes with the luminescence in the nonlinear crystal and an up-conversion signal is generated in the phase-matched direction. (b) The signal can only be generated when the gating pulse is present; thus time evolution can be obtained through scanning the gating pulse.

The sum frequency signal can be collected in a spectrometer and detected in a conventional time-integrated manner. There are various strong noise signals which are close to the up-conversion signal in space, e.g., the second harmonic signal of the gating pulse and the luminescence. Thus it is very important to minimize effectively these noise signals to acquire a clear signal with high signal-to-noise ratio. Certain techniques are usually applied to reduce the noise in space, frequency and phase dimensions, such as the use of apertures, spectral filters, a spectrometer and a lock-in amplifier. Conventionally, the time evolution of the luminescence at a given photon energy can also be obtained by scanning the relative delay between the gating pulse and the excitation pulse. The time-resolved luminescence spectrum can be obtained by fixing the time delay and scanning the angle of the nonlinear crystal and the grating in the spectrometer in a synchronized manner.

Here we briefly present the basic principles of the relevant nonlinear interaction processes and phase-matching in up-conversion spectroscopy [7, 10]. In the case of sum frequency mixing, energy conservation and momentum conservation must been satisfied for the luminescence, the gating pulse and the up-conversion signal:

$$\omega_L + \omega_G = \omega_S \tag{2-23}$$

$$\mathbf{k}_L + \mathbf{k}_G = \mathbf{k}_S \tag{2-24}$$

where $\omega_L, \omega_G, \omega_S$, $\mathbf{k_L}, \mathbf{k_G}, \mathbf{k_S}$ are the photon angular frequencies and wave vectors of the luminescence, the gating pulse and the sum frequency photon, respectively. In general, up-conversion occurs only for a narrow band of wavelengths determined by the phase matching angle.

Usually, in an up-conversion experiment, the power density of the gating pulse is several orders of magnitude higher than the luminescence signal; thus only a small fraction of the power of the gating pulse λ_G is transferred into the sum frequency signal λ_S and the power density remains approximately constant. The quantum efficiency of the up-conversion is given by (assuming there is no angular spread for either beam)

$$\eta = \frac{2\pi^2 d_{eff}^2 L^2 (P_G / A)}{c\varepsilon_0^3 \lambda_L \lambda_S n_{O-L} n_{O-G} n_S(\theta_m)} \tag{2-25}$$

where $P_{G,}$, A, d_{eff} and L are the power and area of the gating pulse, the effective nonlinear coefficient and the thickness of the nonlinear crystal, respectively; and c and ε_0 are the velocity of light and the free-space permittivity. The $n_{O\text{-}L}$ and $n_{O\text{-}G}$ denote the ordinary and extraordinary refractive indices at the wavelength of the luminescence and the gating pulse, and $n_s(\theta_m)$ is the refractive index of the up-conversion signal at the phase-matching angle θ_m given by

$$n_S(\theta_m) = n_{O-L}\frac{\lambda_S}{\lambda_L} + n_{O-G}\frac{\lambda_S}{\lambda_G} \tag{2-26}$$

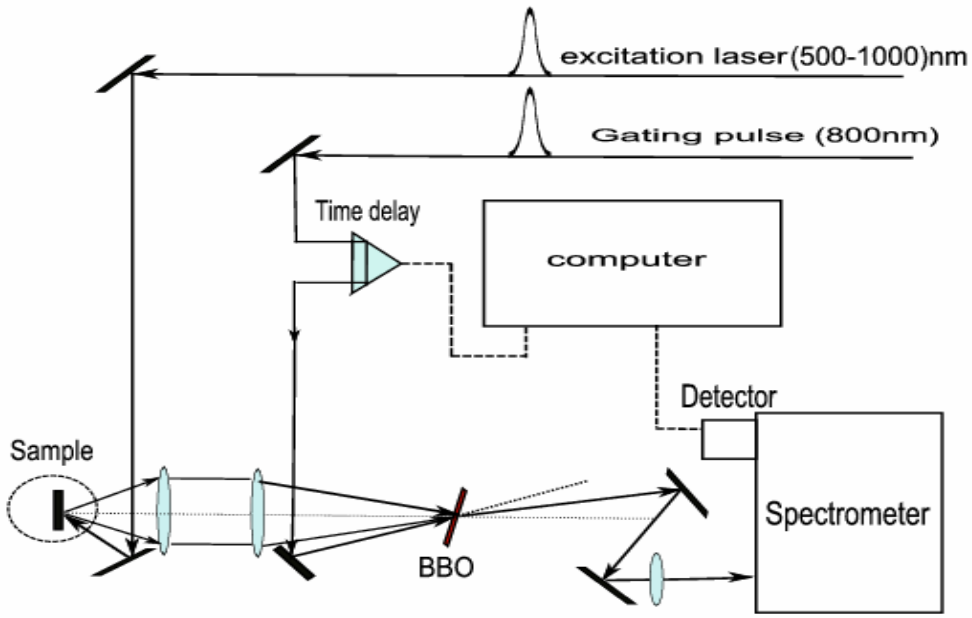

Figure 2-4 Experimental setup of photoluminescence up-conversion

The experimental setup in our laboratory is shown in figure 2-4. The sample is excited by an ultrashort pulse of duration 80 fs with tunable wavelength, pulse energy 1-10 μJ and repetition rate 1 kHz. The sample is mounted in a closed-cycle helium cryostat with a variable temperature ranging from 20-300 K. The photoluminescence from the sample is collected in a back-scattering geometry and mixed in a nonlinear β-barium borate (BBO) crystal with a

variable delayed gating pulse (800 nm, 80 fs, 20 μJ) to generate a sum-frequency mixing signal. This signal is focused into a monochromator and detected with a photomultiplier tube coupled to a lock-in amplifier system. The up-conversion system has a time resolution of 150 fs and a spectral resolution of 2 nm.

2-4 Photon echoes

Multidimensional femtosecond spectroscopy is becoming a major focus in studies of ultrafast dynamical processes in complex molecular systems [4, 11]. Multiple-pulse nonlinear coherent techniques probe correlations between the electric fields generated by the femtosecond pulses in the phase-matching directions and allow detailed dynamical and spectroscopic information to be extracted in the presence of strong inhomogeneous broadening. Photon echo spectroscopy, which is a potentially powerful multidimensional technique, involves the application of two or three femtosecond pulses with independently controllable time delays. The spreading of the information over more than one dimension enables one to unravel and extract complex dynamical and spectroscopic information, such as population relaxation times, dephasing times (homogeneous broadening), inhomogeneous broadening, and vibrational structure of transient species [4, 12]. Although significant progress has been made in recent years, considerable experimental and theoretical effort will be required in order to develop it into a routine structural and dynamical tool.

In the 2-colour 3-pulse photon echoes technique, as shown in figure 2-5, two femtosecond pulses with wave vectors $\mathbf{k_1}$, $\mathbf{k_2}$, wavelength $\lambda_1 = \lambda_2$ and separated by t_{12}, and a third pulse with wave vector $\mathbf{k_3}$ and wavelength λ_3, illuminate the sample and create photon echo signals at times near t_{12} after the third pulse in the phase-matching directions $\mathbf{k_4 = -k_1 + k_2 + k_3}$, $\mathbf{k_5 = -k_2 + k_1 + k_3}$ and $\mathbf{k_6 = -k_3 + k_1 + k_2}$. The photon echo signals ($\mathbf{k_4}$, $\mathbf{k_5}$ and $\mathbf{k_6}$) are detected simultaneously in two or three spectrometers equipped with CCD detectors and the spectra of the photon echo signals are recorded as a function of the time delays t_{12} or t_{23} and the wavelengths λ_1 and λ_2. Spectral analysis of the photon echo signals yields detailed information about the temporal evolution of the amplitude of the nonlinear polarization induced in the sample by the three pulses. Suitable selection of the laser wavelengths allows different sets of energy levels and the dynamics to be investigated.

Applying the optical Bloch equations in this situation and assuming the pulse duration is much shorter than the population time T_1 and the dephasing time T_2, the density matrix at time t after the third pulse may be determined from a product of the interaction and evolution matrices [5, 14]:

$$\boldsymbol{\rho}(t) = \mathbf{Y}(t)\mathbf{X}(A_3)\mathbf{Y}(t_{23})\mathbf{X}(A_2)\mathbf{Y}(t_{12})\mathbf{X}(A_1)\boldsymbol{\rho}(0) \qquad (2\text{-}27)$$

where the **X**(A) represent the time evolution during interaction with the optical pulses of area $A = \int \chi_R \, dt$, and the Y(t) represent the free evolution during the time intervals between the interactions. The polarization induced by the femtosecond laser sequences in the sample can be obtained by solving equation (2-27) [14]:

$$P(t) = \mu_{ge} N[\rho_{eg(t)} + \rho_{ge}(t)] \propto P_1^{(1)}(t) + P_2^{(3)}(t, t_{12}) + P_3^{(3)}(t, t_{12}, t_{23}) \qquad (2\text{-}28)$$

where N is the number of molecules per unit volume.

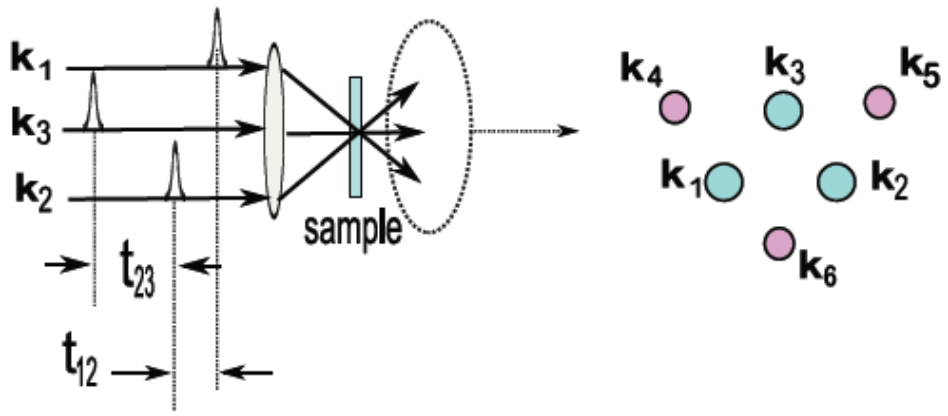

Phase matching directions

$$\mathbf{k}_4 = -\mathbf{k}_1 + \mathbf{k}_2 + \mathbf{k}_3$$
$$\mathbf{k}_5 = -\mathbf{k}_2 + \mathbf{k}_1 + \mathbf{k}_3$$
$$\mathbf{k}_6 = -\mathbf{k}_3 + \mathbf{k}_1 + \mathbf{k}_2$$

Figure 2-5 Two-colour three-pulse photon echoes

The first-order polarization in (2-28), which corresponds to single pulse excitation, is given by:

$$P_1^{(1)}(t) \propto \int d\omega\, G(\omega) \exp(-i\omega t) \exp(-\gamma_{ge} t) \sin A_1 \exp(-i\mathbf{k_1} \cdot \mathbf{r}) \tag{2-29}$$

For pure homogeneous broadening $G(\omega) = \delta(\omega - \omega_{ge})$ the polarization decays with the dephasing time $\gamma_{ge}^{-1} = T_2$. In the presence of inhomogeneous broadening, G(ω), the range of molecular environments in the ensemble can lead to rapid dephasing of the polarization due to interference between the different resonance frequencies, and information about T_2 is essentially lost.

The third-order polarization in (2-28) for the case of two-pulse excitation is given by:

$$\begin{aligned} P_2^{(3)}(t, t_{12}) \propto \int\ & d\omega\, G(\omega) \exp[(-i\omega(t - t_{12}) - \gamma_{ge}(t + t_{12})] \\ & \sin A_1 \sin^2(A_2/2) \exp[-i(-\mathbf{k_1} + 2\mathbf{k}_2) \cdot \mathbf{r}] \end{aligned} \tag{2-30}$$

in the phase matching direction $-\mathbf{k_1} + 2\mathbf{k}_2$ for the pulse sequence (1, 2), with corresponding terms for the sequences (2, 1), (2, 3), (3, 2) etc. In the presence of inhomogeneous broadening the interference term $G(\omega)\exp[(-i\omega(t - t_{12})]$ vanishes at time $t = t_{12}$, and a photon echo signal appears at delay times near $t = t_{12}$. The amplitude of the 2-pulse photon echo is proportional to $\exp(-\gamma_{ge} t_{12})$, allowing a determination of the dephasing time $\gamma_{ge}^{-1} = T_2$.

The third-order polarization in (2-28) for the case of three-pulse excitation is given by:

$$\begin{aligned} P_3^{(3)}(t, t_{12}, t_{23}) \propto \int\ & d\omega\, G(\omega) \exp[(-i\omega(t - t_{12}) - \gamma_{ge}(t + t_{12})] \\ & \exp(-\gamma_e t_{23}) \sin A_1 \sin A_2 \sin A_3 \exp[-i(-\mathbf{k_1} + \mathbf{k}_2 + \mathbf{k}_3) \cdot \mathbf{r}] \end{aligned} \tag{2-31}$$

for the phase matching direction $-\mathbf{k}_1 + \mathbf{k}_2 + \mathbf{k}_3$ for the pulse sequence (1, 2, 3) with corresponding terms for the other pulse sequences. In the presence of inhomogeneous broadening, the interference term $G(\omega)\exp[(-i\omega(t - t_{12}))]$ vanishes at time $t = t_{12}$, and a 3-pulse photon echo signal appears at delay times near $t = t_{12}$. The amplitude of the 3-pulse

photon echo is proportional to $\exp(-2\gamma_{ge}t_{12})\exp(-\gamma_e t_{23})$, allowing the determination of both the dephasing time $\gamma_{ge}^{-1} = T_2$ and the population time $\gamma_e^{-1} = T_1$.

Based on the above treatment, a simplified physical description of 3-pulse photon echoes can be obtained [5, 14, 16]. The first π/2 pulse prepares the inhomogeneously broadened ensemble in a superposition of the states |g> and |e> to create optical coherences ρ_{eg} and ρ_{ge}. After the system has evolved for time t_{12} the second π/2 pulse creates population in the excited state ρ_{ee} or a second-order population change in the ground state ρ_{gg} . The populations ρ_{ee} and ρ_{gg} store the optical coherence and phase information in the excited and ground states. After a further evolution time t_{23} the third π/2 pulse converts the populations back into optical coherences, in which the phase of the frequency components are now opposite to those of the initial optical coherences. For an inhomogeneously broadened ensemble, this rephasing leads to the generation of a photon echo signal at time $t = t_{12}$ after the third pulse in the phase matching direction $\mathbf{k_4 = -k_1 + k_2 + k_3}$.

2-5 Pump-probe spectroscopy

This is the most common form of ultrafast spectroscopy and various pump-probe spectroscopy techniques have been developed based on the different techniques of linear spectroscopy. Here we briefly describe the experiment used in our laboratory as shown in figure 2-6. Two ultrashort pulses, a pump and a probe, come from the signal and fundamental beam of the OPA. The semiconductor sample under investigation is excited by the pump pulse and the changes induced in the sample are probed by a synchronized white light continuum pulse created by the second laser pulse. The continuum pulse is suitably delayed with respect to the pump pulse by introducing an optical delay in its path. Some property related to the probe, such as reflectivity, absorption, Raman scattering or luminescence, is then detected to investigate the change in the sample induced by the pump pulse.

One of the simplest kinds of pump-probe spectroscopies is the measurement of the transmission of the probe. The probe is typically much weaker than the pump and the spot on the sample is smaller than that of pump so that the probe area experiences a uniform photoexcited density. As shown in figure 2-6 for a transmission pump-probe spectroscopy

setup, one generally measures the change of the transmitted probe pulse energy induced by the pump pulse as a function of the time delay between the two pulses. The data is normally expressed in the form of the normalized differential transmission given by $\Delta T / T_0 = [T(t) - T_0] / T_0$, where $\Delta T(t) = T(t) - T_0$ is the change in transmission induced by the pump, T and T_0 are the transmission of the probe in the presence and absence of the pump, respectively. For single wavelength detection, normally a lock-in amplifier is used. Spectrally resolved pump-probe can be obtained by using an ultrashort white light continuum pulse as the probe and a detection system with a CCD detector and a spectrometer.

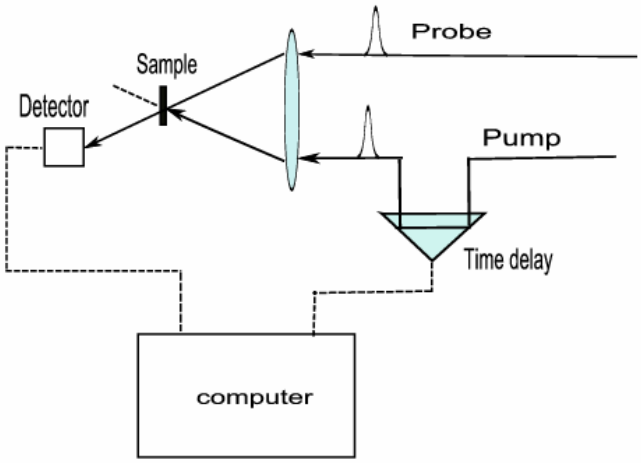

Figure 2-6 Transmission pump-probe experiment

The dynamics in a pump-probe transmission experiment are determined not only by the coherent response but also by the incoherent response of the system. If the time scale is shorter than or comparable to the dephasing times of the system, one must use the semiconductor Bloch equations to calculate the third-order nonlinear polarization in the probe direction. The probe signal can be regarded as the diffracted signal in the probe direction ($\mathbf{k}_{probe} = \mathbf{k}_1 + \mathbf{k}_2 - \mathbf{k}_1 = \mathbf{k}_2$). However, if the time scale is much longer than the dephasing times of the system, the coherent effects can be neglected and the solution is relatively simple; one can ignore the off-diagonal components of the density matrix and just consider the diagonal components corresponding to the populations of the states.

Normally the incoherent effects can be divided into two classes. The first class includes many-body effects [17-20] which result in a change of the energy band structure

(band-gap renormalization or a change of the exciton binding energy), broadening of the energy levels or a change in the various matrix elements. The many-body effects depend strongly on the photoexcited density and the nature of the system being investigated. The second class encompasses occupation effects that result in a change in the optical properties or transition rates.

Under certain experimental conditions, it may be a good approximation to assume that many-body effects depend only on the photoexcited density and are independent of time for the time scale of interest. Furthermore, the change in the matrix element for interband transitions may be small enough to be neglected for certain spectral regions. Then the change of the absorption coefficient at photon energy $h\nu$ is given by

$$\Delta\alpha(h\nu) = (1 - f_e - f_h)\,\alpha_0(h\nu) \tag{2-32}$$

where f_e and f_h are the photoexcited electron and hole distribution functions, and $\alpha_0(h\nu)$ is the absorption coefficient of the unexcited semiconductor. If the absorption is sufficiently small, the differential transmission spectrum DTS is

$$DTS(h\nu) = [T(h\nu) - T_0(h\nu)]/T_0(h\nu) = -\Delta\alpha(h\nu)\,d \tag{2-33}$$

where d is the thickness of the sample. With these simplifications, the results can be simply related to the distribution functions of electrons and holes as a function of time.

2-6 Four-wave mixing

There are various configurations for the four-wave mixing (FWM) experimental setup. In the simplest form, i.e., the two-beam degenerative four-wave mixing (DFWM) (shown in figure 2-7), the pump beam ($\mathbf{k}_1$) generates a coherent polarization in the sample. After a time delay τ_d the probe beam ($\mathbf{k}_2$) arrives at the sample. If the time delay is smaller than the dephasing time of the polarization, an interference grating is produced from which $\mathbf{k}_2$ can be self-diffracted in the phase-matched direction $\mathbf{k}_4 = 2\mathbf{k}_2 - \mathbf{k}_1$. The diffracted signal can be measured as a function of τ_d in both reflection and transmission geometries.

In three-beam degenerative FWM, three beams excite the sample along $\mathbf{k}_1$, $\mathbf{k}_2$, $\mathbf{k}_3$ at times t_1, t_2, t_3. The diffracted signal in the phase matching direction $\mathbf{k} = \mathbf{k}_3 + \mathbf{k}_2 - \mathbf{k}_1$ is measured as a function of the various time delays to obtain additional information about the sample. Compared with two-beam DFWM, three-beam DFWM has greater versatility because of the possibility to control individually the parameters of the three beams; so that it is possible to obtain more information. For example, in a transient grating experiment ($t_{21} = t_2 - t_1 = 0$) the diffracted signal is measured as a function of time delay t_{32} to provide information on the population decay time of the sample.

Additional information may be obtained from the temporal evolution of the diffracted pulse using time-resolved FWM. In this technique one needs to use a streak camera or up-conversion techniques to obtain the temporal profile of the diffracted signal. Other options for FWM setup include various combinations of the polarizations for the excitation beams and reflection geometry. Different combinations of linear polarizations or circular polarizations can be employed in the FWM experiments to obtain different information because the optical transitions are governed by various selection rules. The reflection geometry is particularly valuable for samples which are strongly absorptive at the detection wavelengths. The diffracted signal in a FWM experiment measures only the coherent response of the semiconductor.

In the simple two-beam, DFWM experiment, the temporal evolution of the FWM signal, $S^{(3)}_{221^*}(t)$, which results from diffraction of pulse $\mathbf{k}_2$ from the grating generated by

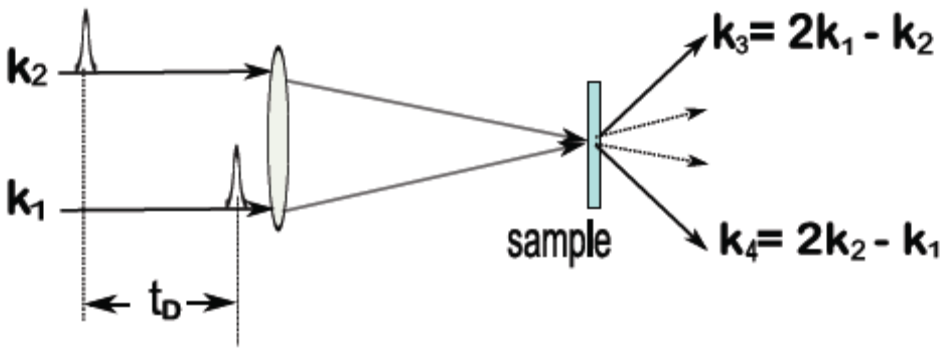

Figure 2-7 Four-wave mixing

pulses $\mathbf{k}_1$ and $\mathbf{k}_2$ in the $\mathbf{k}_4 = \mathbf{2k_2 - k_1}$ direction, can be expressed as [21]

$$S^{(3)}_{221^*}(t) = \left| P^{(3)}_{221^*} \right|^2 \tag{2-34}$$

where $P^{(3)}_{221^*}$ represents the third-order polarization. The time-integrated four wave mixing signal as a function of time delay is then

$$I^{(3)}_{221^*}(\tau_D) = \int_{-\infty}^{\infty} S^{(3)}_{221^*}(t)\, dt \tag{2-35}$$

In the homogeneously broadened case, free-induction decay is expected to be observed after the arrival of the second pulse. The peak occurs at $t = t_d + t_p$ (where t_d and t_p are the delay and width of the pulse) and then decays with $\tau_{decay} = T_2 / 2$. The time-integrated FWM signal decays as a function of time delay as $\exp(-2\tau_d / T_2)$. Therefore, this exponential decay can be used to determine the dephasing time T_2.

In an inhomogeneously broadened system, the phases of the different frequency components excited within the spectral bandwidth of the laser evolve at different rates. Therefore, the macroscopic polarization created by the first pulses decays to zero within the laser pulse width τ_p if the inhomogeneous linewidth $\Gamma_{in\,\mathrm{hom}}$ is larger than the laser spectral width. If the second pulse arrives at a time shorter than the dephasing time T_2, rephasing will occur and result in a photon echo at time τ_d after the second pulse. The FWHM of the echo is determined by τ_p and $\Gamma_{in\,\mathrm{hom}}$, and the intensity is proportional to $\exp(-4\tau_d / T_2)$.

In a semiconductor system, excitons or the interactions between electrons and holes can play an important role and therefore the case becomes more complicated. In the low excitation regime, one can neglect the weak Coulomb interaction and use the Bloch equations for independent two-level systems, as described in section 2-2-2. However, for strong excitation conditions, local field effects [22], excitation induced dephasing [23] and biexcitons [24] can have important contributions.

Chapter 3

Semiconductor Quantum Structures

3-1 General theory of semiconductors

Generally, solids with conductivities between 10^{4} and 10^{-10} ($\Omega.cm^{-1}$) are classified as semiconductors. Germanium (Ge) and silicon (Si) are typical elemental semiconductors, and III-V and II-VI compounds, such as gallium arsenide (GaAs) and zinc oxide (ZnO), are typical compound semiconductors.

Semiconductors are specified by certain properties, for example, the electrical conductivity increases exponentially with temperature for a pure semiconductor. For an impure semiconductor the conductivity depends strongly on the impurity concentration. In a heavily doped material, however, the conductivity changes only slightly with temperature, just as in a metal. Furthermore, the conductivity can be changed by irradiation with light or high energy electrons or by the injected carriers. In such a semiconductor charge transport may be either by electrons or holes, depending on the type of doping.

The periodicity of a semiconductor lattice introduces the concepts of the reciprocal lattice and the Brillouin zone, and allows one to specify the energy levels in a semiconductor in terms of the energy versus momentum picture. Intrinsic semiconductors are characterized by a band gap separating the occupied valence band and the empty conduction band at low temperatures. All semiconductors can be classified either as direct gap semiconductors with a valence band maximum and a conduction band minimum occurring at the same point in the Brillouin zone, or as indirect gap semiconductors in which these extrema occur at different points in the Brillouin zone. The optical properties of direct gap semiconductors differ considerably from those of indirect gap semiconductors [1, 2].

The statistics of the occupation of energy levels by carriers in a semiconductor are described by Fermi-Dirac statistics. Specifically, the probability of an electron occupying a state at energy E is described by

$$f_n(E) = \frac{1}{\exp[(E - E_F)/k_B T] - 1} \tag{3-1}$$

where E_F is the Fermi energy, k_B is the Boltzmann constant, and T is the temperature. Correspondingly, the hole distribution function is

$$f_p(E) = 1 - f_n(E) = \frac{1}{\exp[(E_F - E)/k_B T] - 1} \tag{3-2}$$

The density of states (DOS) in semiconductors is an important concept, which expresses the number of states per unit volume and per unit energy. For parabolic bands, the DOS for the conduction and valence band can be written respectively as:

$$g_n(E) = 4\pi(2m_e^*/h^2)^{3/2}(E - E_c)^{1/2} \tag{3-3}$$

$$g_p(E) = 4\pi(2m_h^*/h^2)^{3/2}(E_v - E)^{1/2} \tag{3-4}$$

where m_e^* and m_h^* are the effective masses of an electron and hole, and E_c and E_v are the energies at the bottom of the conduction band and the top of the valence band, respectively. The total number of electrons in the conduction band and holes in the valence band can be expressed as:

$$n = \int_{E_c}^{\infty} g_n(E)\, f_n(E)\, dE \tag{3-5}$$

$$p = \int_{-\infty}^{E_v} g_p(E)\, f_p(E)\, dE \tag{3-6}$$

3-2 Quantum confinement in semiconductors

One of the important features of semiconductor nanostructures is the flexibility of controlling and designing the properties of such materials [1-3], including controlling the size [4, 5], constructing artificial structures [6, 7] and using various doping [8] or some of the post-growth techniques, such as intermixing [9]. Such nanostructures exhibit structural, electronic and optical properties that are unique and different from both macroscopic materials and isolated molecules. In nanostructures, normally 1 to 50 nanometers in scale, the dimensions are commensurate with the de Broglie wavelength of the charge carriers; so that quantum confinement effects become important and the properties of the semiconductors are significantly modified.

Advanced semiconductor growth techniques, such as molecular beam epitaxy (MBE) and metalorganic chemical vapour deposition (MOCVD), allow fabrication of various semiconductor nanostructures or low dimensional structures. Such low dimensional structures include (i) quantum wells (QWs), where the charge carriers are confined along the growth direction z but free to move in the other two directions x and y, (ii) quantum wires, where the charge carriers are confined in two directions and only allow one dimension motion, and (iii) quantum dots (QDs), where the charge carriers are confined in all three directions. Strong interband transitions are possible in these low dimensional structures because there is a probability of a strong overlap between the wave functions of the electrons and holes. Figure 3-1 compares the density of states as a function of energy in different dimensional materials, bulk, quantum well, quantum wire and quantum dot.

For a bulk material, the density of states in the conduction band and the valence band is described by (3-3) and (3-4). For a two-dimensional QW or one-dimensional quantum wire system, the quantum confinement effects result in discrete subbands in both the conduction and the valence bands and an increase of bandgap energy, as shown in figure 3-1. The density of states in the subbands can be written as $g_e(E) \propto E^0$ for a two-dimensional quantum well and $g_e(E) \propto E^{-1/2}$ for a one-dimensional quantum wire.

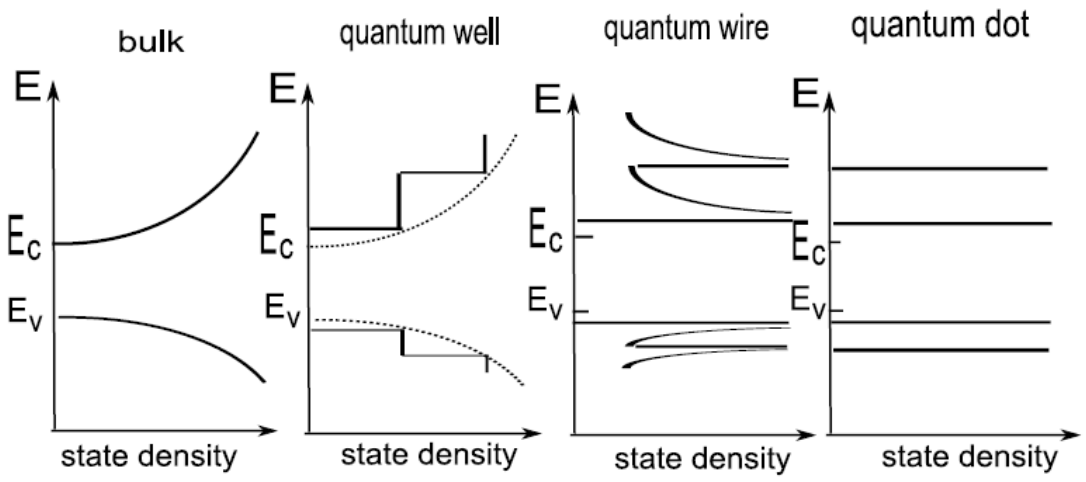

Figure 3-1 Density of states as a function of energy in bulk, quantum wells, quantum wires and quantum dots. E_c and E_v indicate the bottom of the conduction band and the top of the valence band, respectively.

In a *quantum well* system, due to the one dimensional confinement of electrons, the electron energy levels can be found from the solution of the Schrödinger equation for an infinitely deep potential well, with the form:

$$E_n = \frac{\hbar^2 \pi^2}{2m_e^* L^2} n^2 \qquad n = 1, 2, 3, \cdots \tag{3-7}$$

where m_e^* is the effective mass of the electron, and the dependence of the energy levels on $(1/L)^2$ is the quantum size effect. The dispersion relation for the conduction band can be written as (for confinement in the z direction)

$$E(k) = E_c + E_{nz} + \frac{\hbar^2 (k_x^2 + k_y^2)}{2m_e^*} \tag{3-8}$$

where E_{nz} is given by (3-7). For the conduction band, the density of states per unit area in a two-dimensional QW system in the subbands can be expressed as (for energies greater than $E_c + E_{nz}$)

$$g(E) = \frac{m_e^*}{\pi \hbar^2} \tag{3-9}$$

Thus, for each quantum number n_Z the density of states is constant and the overall density of states is the sum of these for all values of n_z, which results in a staircase-type distribution with a step height given by equation (3-9).

In a one-dimensional *quantum wire* system, the carriers are confined in two directions (z and x), and the dispersion relation for the conduction band can be written as

$$E(k) = E_c + E_{nz} + E_{nx} + \frac{\hbar^2 k_y^2}{2m_e^*} \tag{3-10}$$

In each of the subbands, the density of states can be described as a function of energy by $g_e(E) \propto E^{-1/2}$.

In a zero-dimensional *quantum dot* system, the carriers are confined in three directions and the dispersion relation for the conduction band can be expressed as

$$E(k) = E_c + E_{nz} + E_{nx} + E_{ny} \tag{3-11}$$

In this case the density of states is described by a set of discrete $\delta-$functions as shown in figure 3-1. Thus, QDs are generally referred to as artificial atoms due to the similar discrete energy level structures. It is noteworthy that the density of states in the valence band has a similar distribution to that of in the conduction band.

3-3 Semiconductor nanostructures

Due to the quantum confinement effect, the energy bandgap of semiconductor nanostructures increases with decreasing the size of the quantum structures. Nowadays, using MBE and MOCVD growth techniques, it is possible to construct various artificial structures,

such as single quantum wells, multiple quantum wells and superlattices etc., in which the period of the layers may be as small as a few monolayers.

A quantum dot is a fragment of matter that is smaller than the electronic Bohr radius in all three coordinates, with a size normally ranging from a few hundreds to many hundreds of atoms. In quantum dots, the electronic transitions are discrete, and most importantly, they are tunable as a function of dot size. An important issue in such systems is the effect of the surface on their properties. They are very sensitive to the surface properties due to the high surface to volume ratio. Surface states typically play a dominant role in these systems, acting as efficient traps for electrons and holes, and thus surface passivation is essential for fabricating practical semiconductor devices based on such low-dimensional structures[10-12].

As with bulk semiconductor devices, doping is an effective technique for modifying the electronic and optical properties of semiconductor quantum structures. With this technique, certain impurities known as dopants are introduced. The dopants are chosen so that they have either an extra electron in their outer shell compared to the host semiconductor or one fewer electron. The resulting dopant is called a donor or an acceptor. The donor atom is treated as a shallow defect and the electron-donor interaction is represented by a Coulomb potential. A group III element can form an acceptor in Si or Ge while Si can be an acceptor if it replaces As in GaAs.

In semiconductor nanostructures, doping processes can be more complicated than in bulk semiconductors. For example, dopants may be introduced in either the barrier layer (modulation doping) or in the quantum dots (direct doping), which leads to a complicated energy band structure in the interface region. The carrier capture and sebsequent relaxation are very relevant to the details of the structures in the active region.

In addition to doping, implantation induced intermixing, known as an impurity-free technique, is another effective method for modifying the electronic and optical properties. With this technique, some defects are created in the quantum well or quantum dot region by various techniques, such as ion implantation or laser irradiation. After a subsequent fast annealing, in general most of the ions are removed from the material and atom interdiffusion takes place, which may significantly modify the electronic and optical properties of the semiconductor. Some remaining ions may act in a similar manner to defects and also affect the electronic and optical properties. Ion implantation and laser induced intermixing are the general methods used for quantum well intermixing [9, 13, 14].

3-4 Optical transitions in semiconductor nanostructures

The dynamics of electrons, holes, excitons and phonons in semiconductor nanostructures are influenced by their interaction with each other, as well as with defects and interfaces of the system. There are extensive discussions of these interactions in the literature [2, 12, 15, 16]. Here we present a summary of the important interactions relevant to this thesis.

In optical spectroscopy, optical excitation, energy relaxation and optical emission in a quantum well are the most important topics for the various transitions illustrated in figure 3-2. Due to the quantum confinement effect, the electron and hole energy bands of the QWs or superlattices are split into electron subbands e1, e2 (conduction band) and hole subbands h1, h2 (valence band), as shown in figure 3-2. The arrows indicate possible optical transitions. (1) and (5) are direct interband transitions, which correspond to optical excitations to either the quantum well subband or the continuum band of the barrier, and recombination of electron-hole pairs or excitons. In an interband absorption process, a photon absorption is followed by electron-hole pair generation. In the opposite process, a photon emission is followed by

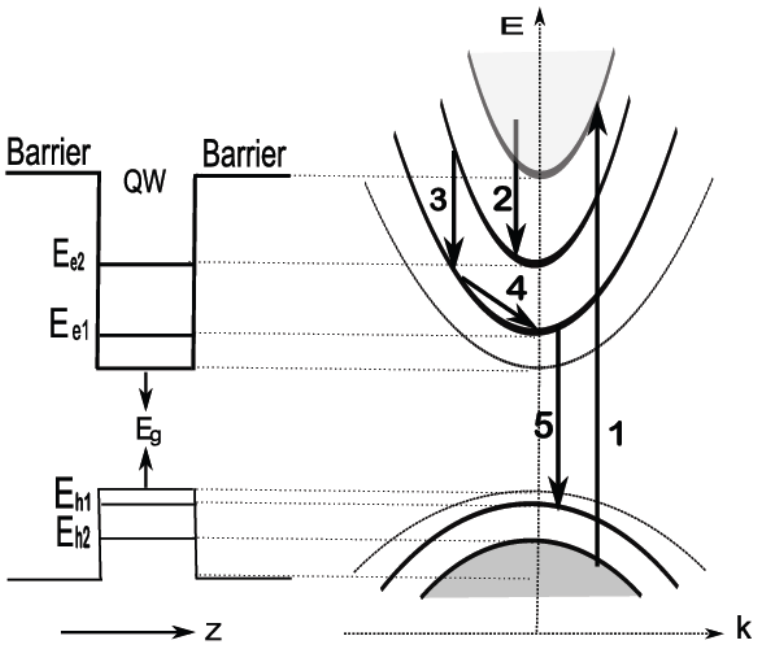

Figure 3-2 Band diagram and optical transitions in a single QW

electron-hole pair or exciton recombination. This type of transition is usually in the ultraviolet to near infrared region. (2) is a transition from the continuum states of the barrier to the quantum-confined states of the quantum well (carrier capture). Electron-electron scattering, electron-hole scattering or phonon scattering can result in this transition. (3) is a direct intersubband transition, such as intersubband relaxation or absorption, and usually corresponds to a relatively small energy transition. This type of transition is also important in physics because of extensive applications in the mid-infrared or far-infrared regions (2-20 μm), such as infrared detection, infrared modulation, quantum cascade lasers, etc. (4) is an indirect intrasubband transition. Phonon scattering is usually in this category.

In principle, transitions in quantum wires are similar to those in QWs due to a similar energy state structure. The energy band structure of a QD, however, is quite different. Due to the three-dimensional quantum confinement, the energy states become discrete levels, which results in unique energy relaxation rules. Thus, intrasubband transitions are not available in QDs. Due to the discrete energy states, some unique effects appear in QD systems, such as the phonon bottleneck. The energy separations in a QD generally cannot match the energy of phonons; so that the system does not satisfy energy conservation, which results in the suppression of phonon emission between two sublevels of a QD [17, 18]. These unique effects and the energy relaxation mechanisms are some of the most important topics in QD research and applications.

3-4-1 Carrier-phonon scattering

The interaction between carriers and phonons plays a major role in the exchange of energy and momentum between the carriers and the lattice, and hence determines the relaxation of photoexcited semiconductors as well as the transport properties of semiconductors. Several texts present extensive discussions on these processes and the scattering rates derived using Fermi's golden rule are presented in these references [19-22].

Electrons can relax into lower subbands via Coulomb scattering and phonon scattering following laser excitation. GaAs-like semiconductors are intermediate between covalent semiconductors like Si and Ge and ionic semiconductors like CdS. Scattering between the carriers and optical phonons is the dominant scattering mechanism (Fröhlich interaction) in carrier-phonon scattering processes in GaAs-like semiconductors. Holes also interact with longitudinal optical (LO) phonons via Fröhlich interaction. Holes might be

expected to interact more efficiently with LO phonons than electrons because the Fröhlich interaction rate varies with the effective mass ($m_{eff}^{1/2}$). However, the complicated band structure of the holes leads to an effective reduction of the phonon scattering rate by a factor of two [22].

The case of spacing of subbands far above the LO phonon energy leads to population of states in the lower subband with extra in-plane momentum. The relaxation rate depends on the subband spacing. In quantum wells, the relaxation is usually fast due to the continuum subband. Because of the k^{-2} -dependence of the electron-LO phonon scattering rate, a subband spacing resonant with the LO phonon energy results in a much faster relaxation rate than a subband spacing far above the LO phonon energy. For a quantum dot system, the situation can be much different due to its discrete energy states. If the energy spacing cannot satisfy the condition of energy conservation, the relaxation rate through LO phonons should be much slower.

The interaction with acoustic phonons can also be important. If the carrier has sufficient energy to emit an optical phonon, then the optical phonon scattering rate is generally considerably higher than the acoustic phonon scattering rate. Phonon emission processes are independent of the phonon occupation number and hence temperature. Phonon absorption, on the other hand, is proportional to the phonon occupation number and hence is strongly temperature dependent [1]. In semiconductor systems, multi-phonon processes can also play an important role in the relaxation.

3-4-2 Carrier-carrier scattering

Carrier-carrier scattering determines the energy exchange between carriers and is primarily responsible for the thermalization of photoexcited non-thermal carriers. This process is mediated by Coulomb interaction and includes electron-electron, hole-hole and electron-hole scattering. The difference in the effective masses between electrons and holes reduces the energy exchange between these two species. The long-range Coulomb interaction diverges in the absence of screening. Spin relaxation processes can also play an important role in the dynamics of photoexcited systems.

In semiconductor nanostructures, the scattering rates are modified by several factors, such as different band structures, phonon modes and density of states, which result in some

new effects in the case of QWs or QDs. For example, the effective carrier-LO phonon scattering is prohibited due to the discrete energy states in QDs [23].

Chapter 4

ZnO/ZnMgO multiple quantum wells

4-1 Introduction

ZnO has a large fundamental band gap of ~3.37 eV at room temperature, and high thermal conductivity, high luminous efficiency and mechanical and chemical robustness. Thus ZnO and its alloys have great prospects in optoelectronics applications ranging from ultraviolet to red wavelengths [1-7]. ZnO also has the advantage of a large exciton binding energy [8, 9], about 60 meV, which assures more efficient excitonic emission at higher temperatures [10]. Moreover, excitons in ZnO-based quantum well heterostructures exhibit high stability compared to bulk semiconductors or III–V QWs due to enhancement of the binding energy and reduction of the exciton–phonon coupling [11-13] caused by quantum confinement. Due to these effects, excitons are expected to play an important role in many-body processes such as laser action and nonlinear absorption of ZnO QWs even at room temperature. In principle the threshold for lasing using biexcitons is expected to be ever lower than that using an exciton-exciton scattering process [14]. There is a great potential in the possibility of using biexcitons as a laser action mechanism for UV wavelengths and room temperature operation because of their large binding energy in ZnO (12-16 meV) and ZnO quantum wells (more than 30 meV) [2]. There are only a few papers on the coherent optical properties of excitons and biexcitons in ZnO [15-17]. A detailed study of excitons and biexcitons in ZnO multiple quantum wells (MQWs) is thus important for understanding the optical properties of these wide band gap heterostructures, especially in view of their potential application to ultraviolet–blue optoelectronic devices [18].

Band gap engineering is an important research field for further ZnO applications. Alloying ZnO with CdO [19-22] and MgO [23-29] have allowed the generation of red- or blue-shifts of the emission wavelength, respectively. In the alloy system $Zn_xMg_{1-x}O$, the emission wavelength can be precisely tuned by changing the Mg composition [23, 30] or by inducing thermal intermixing in the ZnMgO superlattice by annealing [31, 32]. These techniques result in a uniform wavelength shift throughout the whole material, which could be

a disadvantage when trying to achieve monolithic integration of devices with different functionality on the same chip. In order to overcome this problem, several techniques currently can achieve the goal of precisely tuning the emission wavelength in both the vertical and lateral directions. These include selective area epitaxy and layer intermixing [33-36]. Ion implantation induced intermixing has two main advantages. One is the number of defects introduced by ion irradiation can be precisely controlled, thus allowing precise control of the amount of wavelength shifting, and the other is no further processing or regrowth is required.

Although there have been many decades of extensive investigation on ZnO materials, so far a reliable and reproducible high-quality p-type conducting ZnO has not been achieved [3, 37] and some of the basic properties still remain unclear or under debate, for example, the effect of the intrinsic defects and impurities on the radiative and nonradiative transitions. Moreover, the coherence properties of ZnO are still almost unexplored [38], especially in various nanostructures of ZnO.

In this study, low energy (80 keV) oxygen implantation into a ZnO/ZnMgO superlattice was used to place the peak of the damage in the quantum well region. Various spectroscopy techniques, such as photoluminescence, time-resolved photoluminescence, pump-probe and four-wave mixing, are performed to characterize the optical properties of ZnO multiple quantum wells and the effect of oxygen implantation.

4-2 Experiments

4-2-1 Sample growth and oxygen implantation

The ZnO/$Zn_{0.7}Mg_{0.3}O$ multiple quantum well samples used in this study were grown in the New Materials Research Centre, Osaka Institute of Technology, oxygen implanted at the Australian National University and provided by Ms V A Coleman. The sample is a single crystal stack of 19 ZnO/$Zn_{0.7}Mg_{0.3}O$ multiple quantum wells grown on *a*-plane sapphire by molecular beam epitaxy [26, 39]. The structure of the samples is shown in figure 4-1, which consists of a 10 nm thick ZnO buffer grown at low temperature (250 ℃), followed by a 500 nm thick ZnO layer grown at 500 ℃. The 19 ZnO/$Zn_{0.7}Mg_{0.3}O$ MQWs were grown on top of these buffers. The ZnO wells have a thickness of 2 nm, (another two groups of MQW samples with a well width of 3 nm and 4 nm were also used in some experiments) and the

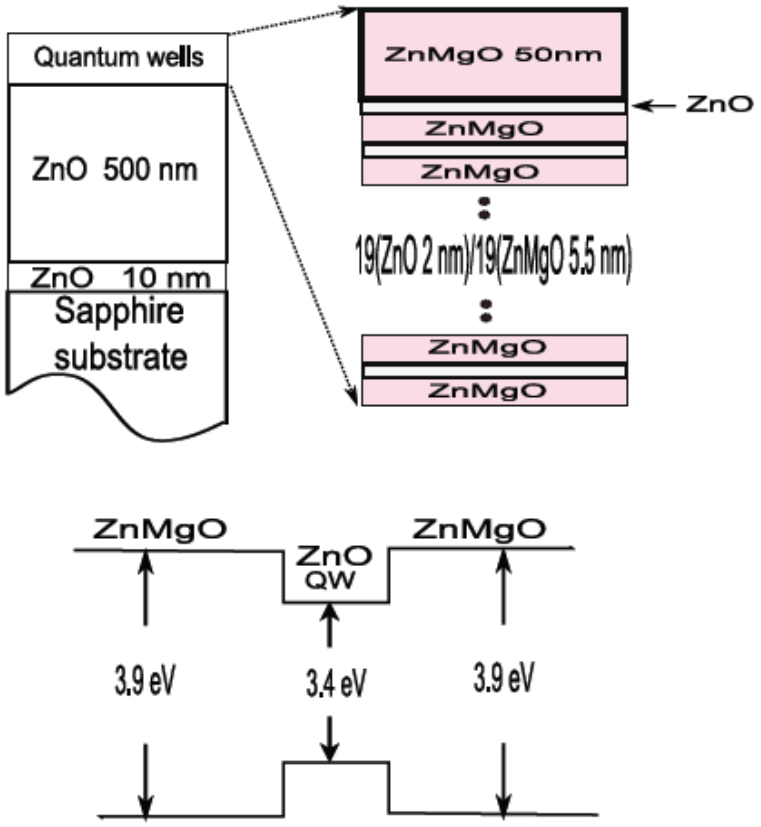

Figure 4-1 ZnO/ZnMgO multiple quantum well structure (above) and band alignment of type I (below)

$Zn_{0.7}Mg_{0.3}O$ barrier layers are 5.5 nm thick. The multiple quantum wells are capped by a 50 nm layer of $Zn_{0.7}Mg_{0.3}O$. The ZnO/ZnMgO sample has a band alignment of type I (figure 4-1) and the barrier band-gap energy is about 3.9 eV corresponding to the absorption wavelength 320 nm or shorter.

Prior to all experiments, the sample was cut and chemically cleaned. Some pieces of the sample were kept for an annealing study. The rest were implanted with 80 keV oxygen ions in the dose range of $5\times10^{14} - 1\times10^{16}\ ions/cm^2$ at room temperature, using a 1.7 MeV tandem accelerator (NEC, 5SDH-4). Oxygen ions were chosen to avoid complications arising from introducing an impurity ion into the system. The ion beam flux was $\sim 3\times10^{12}\ cm^{-2}s^{-1}$. During implantation, the samples were tilted 7^0 relative to the incident beam to minimize channeling. A piece of Si was used to mask a part of the sample during implantation to be used as a reference. Figure 4-2 shows the calculated displacement density expected during the implantation as a function of depth based on TRIM code calculations [26]. Also shown in this figure is the location of the MQWs of 2 nm and 4 nm thickness with respect to the

displacement profile. It is clear that only a small part of the MQWs is in the low implantation dose region for the 2 nm thickness sample and a significantly larger part of the MQWs is in the low implantation dose region for the sample of 4 nm thickness. Rapid thermal annealing (RTA) of the samples (both implanted and unimplanted) was conducted at 800℃ in an Ar ambient for 60 s. One piece of the sample was left as-grown for a reference.

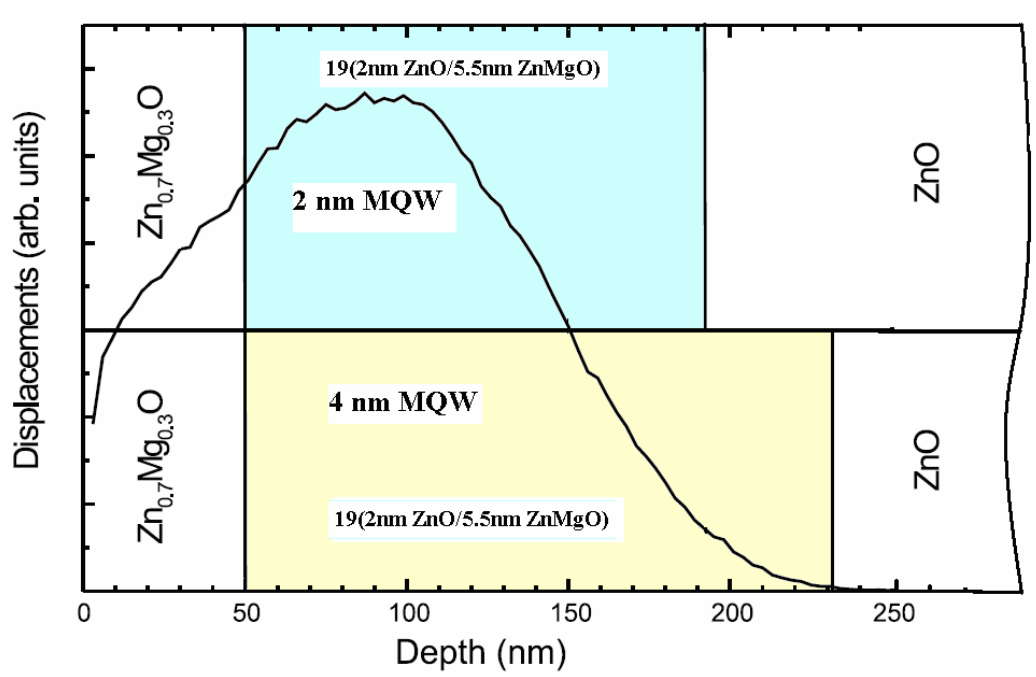

Figure 4-2 Displacement profile in the oxygen implantation for various thicknesses of MQWs

4-2-2 Spectroscopy

The excitation laser pulses used in the photoluminescence (PL) experiment are the third harmonic of the fundamental pulses from the Ti:sapphire regenerative amplifier, with wavelength 266 nm, pulse duration 100 fs and 1 kHz repetition rate. The detector is a UV-visible response photomultiplier tube at the output slit of a 0.25 m monochromator. Pump-probe experiments and FWM experiments were performed in the same setup, which is similar to that of the photon echoes described in Chapter 2. In the experiments, two ultrashort pulses with duration 100 fs from two independent OPAs (wave vectors $\mathbf{k}_1$ and $\mathbf{k}_2$) were used for the

pump and probe with a tunable wavelength and suitable time delay. The detection system includes two independent spectrometers with CCDs for detection of the diffracted beams $\mathbf{k}_3 = 2\mathbf{k}_1 - \mathbf{k}_2$ or $\mathbf{k}_4 = 2\mathbf{k}_2 - \mathbf{k}_1$ in the FWM experiment and only the probe ($\mathbf{k}_2$) for the pump-probe experiment.

4-3 Experimental results and discussion

4-3-1 Implantation effect in temperature quenching of photoluminescence

In the photoluminescence experiment, strong quantum well emission is observed at low temperatures and the wavelength depends on the thickness of the quantum well. At 20 K, the emission peaks of as-grown MQW samples with 2, 3 and 4 nm thickness are located at 360, 370 and 389 nm, respectively. It is evident that the wavelength shift relative to the photoluminescence of bulk ZnO is due to the quantum confinement effect. Similar phenomena have also been observed in other QWs and nanostructures of ZnO [40-43].

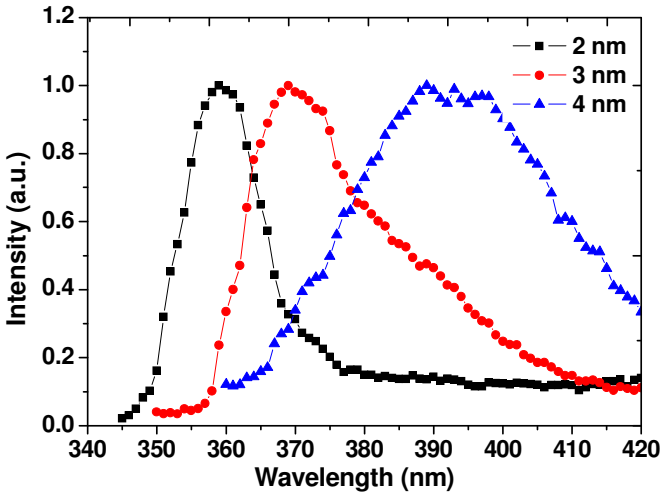

Figure 4-3 Photoluminescence of ZnO/ZnMgO multiple quantum well samples with a well width of 2 nm (a), 3 nm (b) and 4nm (c)

A number of groups have studied the PL of ZnO quantum wells or nanostructures, and the details of the origin of the spectra in the near band gap region have been identified [25, 44-47]. The near band gap PL consists of peaks of free and bound exciton emissions, followed by their longitudinal optical phonon replica on the low energy side as a shoulder [48, 49]. The 2 nm sample (Figure 4-3(a)) has a relatively narrow PL band with a full width at half maximum of 20 nm and a weak shoulder on the low energy side. Compared with the 2 nm sample, the 3 nm sample has a broader band near the PL peak and a relatively strong phonon replica band. The 4 nm sample shows a quite broad PL emission band, which is most likely the combination of different emission transitions because the intensity of the quantum well emission in this sample is comparable with that of ZnO bulk and this sample has a small blue-shift and enhanced quantum confinement Stark effect due to relatively thick quantum wells and thus weak quantum confinement [50, 51]. This band is superposed on the band edge emission of ZnO bulk, which is supported by the PL observation of the implanted samples, as discussed in section 4-3-2. In this experiment, the PL band from the ZnMgO barrier cannot be observed, which suggests the carrier capture from the barrier is effective in the quantum well and the excitation laser is not sufficiently strong to lead to saturation in quantum wells.

Figure 4-4 shows the PL of the MQW samples of as-grown (reference) and implanted samples for various ion doses with 2 nm ZnO/ZnMgO quantum wells. The rapid thermal annealed sample has a very similar PL spectrum (not shown here) to the reference sample and

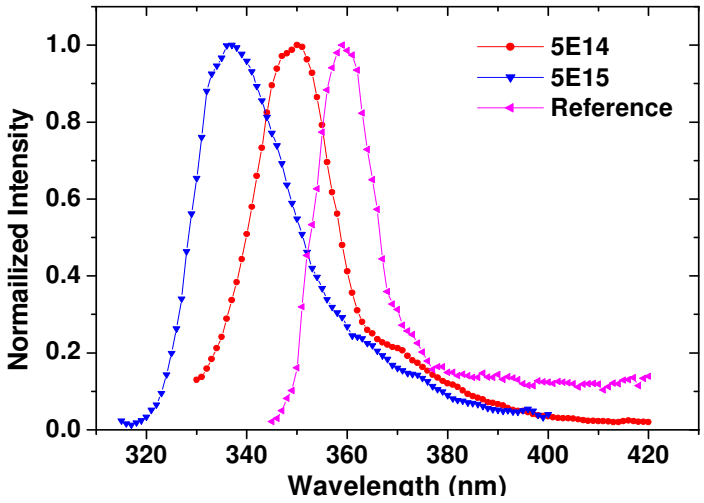

Figure 4-4 Photoluminescence of ZnO/ZnMgO MQW samples: reference and implanted samples. The ion implantation doses are in units of ions/cm^2

no blue shift can be observed, which indicates that the RTA does not lead to intermixing. On the other hand, the implanted samples have an increased blue shift with increasing oxygen ion dose, from a peak of 360 nm for the as-grown sample to 350 nm for the low ion dose sample and 340 nm for the high ion dose sample, which is mainly consistent with the cathodoluminescence (CL) observation by Coleman et al. [26]. At the same time, the ZnO peak becomes broader with increasing ion dose, especially for the high dose samples, and the spectra show an enhanced shoulder on the low-energy side. The broadening, as well as the shoulder feature, is most likely a result of an inhomogeneous distribution of defects induced by implantation across the MQW region, leading to variations in the extent of intermixing across the interface region between the quantum well and the barrier. It is worth noting that at the high dose implantation, 1×10^{16} ions/cm^2, the PL broadens and the PL intensity decreases significantly, which indicates that irradiation at high dose leads to lattice damage and amorphism in ZnO, similar to other observations of ion irradiation [52, 53]. Similar effects are also observed in the 3 nm and 4 nm QW samples.

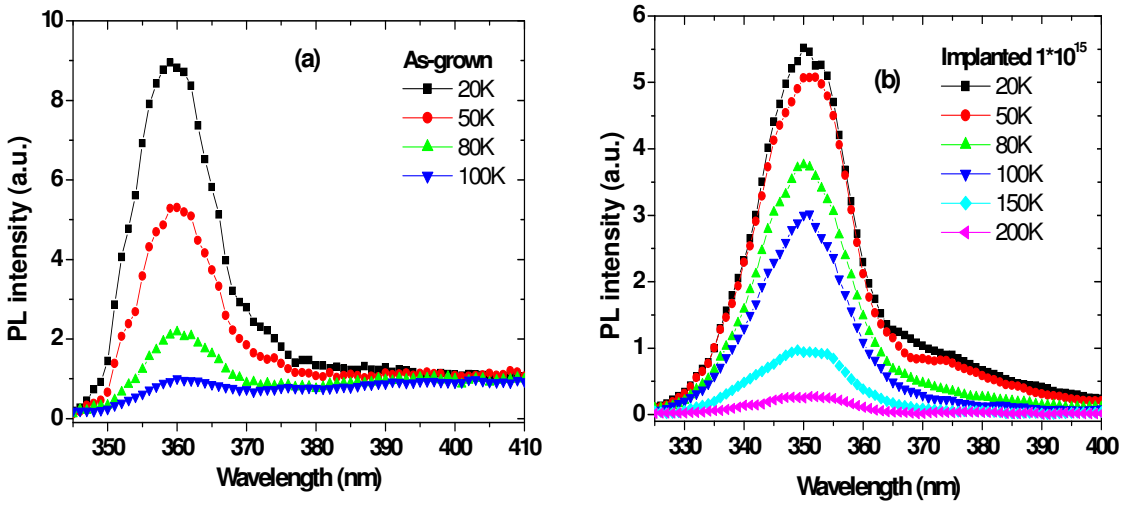

Figure 4-5 Temperature dependence of photoluminescence from as-grown and implanted samples

It is interesting that ion implantation results in a remarkable change in the rate of quenching of the PL with increasing temperature, e.g., the temperature quenching rate of the implanted samples with low ion dose ($5\times10^{14}, 1\times10^{15}\ ions/cm^2$) is significantly slower than that of the reference, while the temperature quenching rate of the high ion dose implanted samples is similar to the reference. Figure 4-5 shows the temperature dependence of the PL of the 2 nm samples, as-grown (a) and an implanted sample with an ion dose of

$5\times10^{15}\ ions/cm^2$ (b). The PL intensity decreases quite rapidly with increasing temperature in the as-grown sample and the peak intensity decreases to only 10% as the temperature is increased from 20 K to 100 K. With further increasing temperature, the emission of the quantum wells continues to decrease. At about 200 K it is washed out by the emission of the band edge emission of the ZnO bulk, as shown in figure 4-6. The implanted sample, on the other hand, shows a significantly slower temperature quenching rate, the PL intensity remains at more than 50% as the temperature is increased from 20 K to 100 K, and the PL can be observed even at room temperature. It is worth noting that the temperature quenching rate of the high ion dose implanted sample ($1\times10^{16}\ ions/cm^2$) has a markedly slower quenching rate, similar to that of the reference sample.

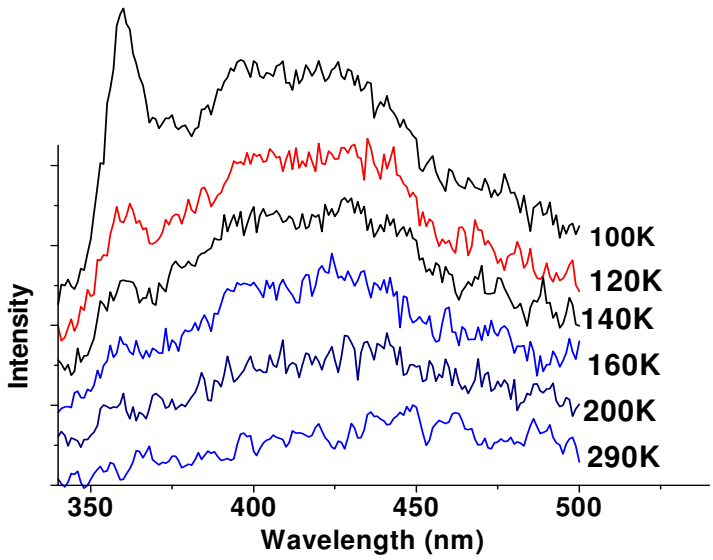

Figure 4-6 Photoluminescence as a function of temperature, showing how with increasing temperature, the emission of the quantum wells decreases and is washed out by the band edge emission of ZnO bulk at 200 K. Each PL spectrum is offset

At the same time, the peak intensity at low temperatures is changed by the ion implantation. At 20 K, the peak intensity of the implanted samples with low dose (5×10^{14},$1\times10^{15}\ ions/cm^2$) increases by about 20% compared with the reference sample, while the intensity of the high dose implanted samples decreases significantly relative to the reference.

In order to compare the temperature quenching rate between the reference and the implanted samples, an activation energy is introduced to describe the temperature quenching process [54]. With optical injection of excitons, the population governing a certain transition is given by

$$\frac{\delta n}{\delta t} = G - \frac{n}{\tau_R} - \frac{n}{\tau_{NR}} \tag{4-1}$$

where n is the density of the photoexcited excitons, G is the generation rate, and τ_R and τ_{NR} are radiative and nonradiative lifetimes, respectively. Generally, the exciton PL decay consists of two components, i.e., radiative and nonradiative recombinations, with $\tau_{PL}^{-1} = \tau_R^{-1} + \tau_{NR}^{-1}$. The nonradiative recombination rates are thermally activated, whether they correspond to level depopulation or to the activation of a nonradiative recombination centre, i.e., $\tau_{NR} = \tau_0 \exp(E_a / k_B T)$ with E_a the activation energy and k_B Boltzmann's constant [46, 54]. The quantum efficiency can be expressed as $\eta_{PL} = \left(1 + \tau_R / \tau_{NR}\right)^{-1}$. Thus

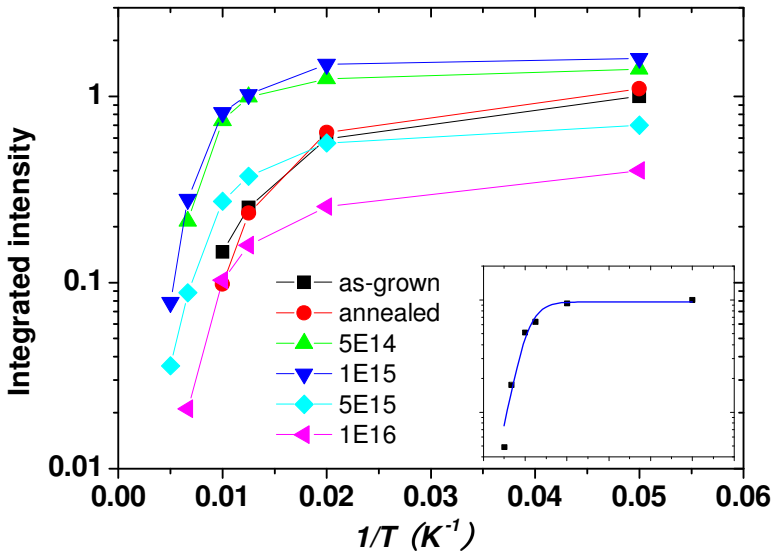

Figure 4-7 Temperature dependence of integrated intensity of the excitonic band of ZnO/ZnMgO MQWs. The inset is a fit with equation (4-2) for one of the implanted samples

the nonradiative lifetime τ_{NR} decreases with increasing temperature, which results in a decrease in quantum efficiency and a decrease in the PL intensity.

The PL intensity is proportional to n/τ_R and, in the steady state, we obtain the familiar expression

$$I = I_0 /[1+\alpha \exp(-E_a / k_B T)] \qquad (4\text{-}2)$$

with $\alpha = \tau_R / \tau_0$.

Figure 4-7 is an Arrhenius plot of the integrated intensity of excitonic bands in the ZnO/ZnMgO quantum well samples. The inset is a fit with equation (4-2) for one of the implanted samples (5×10^{15} $ions/cm^2$), which shows it is well described by a single activation energy. We can deduce the activation energy from fitting the temperature dependence data with equation (4-2), as shown in figure 4-8 (circles). The peak intensity variation at 20 K in the 2 nm sample is also shown in this figure (triangles), which shows that the peak intensity is enhanced by suitable dose implantation. However, high dose ion irradiation results in a decrease in the intensity due to lattice damage and agglomeration of defects. Compared with the reference, the activation energy of the implanted samples with low dose is significantly larger by 30-35 meV, and with further increasing the dose the activation energy decreases to about 20-30 meV, which is still slightly larger than that of the reference sample. Under very high dose, 1×10^{16} $ions/cm^2$, the activation energy decreases further due to lattice damage and agglomeration of defects leading to large defect clusters, which leads to the formation of structural defects acting as nonradiative centres.

To date many investigations have been performed on the nature of various defects in ZnO and their correlation with the radiative emission bands and nonradiative recombination using various techniques, such as PL, time-resolved PL, positron annihilation spectroscopy, etc [2, 3, 55-59]. In ZnO, point defects are known to be nonradiative centres. However, the nature of the details of the defects is still not clear and is under debate [3].

According to Kohan and Van de Walle's calculations [60, 61], the most important factor determining the concentration of a defect in a crystal is its formation energy E^f which is determined by:

$$C = N_{sites} \exp(-E^f / k_B T) \qquad (4\text{-}3)$$

where N_{sites} is the concentration of sites in the crystal where the defect can occur. For ZnO, an oxygen vacancy and zinc vacancy have the lowest formation energy; so they are the most common point defects, which have been confirmed by experiments [62-64]. It has been shown that dynamic annealing of point defects generated by ion implantation in ZnO is extremely efficient. In the case of oxygen implantation, a myriad of defects can be produced, such as Zn vacancies and interstitials, O vacancies and interstitials and antisites. Recently, in an oxygen implantation experiment, Vijayakumar et al. reported that the main point defect introduced by oxygen implantation is the zinc vacancy and that a high dose ($2\times10^{16}\ cm^{-2}$) of irradiation leads to extensive lattice damage in ZnO sample [52]. At the same time, a marked decrease in electron mobility is found due to ion implantation.

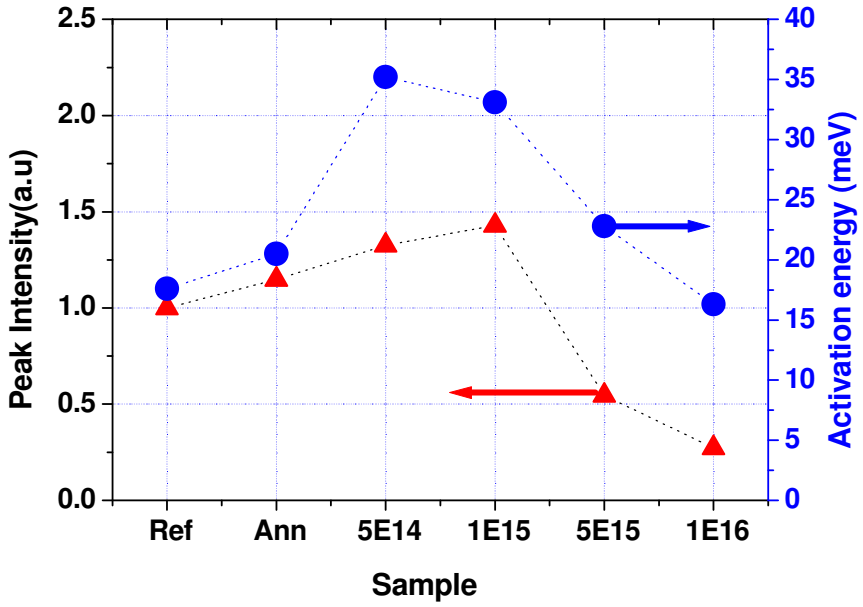

Figure 4-8 Activation energy (circles) and peak intensity (triangles) in 2 nm thick MQW samples. Ref and Ann refer to reference and annealed, respectively

Very recently, Chichibu and colleagues proposed that certain point defect complexes associated with a zinc vacancy, V_{Zn} ($V_{Zn} - X$), are the dominant nonradiative centres and result in a reduction of the band edge emission [56]. According to Chichibu and Kohan, a single point defect in ZnO, including V_{ZnO}, is not likely to act as a nonradiative centre.

In our experiment, increasing the linear intensity and slowing the temperature quenching rate suggest that nonradiative recombination decreases in implanted samples. The most likely situation is that, although the concentration of V_{ZnO} is not decreased or even slightly increased by ion implantation, the carrier mobility is markedly decreased, which suppresses the formation of the point defect complexes associated with V_{ZnO} that act as nonradiative centres. Thus the concentration of the point defect complexes and the activation energy is increased and nonradiative recombination is decreased. With further increase of the ion dose, the lattice damage and agglomeration of defects is significantly increased. These defect clusters could again act as nonradiative recombination centres and result in an increase of nonradiative recombination and reduction of PL intensity. However, further work is needed to better understand the mechanism of ion implantation induced defect complexes in ZnO quantum wells.

It is noteworthy that ion implantation not only can be used for suitable band gap engineering for precisely tuning the energy shift in a selective area, due to strong dynamic annealing at the high temperature, but it can also be used to suppress nonradiative recombination in order to improve the quantum efficiency and the room temperature properties.

4-3-2 Implantation effect in thick MQW

According to TRIM code calculations [26], the intermixing effect induced by implantation takes place mainly in the front 80-100 nm of the quantum well surface region. For thick quantum well samples, such as the 4 nm sample, the total thickness of the quantum well is equal to 19*(4+5.5)=180.5 nm, which means that nearly half of the sample will experience low dose implantation. Because the amount of blue shift depends on the irradiation dose, a low implantation dose would result in a small blue shift, which leads to a separated PL peak of the exciton transition in the PL spectra. After implantation, the quantum well emission shifts to the blue while emission of the ZnO bulk still has the same wavelength due to no implantation, which leads to the original emission band separated into the quantum well emission band and the ZnO bulk band edge emission.

Figure 4-9 shows the PL spectra from the 4 nm thick reference sample (triangles) and the implanted MWQ sample with $5\times10^{14}\ ions/cm^2$ at 20 K (circles). The PL from the reference sample is a broad band which may consist of an overlap of several components,

such as free and bound exciton transitions in the quantum wells, phonon replica in the quantum wells, and band edge transitions in the ZnO bulk because the relatively thick well results in a stronger quantum confined Stark effect and weaker quantum confinement effect. This weak quantum confinement effect also results in a relatively weak MQW exciton emission, comparable in intensity with the band edge emission of bulk ZnO. For thin MQW samples, such as the 2 nm sample, the PL band of the exciton transitions is much stronger than band edge emission of bulk ZnO.

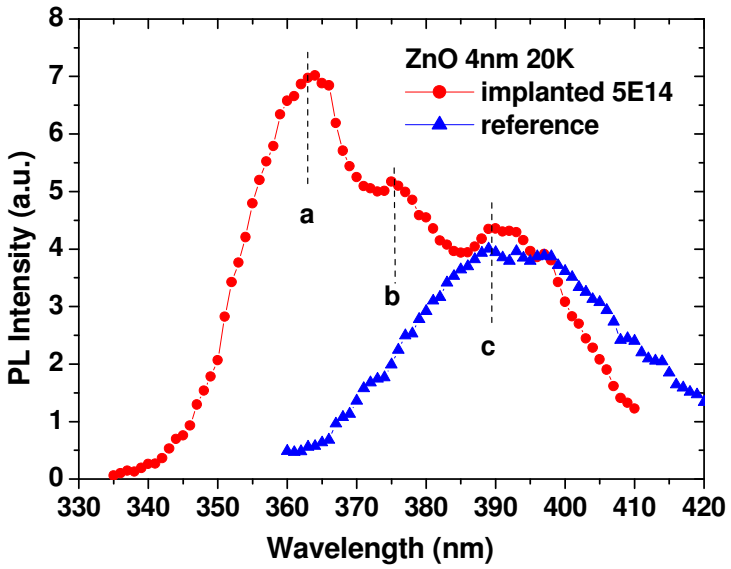

Figure 4-9 PL Comparison of PL spectra for the thick reference and implanted MQW samples

After oxygen implantation, clearly separated exciton PL peaks from quantum wells are observed due to the blue shift induced by the oxygen implantation. The PL band (a), which originates mainly from the exciton transitions, is significantly narrower than that of the reference, which supports the interpretation that the broad band of the reference sample originates from the overlap of quantum well emission and band edge emission of the bulk ZnO. The peak (b) should originate from two components: one is exciton emission from the back part of the quantum wells that was implanted with low dose, and thus exhibits a smaller blue shift, and the other is a phonon replica contribution of the front part of the quantum wells. Peak (c) should be mainly due to the back quantum wells that were almost not implanted. However, the blue shift changes continuously with the ion dose; so it is impossible to separate all of the components.

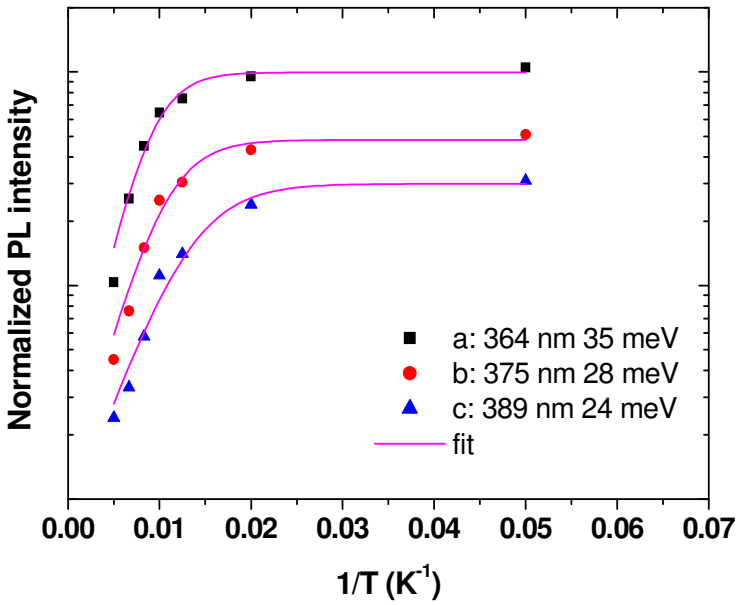

Figure 4-10 Temperature dependence of the intensity of peaks a, b, c

We compare the temperature dependence of the peaks a, b and c, as shown in figure 4-10, and deduce activation energies by fitting equation (4-2). Peak (a), which corresponds to the implanted exciton transition band of the MQW, gives the largest activation energy of 35 meV. Peak (b), which originates mostly from a lower implantation dose and phonon replica, gives an activation energy of 28 meV. Peak (c), which originates mainly from the unimplanted MQW and phonon replica, gives the lowest activation energy of 24 meV.

4-3-3 Observation of biexcitons in four-wave mixing

ZnO materials have a large binding energy and further enhancement of the binding energy in ZnO-based quantum wells due to quantum confinement makes it possible to achieve low threshold stimulated emission or laser action at temperatures up to room temperature [29, 65, 66]. Two excitons with opposite spins may interact to form a bound state known as a biexciton (also known as an exciton molecule) at high excitation. Biexcitonic transitions can play an important role because of their linear and nonlinear optical properties, such as a low threshold density for stimulated emission or lasing and a high gain coefficient [9, 17, 67]. The

threshold for biexciton recombination or formation is significantly lower than that for exciton-exciton recombination, i.e., the biexciton gain should be advantageous from the viewpoint of applications as a low-threshold semiconductor [2].

The binding energy of the biexciton has been measured to be in the range 12-16 meV in bulk ZnO [9, 68], and it is enhanced in ZnO/ZnMgO quantum wells due to the quantum confinement effect, leading to the observation of binding energies larger than 30 meV [9, 12, 67, 69]. This is comparable to the thermal energy at 300 K, which suggests the possibility of biexciton lasing at room temperature with only minimal cooling required. To date, however, there has been no experimental observation of biexcitonic emission from ZnO/ZnMgO quantum wells at room temperature.

The simplest way to experimentally observe biexcitons and determine the binding energy is to study the luminescence spectrum, where the biexciton peak appears at lower energy than the exciton [67] and with an amplitude that varies quadratically with excitation intensity. However, with this method it is difficult to resolve the biexciton peak at room temperature due to inhomogeneous broadening and thermal broadening of the transitions. Time integrated and spectrally resolved FWM techniques have also been used to observe emission from biexcitons in a background-free phase-matching direction [16, 70]. However, the broadening again makes it difficult to resolve the biexciton peak, whilst the short dephasing time at room temperature makes it difficult to distinguish the biexciton signal from other many-body effects, such as local field effects and excitation induced dephasing, at short negative delays.

In this study we use one-colour and two-colour spectrally resolved FWM experiments to observe biexciton transitions in ZnO/ZnMgO multiple quantum wells at room temperature. The experiment setup is a typical two-pulse degenerate FWM, as described in chapter 2. Two laser pulses (denoted as pulse-1 and pulse-2) from two independent OPAs and with wave vectors $\mathbf{k_1}$ and $\mathbf{k_2}$ are incident on a thin sample. Pulse-2 is delayed with respect to pulse-1 by τ_d , and the signal due to the third-order polarisation in the $2\mathbf{k_2}-\mathbf{k_1}$ direction is detected. In this configuration, pulse-1 arrives first and establishes a polarization in the sample, and then pulse-2 interferes with the polarization to generate a population grating if the pulse separation τ_d is shorter than the dephasing time. Pulse-2 can then be diffracted from this grating in the $2\mathbf{k}_2-\mathbf{k}_1$ direction. Thus, a signal is observed only when pulse-1 arrives before pulse-2, hereafter referred to as a positive delay. In the time integrated FWM experiment, the

intensity of the signal is proportional to $\exp(-2\tau_d/T_2)$ in a homogeneously broadened system or $\exp(-4\tau_d/T_2)$ in an inhomogeneously broadened system, where T_2 is the dephasing time [71].

At the same time, a signal can be generated at negative delays as a result of many-body effects, such as local-field effects and excitation-induced dephasing [71], and it is also possible to generate a signal at negative delays from biexcitons [72], in which case the two

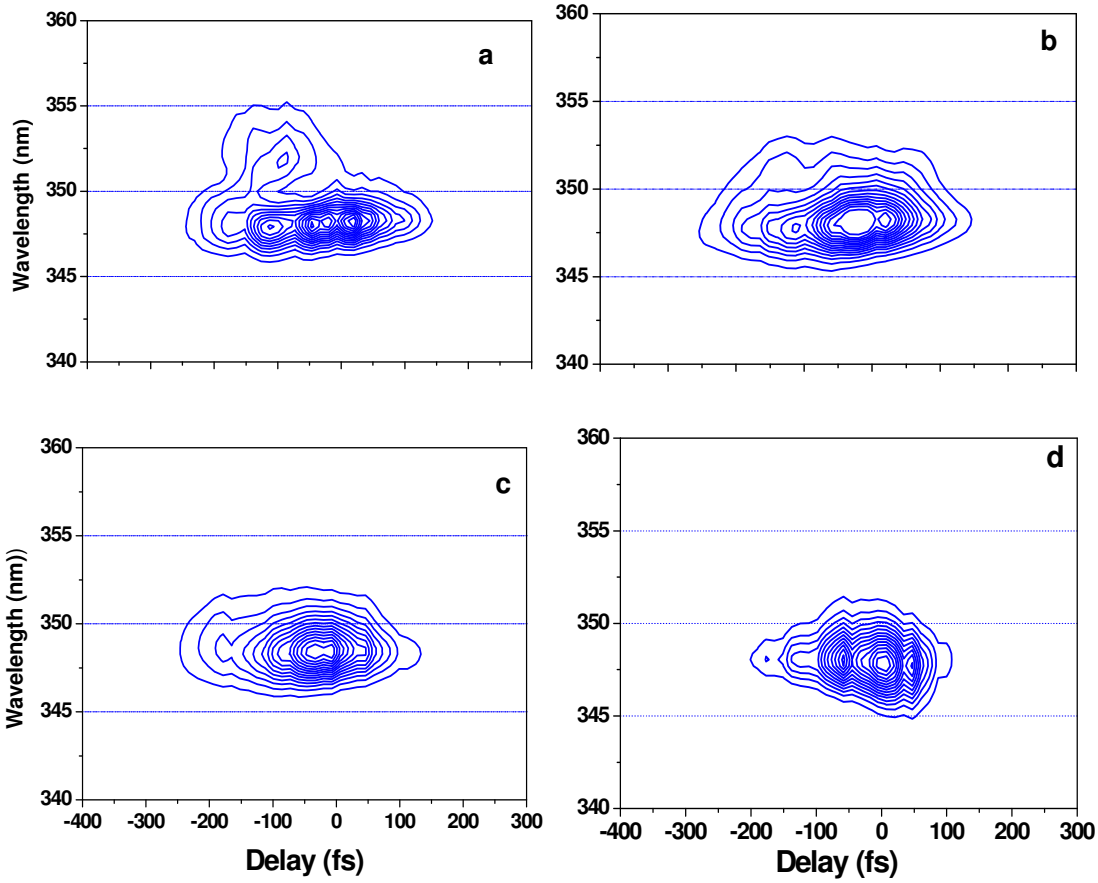

Figure 4-11 Spectrally resolved FWM signal for different excitation intensities as a function of time delay between pulses, a: $8\,I_0$, b: $5\,I_0$, c: $3\,I_0$, d: $I_0 = 0.1 mJ/cm^2$

photons from pulse-2 establish a two-photon coherence (i.e., a biexciton), from which a photon of pulse-1 can diffract and give a signal in the $2\mathbf{k_2}\text{-}\mathbf{k_1}$ direction that decays at a rate determined by the dephasing time of the biexciton. Indeed, this signal from a biexciton would be expected to exist almost entirely at negative delays [73]. It is a problem to determine the

origin of negative time-delay signals because local-field effects, excitation induced dephasing and biexcitons are qualitatively similar although the local-field effect is independent of the excitation intensity while both excitation-induced dephasing and biexcitons depend on the excitation intensity [71].

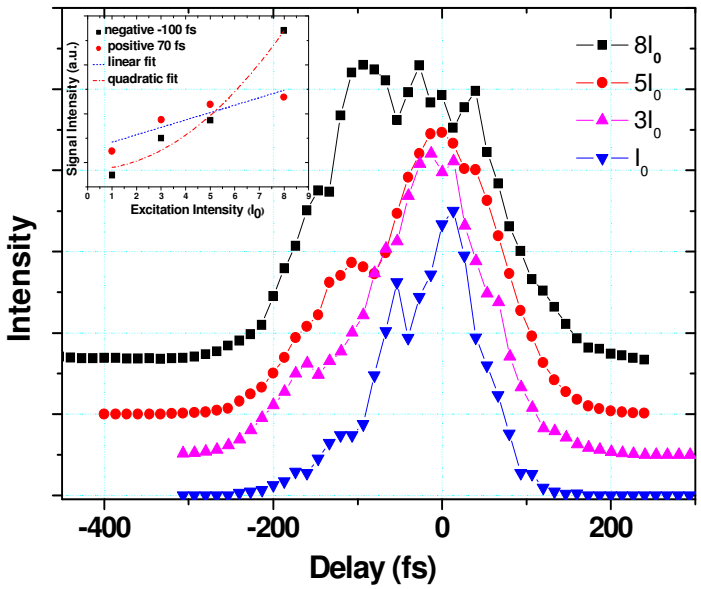

Figure 4-12 Wavelength-integrated FWM signal at different excitation intensities. Each plot is offset and the real zero intensity corresponds to the intensity at long time delay -300 fs. The inset shows the signal intensity variation with increasing excitation intensity in positive delay (70 fs, circles) and negative delay (-100 fs, squares).

In the case of a two-colour experiment, the 'normal' signal would be expected to exist only when there is coherent transfer of the polarisation from the state pumped by pulse-1 to the state probed by pulse-2. Local-field effects and excitation induced dephasing are both, in principle, based on the interaction between excitons and their transfer of coherence, but in the two colour case, the excitons excited by pulse-1 and pulse-2 have different wavelengths; so that the transfer of coherence is expected to be weak. A signal from a two-photon coherence, however, can still exist when the two pulses are of a different colour, since pulse-1 simply needs to diffract from the coherent biexciton. It is by the observation of this signal, using a two-colour spectrally resolved FWM setup, that the presence of biexcitons at room temperature is identified.

In the one-colour experiment, 350 nm laser pulses with 100 fs duration were used and the sample is the low implanted ($5\times10^{14} ions/cm^2$) 2 nm thick ZnO/ZnMgO. Figure 4-11 shows the spectrally resolved transient FWM signal as function of time delay τ_d for different excitation intensities, where (a) to (d) correspond to excitation intensities of $8I_0$, $5I_0$, $3I_0$ and I_0 with $I_0 \sim 0.1 mJ/cm^2$ per pulse. The corresponding time evolution of the wavelength-integrated FWM signals is shown in figure 4-12. On the positive delay side, with increasing time delay, the spectral width decreases, which indicates that there is some signal from the sample after the excitation pulses have ceased temporally overlapping. We can see from the time evolution of the integrated signal that the decay of the signal for positive delay is independent of the excitation intensity, from which we can deduce an exciton dephasing time $150\pm10\ fs$ using a single exponential function fit based on inhomogeneous broadening. However, for negative delay, with increasing excitation intensity, clear spectral broadening can be observed (also figure 4-11). This is due to many body effects, which become important at high excitation intensities, and can include the presence of biexcitons. Furthermore, the decay is very rapid for low excitation intensity but increases with the excitation intensity. This indicates there is a significant signal for negative delays beyond the temporal overlap of the

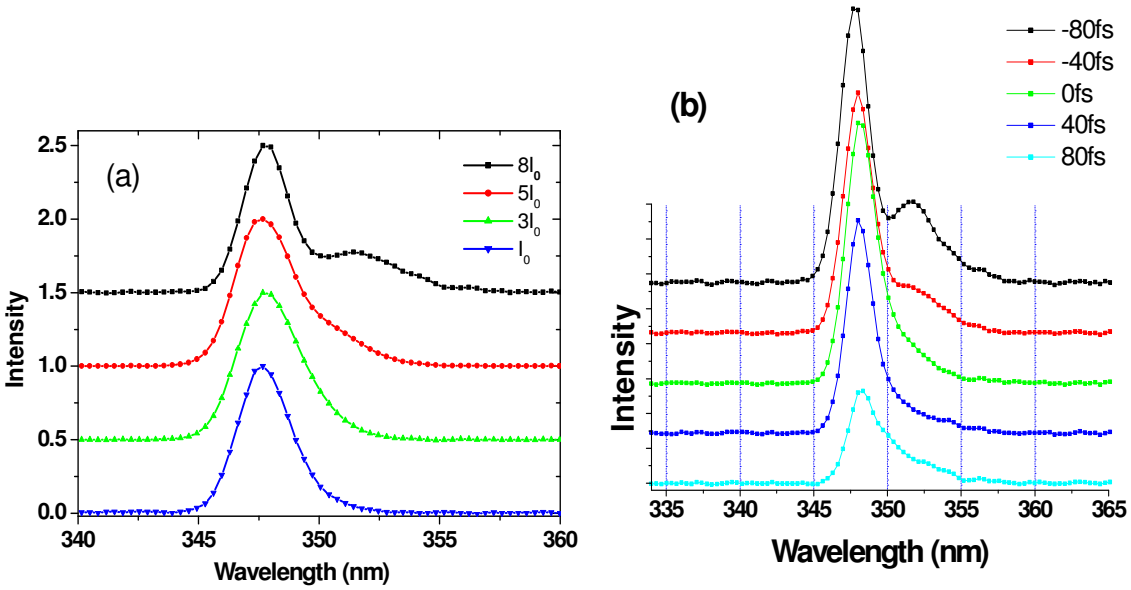

Figure 4-13 Spectra of time-integrated FWM signals with one-colour excitation for a negative delay of 40 fs and different excitation intensities (a) and different time delays at high intensity (b)

two pulses which is only present at high excitation intensity. The signal variation for different excitation intensities is compared in the inset of figure 4-12 for positive delay (70 fs, circles) and negative delay (-100 fs, squares). It is clear that the signal of the negative delay increases significantly faster with increasing excitation intensity than that of the positive delay and that the negative and positive signals can be approximately fitted with quadratic and linear functions, respectively. This signal may originate from excitation induced dephasing and the presence of biexcitons.

Figure 4-13 (a) compares the spectra of time-integrated FWM signals for negative delay and different excitation intensities. There is a significant increase on the long wavelength side with increasing excitation intensity which forms a clear dual-peak structure at high excitation intensity. Figure 4-13(b) compares the spectra for different time delays. Similarly, there is a significant component on the long wavelength side for the negative delays.

The origin of the negative delay signal is clarified in the two colour experiments, in which pulse 1 and pulse 2 have a wavelength of 350 nm and 360 nm, respectively, and the FWM signal is detected in the $2\mathbf{k}_2 - \mathbf{k}_1$ direction. The wavelength of the FWM signal in this direction is given by $2\omega_2 - \omega_1$, which in this case generates a signal at 370 nm as shown in figure 4-14. For the normal FWM signal in this configuration, there needs to be coherent transfer of polarization between the states excited by the 360 nm and 350 nm pulses. This is also true for the signal at negative delay due to local field effects and excitation induced dephasing, in which the decay of such a signal for negative delay would be twice as fast as

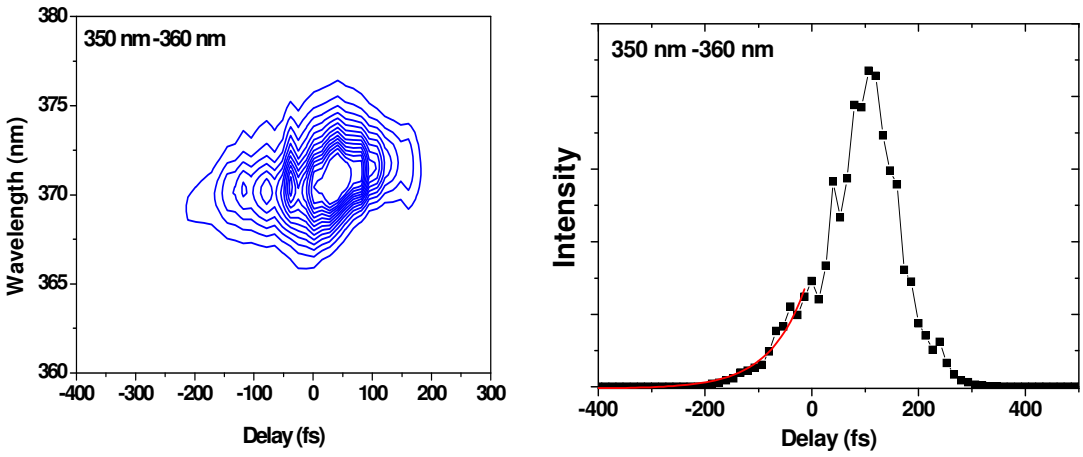

Figure 4-14 FWM signal for two-colour excitation at 350 and 360 nm

that for positive delay [71]. The experimental result shows that there is a rapid decay for positive delay, but an extended signal at negative delay, well beyond the time when the two pulses temporally overlap. This is clear evidence that the extended signal originates from the generation of a two-photon coherence, most likely in the form of a biexciton. The intensity dependence experiment shows, similarly to that of the one-colour experiment for negative delay, that the second peak is enhanced at high excitation intensity and absent at low intensity, which is consistent with the behaviour expected for biexcitons. From the decay of the signal, the decoherence time of the two-photon coherence is deduced to be 90 ± 10 *fs* using a single exponential fit. A similar two-colour experiment was performed with 340 nm and 350 nm excitation and gives a similar decoherence time. Given that these experiments were performed at room temperature and phonons are expected to be the dominant cause of dephasing, this is a remarkable observation. Other sources of a two-photon coherence, such as an unbound exciton pair, would be expected to dephase even more rapidly, and within the laser pulse, due to enhanced interaction with the environment.

4-3-4 Pump-probe experiment

Time-resolved photoluminescence plays an important role for understanding the detailed physical processes in hot exciton scattering and exciton recombination. Pump-probe provides the simplest technique for obtaining time resolution limited by the laser pulse-width. In this experiment the pump pulse is adjusted to 340 nm and the probe pulse, which has much low intensity (~1%), is tuned from 350 nm to 380 nm. Both pulses have a duration of 100 fs and the transmitted intensity is detected. The samples used in this study include the samples of 2 nm thickness multiple quantum wells with implantation dose of 5×10^{15} ions/cm^2 and without implantation.

Figure 4-15 shows the time evolution of the transmission at probe wavelengths 350 nm and 370 nm. Near time zero a very sharp peak appears, which is attributed to a coherence spike on the time scale of tens of femtoseconds. A relatively slow decay follows, which corresponds to exciton relaxation or recombination. The transmission decays with a single exponential function, which gives the decay time of the detected state. We compare the decay time at different probe wavelengths as shown in figure 4-16. On the high energy side the decay times are very short, of the order of hundreds of femtoseconds, whilst on the low

energy side the decay times are relatively long, of the order of tens of picoseconds. In the optical excitation process, the pump pulse generates hot excitons with a small amount of excess energy because the wavelength of the pump is 340 nm. The hot excitons lose their excess energy in a few hundreds of femtoseconds to low states mainly by exciton-LO phonon interactions, resulting in a quasi-equilibrium distribution of thermalized excitons [74]. This process can be fast because of efficient exciton energy cooling through LO scattering in the two-dimension quantum wells at room temperature. The subsequent processes consist of localization at potential fluctuations, scattering with electrons or other excitons and eventually recombination radiatively or nonradiatively on a time scale of a few hundred picoseconds.

At 350 nm and 360 nm, the dominant process is carrier relaxation through LO-phonon scattering because this is much faster than the recombination process [74]. In the pump-probe experiment, the reference sample gives decay times of 710 fs and 830 fs at 350 nm and

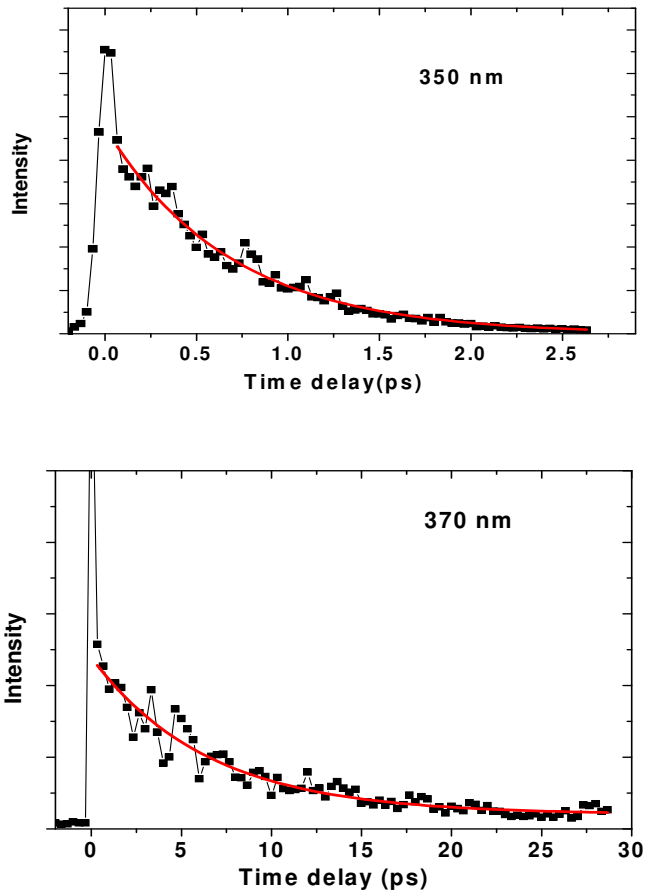

Figure 4- 15 Time evolution of transmission at probe wavelength of 350 nm and 370 nm, which shows a single exponential decay

360 nm, and almost the same decay times for the implanted sample, with 730 fs and 920 fs, respectively. Due to inhomogeneous broadening and thermal broadening, low quantum efficiency at room temperature and low resolution of the spectrometer, it is difficult to identify exactly the detailed nature of the transitions at various wavelengths. We can estimate that the main transitions include the recombination of hot carriers on the high energy side (350-360 nm), free excitons, localized excitons and exciton replica roughly in the range from 370 to 400 nm [49]. At room temperature, nonradiative recombination rather than radiative recombination should be the dominant process because of the very low PL efficiency. Thus on the low energy side the decay time could correspond mainly to the nonradiative recombination lifetime with about 40 ps.

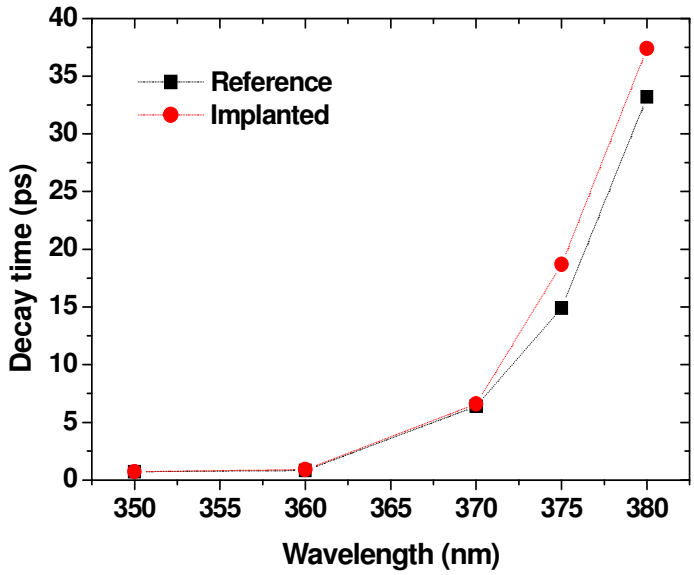

Figure 4-16 Comparison of the decay time between the reference (squares) and implanted (circles) ZnO/ZnMgO MQW as a function of probe wavelength for a pump wavelength 340 nm

In general, nonradiative decay in semiconductors is correlated with certain kinds of point defects. However, no clear correlation is found between the PL decay time and the point defect density, and the nonradiative process is considered to be governed by certain defect species introduced by the presence of Zn vacancies such as vacancy complexes. As mentioned earlier, compared with the as-grown sample, the implanted sample exhibits a slightly longer lifetime at all wavelengths, which is consistent with the high quantum efficiency and slower temperature quenching rate in the PL temperature dependence experiment. This observation

also supports the conclusion that a suitable dose of oxygen implantation can improve the quality of the MQW.

4-4 Conclusions

We have studied the ZnO/ZnMgO MQW and oxygen-implanted MQW samples using various ultrafast spectroscopy techniques. In the PL experiment, a clear blue shift is observed for the implanted samples, and the blue shift increases with increasing oxygen implantation dose. In the implanted sample, significant temperature quenching improvement takes place at low implantation dose, which could be due to the oxygen implantation suppressing the formation of nonradiative centres that are most likely defect complexes with Zn vacancies. A high dose of implantation leads to lattice damage and agglomeration of defects leading to large defect clusters, so that additional nonradiative centres will be introduced, which leads to a low quantum efficiency and a fast temperature quenching rate of the PL.

Biexcitons may play an important role in low threshold laser action due to the binding energy enhancement in the ZnO/ZnMgO MQW. However it is normally very difficult to identify this effect especially at room temperature, because of strong inhomogeneous broadening and thermal broadening, and also the very short dephasing time. In the one- and two-colour two-beam spectrally resolved degenerate FWM experiment, the biexciton effect is observed at room temperature and the decoherence time of the two-photon coherence is deduced to be $90 \pm 10\ fs$. The experiment also gives an exciton dephasing time of $150 \pm 10\ fs$ based on the inhomogeneous broadening.

In the pump probe experiment, we observe the decay time in the band edge region. In the high energy region, 350 nm and 360 nm, the dominant process is hot exciton relaxation with LO phonon scattering, giving a decay time in the subpicosecond range. In the low energy region, 370 nm and 380 nm, the dominant process is exciton recombination. At room temperature the recombination process is mainly governed by nonradiative recombination with a time scale of about 40 picoseconds.

Chapter 5

InGaAs Quantum Structures

5-1 Electron dynamics in InGaAs quantum dots

Semiconductor quantum dots have been the subject of intensive research in recent years due to their great potential both in applications and in fundamental studies [1-3]. Especially, with the progress of growth technology it is possible to precisely control the quantum structures in the growth and achieve a variety of quantum structures. On the applications side quantum dots could be the best candidate for the next generation of photonics devices, such as high performance lasers and photo-detectors. Semiconductor quantum dots have unique discrete states due to the three dimensional confinement. In principle, quantum dot lasers can achieve high efficiency because nearly all of the energy is concentrated in the ground state and they can have excellent temperature stability due to the discrete energy levels. QD detectors can cover a very broad range of wavelengths because of the various discrete energy states in the QDs based on their interband and intersubband transitions. In fundamental studies, quantum dots can be regarded as artificial atoms because they have discrete energy states like atoms or molecules; so it is possible to make quantum dots with various structures to study various quantum effects or discover new phenomena.

One of the simplest and most common ways of producing semiconductor QDs is the Stranski and Krastanov self-assembled growth of strained QDs (SAQDs) [4, 5]. In this growth mode, elastic energy associated with the lattice mismatch strain between different epitaxially deposited semiconductor layers is minimized through the formation of a small island connected by a thin wetting layer (WL). This high crystalline quality island is typically of pyramidal shape with 10-30 nm base dimension and 2-8 nm height. By capping these self-assembled islands with an epitaxial layer of a wider band-gap material and a lattice constant similar to that of the substrate, high quality QDs can be produced. One of the main disadvantages of this growth mode is the size distribution of the SAQDs, which is typically about ±10%. This, together with a possible distribution in composition, strain field and

structure shape, gives rise to a large non-uniformity of the SAQD properties in general and inhomogeneous broadening of their optical spectral features in particular.

SAQDs are typically grown from a quasi-two-dimensional wetting layer. Consequently, the relevant electronic structure consists of two parts, the discrete QD states due to three dimensional confinement and a quasi-continuum WL band due to one dimensional confinement. The localized QD states are energetically below the delocalized WL states. In a usual optical experiment, a pump process initially generates carriers in the WL. The carrier dynamics in the QDs critically depends on the capture of carriers from the WL into the QD states as well as the relaxation of carriers between the discrete QD states. An important question is the extent to which these processes limit the laser operation in comparison to the extensively studied quantum-well laser.

InGaAs (InAs) is one of the most important semiconductor quantum dot materials which provide a tunable wavelength to cover the near infrared range for the optical communication industry. Many applications have been found for InGaAs (InAs) quantum dots, including infrared detectors [6, 7], single electron transistors [8, 9], QD memory devices [10] and QD lasers [3, 11]. Quantum dots have been proposed as a possible route to increase the modulation speed of semiconductor lasers because they have the potential to achieve very high differential gain due to their unique discrete energy levels. In principle, a QD active region can couple every injected electron and hole to the lasing mode. By contrast a quantum well has a small probability for its electrons and holes to occupy only those states that couple to the lasing mode due to their continuous density of states. This is an essential requirement for high efficiency, high modulation speed and stable temperature QD lasers that achieve efficient relaxation to the ground state. However, the energy relaxation was found to be limited by the so-called phonon bottleneck effect which is also due to the discrete energy states of the QDs [12, 13]. Carrier capture and sequent relaxation is a most important subject and has been the subject of extensive research [14-22] for the last decade because it is closely relevant to both applications and fundamental research. The slow relaxation rate had been considered as evidence of a phonon bottleneck in many observations [23-26]. On the other hand, other studies indicated that relaxation within the quantum dots proceeds at a rate greatly exceeding that originally thought possible in the presence of a phonon bottleneck. Several explanations have been proposed for this fast relaxation, including Auger processes [27-29], electron-hole scattering [18, 30-32] and multiphonon emission [19, 33-35]. The wide range of energy relaxation times is likely to be a result of a number of factors, such as lattice temperature, excitation intensity, excitation energy and various SAQD features resulting from

different growth conditions, such as different dot sizes, shapes, ground state energies and electron and hole potential depths.

During the process of non-resonant optical excitation of a semiconductor system, electrons and holes are normally created in the higher-energy continuum states. Photoexcited electrons and holes relax into the ground state (assuming negligible recombination in the excited state because the lifetime in general is much longer than the relaxation time) in cascade via phonon emissions and finally recombine to emit light. In higher dimensional systems (bulk or quantum well) the dominant relaxation process is longitudinal optical (LO) phonon emission via Fröhlich interaction [13, 36] with subpicosecond relaxation times because it is easy to satisfy energy and momentum conservation in the continuum. However, in a quantum dot, this process is forbidden because it is difficult to satisfy energy conservation in a discrete state system. The deformation potential interaction with longitudinal acoustic (LA) phonons, which is already weaker in the bulk, becomes even weaker as the dot size is reduced due to a decreasing form factor [36]. The relaxation via LA phonon emission in quantum dots is slower than in the bulk by many orders of magnitude [13, 20]. An efficient phonon relaxation can only be achieved when the energy separation between the discrete states of the QDs is equal to the LO phonon energy or is within the narrow window $LO \pm LA$ [36]. Thus, very slow intersubband relaxation rates are generally observed in a QD system, which is called a phonon bottleneck [23, 26, 37].

However, contradictory effects have been found in many experimental observations [33, 38]. Many different mechanisms have been proposed to break the phonon bottleneck and result in fast intersubband relaxation [19, 22, 29, 39-41]. For instance, in a QD laser device, the pump generates a high density electron-hole plasma in the delocalized states. Under these conditions electron-electron and hole-hole scattering (Auger process) can provide efficient transitions for electrons and holes from the delocalized WL states into the discrete localized QD states (carrier capture) as well as between the discrete QD states (carrier relaxation) [29, 42]. A detailed inspection of the kinetic equation for Coulomb scattering shows that these are only some of the possible processes, for example, a relaxation process starting with two carriers in an excited QD state where one is scattered into the QD ground state and the other into the WL [39].

On the other hand, interaction between carriers and LO-phonons can also lead to efficient scattering channels if energy conservation can be satisfied. The energy separation of the QD states typically does not match the LO-phonon energy whilst capture processes of carriers from the WL to the QD states are often possible for holes since they have shallower

confinement energy than electrons. Thus electron-hole scattering becomes a possible relaxation channel, in which electrons transfer their extra energy to holes and relax into the ground state of the QDs, while the holes jump into the WL [43]. Holes can effectively relax back because of their small energy separation through phonon or multiphonon relaxation. Furthermore, multiphonon scattering and defect-assisted relaxation were also regarded as possible relaxation mechanisms for the QDs in which a significantly faster relaxation than predicted by phonon bottleneck can be achieved [19, 20, 34, 44].

P-doped self-assembled QDs can greatly improve the performance of QD lasers, in terms of stable temperature characteristics and promising high-speed properties [3, 45, 46]. The first characteric is attributed to countering the effect of thermal smearing of holes in closely spaced hole levels. The high-speed characteristics are known to be strongly affected by carrier capture and sequent relaxation. In doped QDs, the presence of built-in carriers can alter the carrier dynamics and result in an enhancement of the relaxation rate.

As shown in figure 5-1, the essential difference between undoped and doped QDs is the carrier density in the conduction and valence bands. For undoped QDs, after laser pulse excitation, equal densities of electrons and holes are generated in the conduction and valence bands. Therefore, the sample ensemble is neutral in charge. P-doped (n-doped) QDs have an excess of holes (electrons) built-in the valence (conduction) band before laser excitation. In p-doped QDs the photoexcited electron density in the conduction band is smaller than the

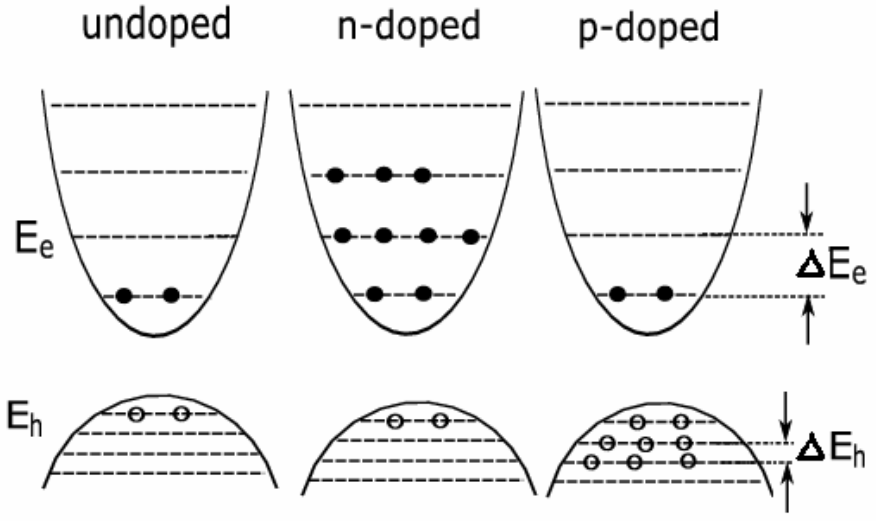

Figure 5-1 Primary difference between undoped, n-doped and p-doped QDs

density of holes in the valence band, and so electrons can recombine with the holes in the ground state due to the small energy spacing in the valence band [47]. Therefore, in p-doped QDs, the carrier dynamics essentially depend on electron capture from the wetting layer and sequent intersubband relaxation because excess holes reside in the valence band prior to laser excitation.

Another important subject is how the doping processes and dopants affect the electrical and optical properties of the doped quantum dots. Shchekin et al. showed that the presence of doping-induced excess carriers can increase the number of certain kinds of defects because of the free carrier influence on interdiffusion occurring during the dot overgrowth [48]. For example, in a p-doped structure, the concentration of interstitials will increase, which leads to a positive charge. Thus a small number of point defects can result from p- or n-doping [49, 50]. However, to date the exact nature of the defects produced during the doping process is still unclear.

Despite the potential for applications, only a few studies of carrier dynamics in modulation doped QD structures have been reported [18, 45, 51]. The details of the carrier capture and subsequent relaxation is not clear, and the relevant energy relaxation mechanism

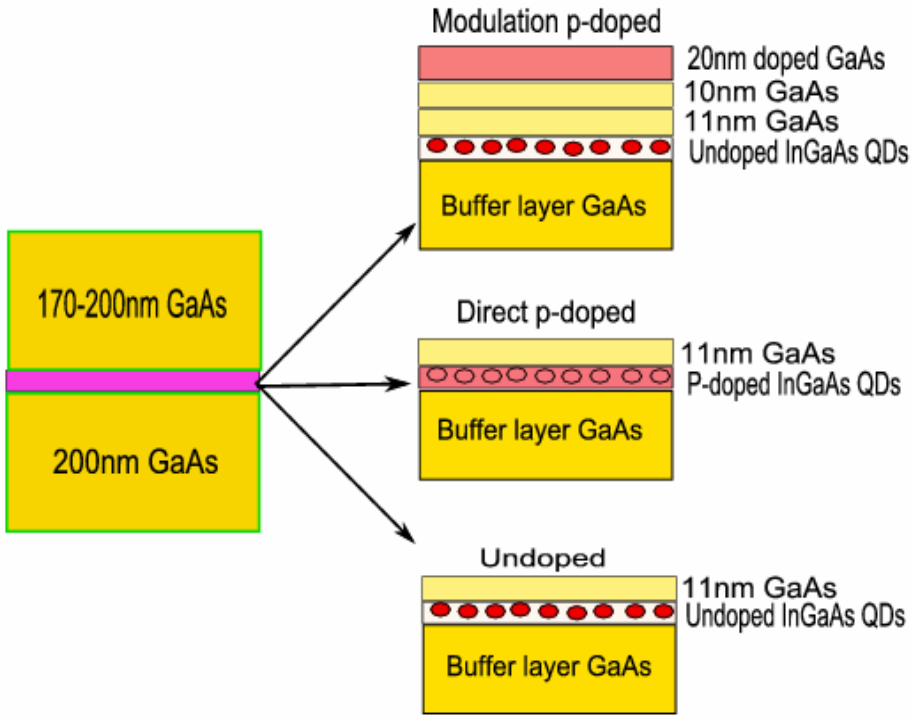

Figure 5-2 Structures of undoped, direct p-doped and modulation p-doped InGaAs QDs

is very controversial and under debate. In this chapter we study the electron dynamics in InGaAs SAQDs with different p-type doping and undoped samples using time integrated and time resolved PL.

5-1-1 Experiment

InGaAs/GaAs QD and InGaAs/InP QW samples used in this work were provided by Ms Sudah Mokkapati and Mr. Paulus Lobo Gaoso from the group of Professor Chennupati Jagadish at the Australian National University. The QD samples include undoped, direct p-doped and modulation p-doped samples (figure 5-2). Each of the samples was grown on a semi-insulating (100) GaAs substrate by low-pressure metalorganic chemical vapour deposition for structures of direct doping, modulation doping and without doping. For the undoped sample, 200 nm of GaAs buffer layer was first grown at 650℃ on a semi-isolated GaAs substrate, followed by $In_{0.5}Ga_{0.5}As$ dots grown and capped with 11 nm GaAs at 550℃. After a 1 minute interruption, the sample was capped with 200 nm of GaAs as the temperature was ramped to 650℃. The direct p-doped sample was grown under the same conditions as the undoped sample except the QDs were grown with a CCl_4 flow at 4×10^{-6} Torr at 550℃. For the modulation p-doped sample, after a 200 nm GaAs buffer layer, undoped $In_{0.5}Ga_{0.5}As$ dots, 11 nm capping layer and a 1 minute interruption, 10 nm GaAs was grown as the temperature was ramped to 650℃. Then a 20 nm thickness of doped GaAs (III/V ratio of 0.70) was grown at 650℃ with a CCl_4 flow at 5×10^{-7} Torr. Finally, 170 nm undoped GaAs was capped at 650 ℃.

Time integrated PL (CWPL) was performed at 77 K and room temperature using two kinds of laser excitation, a 532 nm laser as a continuous stable excitation source and 800 nm femtosecond pulses for high intensity excitation. A cooled InGaAs photodetector was used at the output slit of a 0.25 m monochrometer. The time-resolved PL experiment was performed with a PL up-conversion technique, as described in chapter 2. The excitation laser has ultrashort pulses with duration 80 fs, pulse energy 1-10 μJ and repetition rate 1 kHz. The luminescence from the sample was collected in a backward geometry and mixed in a BBO crystal with a variable delayed gating pulse (800 nm, 80 fs, 20 μJ) to generate a sum-frequency signal. The up-conversion system has a time and spectral resolution of 150 fs and 2 nm, respectively.

5-1-2 Time integrated photoluminescence

Figure 5-3 shows the PL spectra of the undoped (a), direct doped (b) and modulation doped (c) samples excited by a 532 nm laser at a low intensity of 2 mW at 77K. Each of the spectra can be fit well with a single Gaussian function, which is attributed to the ground state transition. A clear blue shift is observed for the p-doped samples, with 9 meV (b: direct doped) and 29 meV (c: modulation doped), compared to the undoped sample (centre 1070 nm), which suggests substantial carrier accumulation inside the QDs. Several groups have observed and

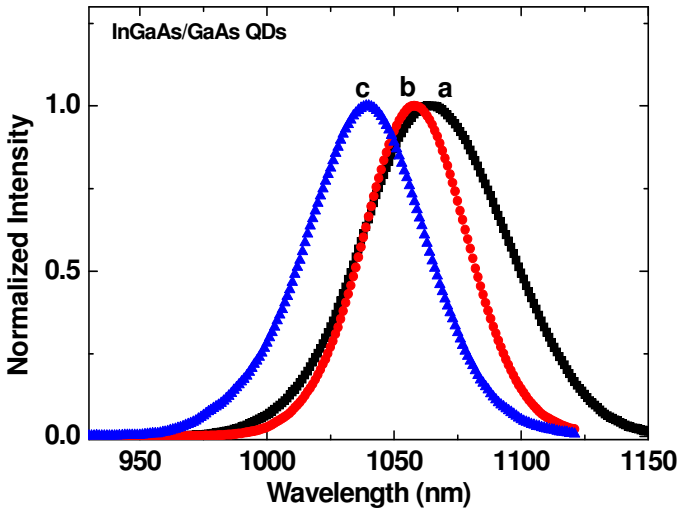

Figure 5-3 Integrated photoluminescence of InGaAs/GaAs QDs with the undoped (a), direct p-doped (b) and modulation p-doped (c) samples at 77K and low excitation

theoretically studied the spectral shift from charged QDs [52-54]. Regelman et al. demonstrated that, unlike higher dimensionality charged collective states, positively charged dots show an increase in emission energy, because the energy associated with hole-hole repulsion is larger than the energy associated with electron-hole attraction, which in turn is larger than the energy associated with electron-electron repulsion. Thus, the emission due to radiative recombination of an electron-hole pair is shifted to the blue. Compared to the undoped sample, charged QDs will create an extra multi-particle recombination energy, as shown schematically in figure 5-4 [53].

With increasing doping density, the probability of holes present in a QD increases, so the probability of multi-particle recombination increases. This leads to an increasing blue shift.

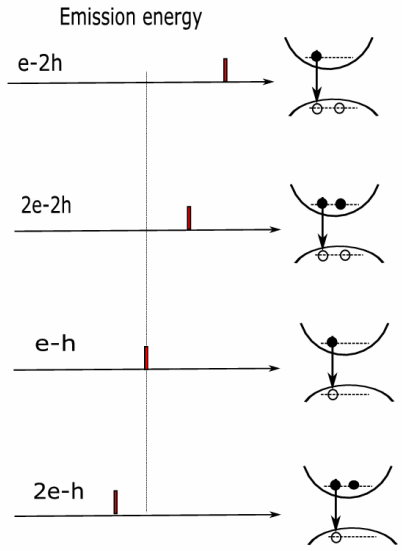

Figure 5-4 Emission energy shift for charged quantum dots. Positive charged QDs will create extra multi-particle recombination energy and thus a blue shift is observed in the p-doped sample

At a low excitation intensity many-body effects, such as bandgap renormalization and state filling, can be neglected. Basically, the dot size is an important effect for shifting the emission energy. Each of the samples has a very similar dot size based on a very similar growth process (the only difference is the modulation doping layer after the dot growth), so the reason for this blue shift should be extra holes in the QDs. Thus, the higher the doping density, the larger the blue shift. The experiment shows a smaller blue shift in the direct doped sample compared to the modulation doped sample, which can be attributed to a lower doping density in the direct doped sample. This is consistent with other studies [51, 55].

With increasing laser excitation intensity, an obvious asymmetry appears on the high energy side of the CWPL, which can be attributed to a state filling effect [56]. At 52 mW laser excitation, the PL contribution from the excited state transition can be clearly observed. The CWPL spectrum for each sample is well characterized by a two Gaussian fit for high excitation, where the centres of the Gaussian functions can be attributed to transitions from the ground state and from the first excited state, respectively, as shown in figure 5-5 for the

undoped sample. The inset shows the spectra for high excitation intensity for the undoped, direct doped and modulation doped samples. Energy separations between the ground state and excited states of 62, 53 and 57 meV are deduced for the undoped, direct doped and modulation doped samples, respectively. For these excitation conditions, we do not find any other component from the higher excited state or wetting layer.

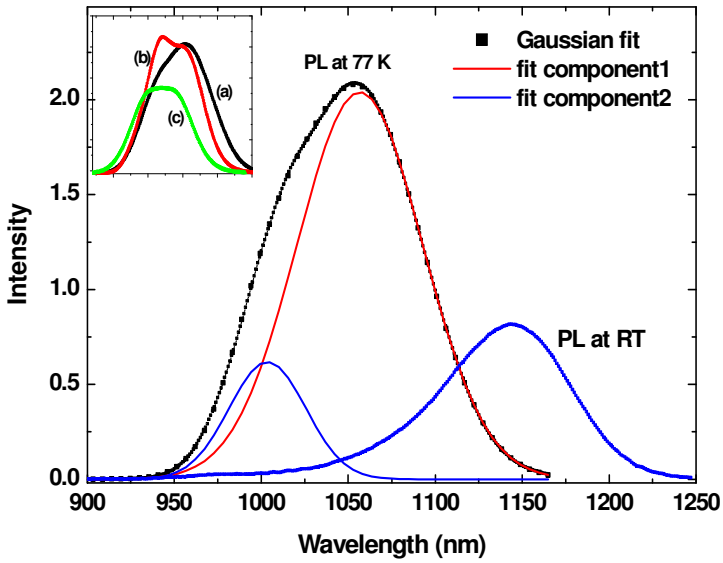

Figure 5-5 PL spectra of undoped QDs at high excitation. An obvious contribution of the excited state can be observed with a Gaussian fit. At room temperature, the PL spectrum shifts to the red and broadens. The inset shows the spectra of undoped (a), direct doped (b) and modulation doped (c) for high excitation at 532 nm

At room temperature and at the same high excitation, in addition to a red shift and a decrease of intensity, the contribution from the excited state decreases relative to the ground state. A weak contribution from the higher excited state is observed due to strong thermal activation, as shown in figure 5-5 for the undoped sample. A similar room temperature spectrum is also observed for the other two samples.

It is possible to observe the higher excited state or wetting layer, even the GaAs barrier, with femtosecond laser excitation. With increasing laser excitation intensity, peaks from the ground state, excited states, wetting layer and GaAs barrier sequentially appear, as shown in figure 5-6 for undoped (a) and direct doped (b) samples. In the figure, arrows indicate the ground state transition of the QDs and WL, respectively. At 77 K, the WL of both the undoped and modulation doped samples appears at 925 nm (1.338 eV), which results from the

identical conditions of the dot growth. The variation of spectral shape with excitation intensity is similar for these two samples. On the other hand, the wetting layer of the direct doped sample significantly shifts to the red side, with 980 nm (1.263 eV). Basically, the wetting layer is regarded as a thin quantum well; therefore, its emission wavelength depends not only on the composition but also on the thickness, which determines the quantum confinement energy. During InGaAs dot growth of the direct doped sample, the composition is affected by the doping atom and may slightly affect the strain and thus the thickness of the wetting layer. An energy shift of the WL results from the doping process and this shift leads to significantly different state filling features, as shown in figure 5-6.

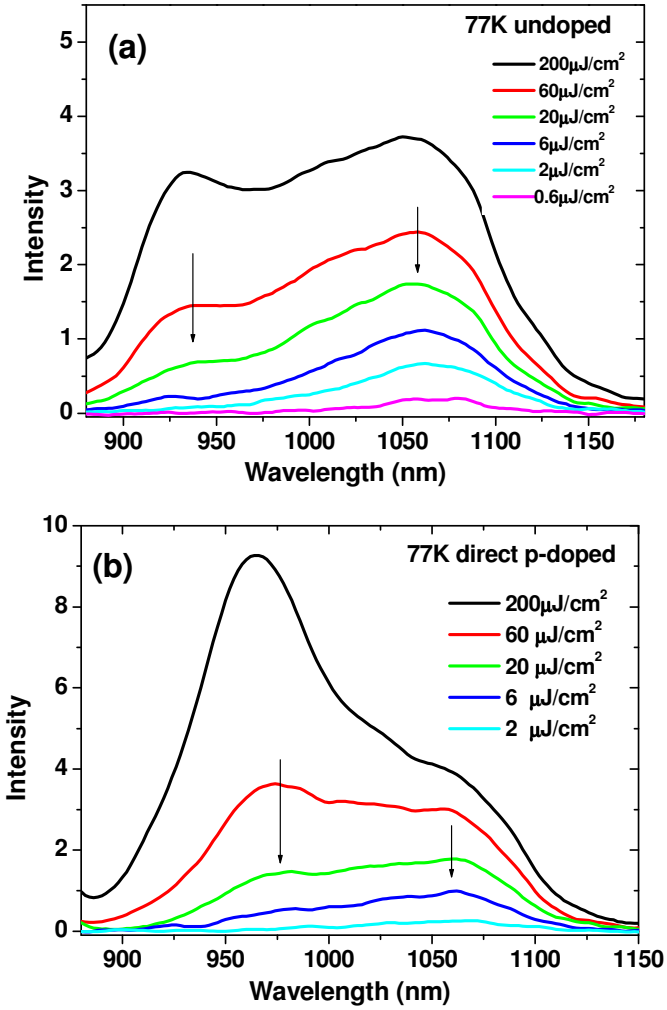

Figure 5-6 Variation in the PL spectrum excited at 77K by a femtosecond laser for the undoped (a) and direct doped (b) samples. Arrows indicate the positions of the ground state and WL transitions. Significantly different WL is clearly observed

5-1-3 Time-resolved photoluminescence

Figure 5-7 shows the evolution of the PL for the ground state transitions of undoped (a) direct doped (b) and modulation doped (c) samples excited at 800 nm at 77 K and 293 K, respectively. Each PL evolution can be fit with an exponential function $A[\exp(-t/\tau_D)-\exp(-t/\tau_R)]$, with decay time τ_D and rise time τ_R. We deduce the rise time and decay time of the three samples from the fitting (table 5-1). At low temperature, in

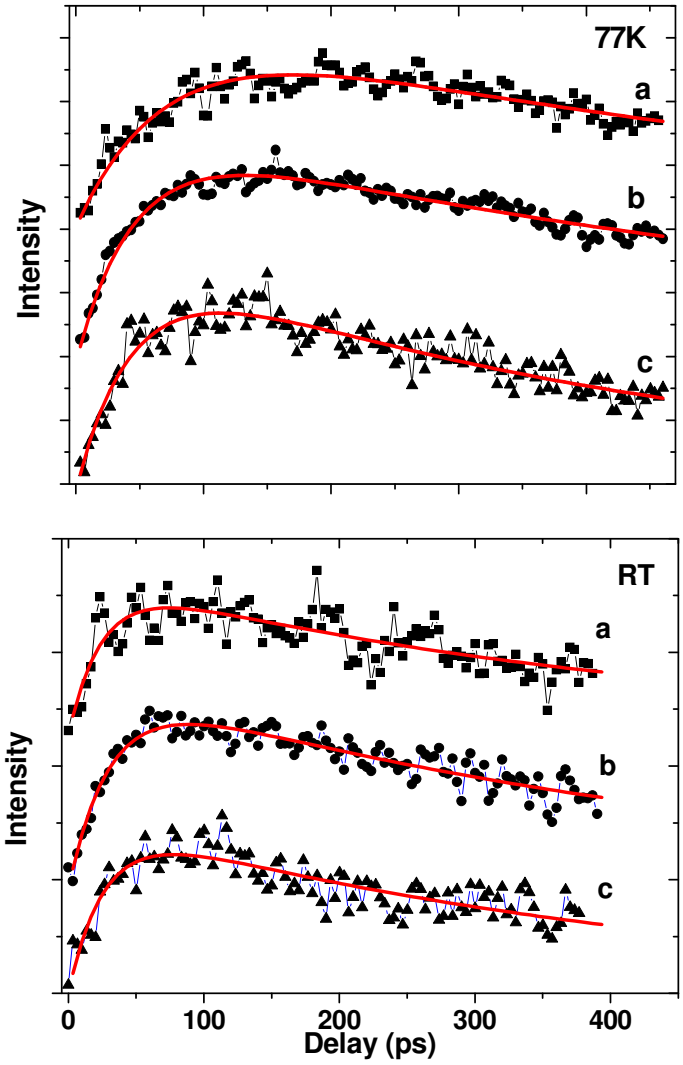

Figure 5-7 Evolution of PL for the ground state transition for undoped (a), direct doped (b) and modulation doped (c) samples with low intensity excitation of 800 nm at 77 K and 293 K

comparison with the undoped sample, the modulation doped sample has a significantly shorter rise time, while the direct doped sample gives a slightly shorter rise time. A slightly shorter rise time of the excited state transition is observed for each sample. At the same time, we obtain almost the same decay time for both ground state and excited state transitions for each sample.

When the temperature increases to room temperature, the rise time of the undoped sample significantly shortens. On the other hand, the rise time of the modulation doped sample changes only slightly. At room temperature, the undoped sample gives the shortest rise time, followed by the direct doped sample. As for the decay time, those of the undoped and direct doped samples shorten significantly at room temperature; so that the three samples have similar decay times at room temperature.

Table 5-1 Rise times and decay times of the three samples at 77 K

Sample	Undoped		Direct p-doped		Modulation p-doped	
Decay or rise time	τ_D (ps)	τ_R (ps)	τ_D (ps)	τ_R (ps)	τ_D (ps)	τ_R (ps)
Ground state	750	65	620	50	400	35
Excited state	730	55	610	45	400	25

Table 5-2 Rise times and decay times of the three samples at room temperature

Sample	Undoped		Direct p-doped		Modulation p-doped	
Decay or rise time	τ_D (ps)	τ_R (ps)	τ_D (ps)	τ_R (ps)	τ_D (ps)	τ_R (ps)
Ground state	455	23	445	28	395	30
Excited state	430	18	390	20	350	25

After 800 nm laser excitation, hot electrons and holes are generated in the GaAs barrier layer. A rapid LO phonon emission via Fröhlich interaction [13, 36] is expected due to the continuum band in the GaAs barrier; in this way electrons may rapidly relax into the ground state of the GaAs and the wetting layer. Then two relaxation channels are expected, through

which electrons relax into the ground state of the QDs. In the first channel electrons are captured directly into the ground state of the QDs from the WL, through either electron-electron scattering or electron-hole scattering. In the second channel, electrons are first captured into the excited states of the QDs and then relax into the ground state through intersubband relaxation, electron-hole scattering or phonon scattering.

There are many theoretical approaches which discuss the general possible relaxation mechanisms of carriers in self-assembled QDs [15, 16, 19, 28, 32]. Some of the experimental observations and theoretical studies have pointed out that carrier relaxation may be rapid taking into account Auger processes [29, 57], electron-hole interactions [18, 39] and the relatively slow relaxation from multi-phonon processes [19, 33, 58]. Gündoğdu et al. found that relaxation is significantly enhanced in p-doped InAs QDs due to efficient electron-hole scattering involving a built-in carrier population [18]. Siegert et al. studied carrier dynamics of modulation doped InAs QDs and different relaxation mechanisms were proposed [51]. However, the details of the relaxation mechanism depend sensitively on the features of the QDs, such as the composition, dot size, doping density, temperature, excitation intensity and wavelengths, etc, and it is difficult to identify the relaxation mechanisms from experiments. To date the physical mechanism involved in carrier relaxation in QDs and the influence of doping on the carrier capture and relaxation dynamics are still unclear and under debate [19, 24, 25, 33].

The primary difference between the samples is the different doping methods which can lead to a different doping density and may result in different relaxation mechanisms. According to our experiment, scattering between electrons and built-in holes most likely is the dominant relaxation mechanism in the modulation doped sample. In this way, electrons in the WL can transfer their energy to holes through scattering with holes of the ground state of the valence band and relax into QD states; holes are excited into excited states or the WL of the valence band. Due to the high effective mass of the holes, the QD level separation in the valence band is in the range of a few meV. This allows the holes to thermalize within several hundreds of femtoseconds through effective phonon emission. We expect hole scattering into the WL to be more efficient than scattering between discrete hole states because of the high state density in the WL. For the p-doped samples, built-in holes in the QDs result in efficient electron-hole scattering and thermal activation does not affect the relaxation rate. For the modulation doped sample, the higher doping density provides an effective scattering channel. The relaxation rate is related to the doping density, e.g., the

direct p-doped sample gives a slightly faster relaxation rate due to the low doping density. This is consistent with the observations reported by other groups [14, 18, 29, 42].

The PL experiment shows there is no obvious so-called phonon bottleneck in these InGaAs QDs. If the intersubband relaxation rate of the QDs is very low, PL peaks from both the ground state and excited states should be observed both at high excitation and low excitation intensity. However, both PL and TRPL experiments reveal that this intersubband relaxation is not very effective, because for each sample the rise time and decay time of the excited state transitions do not show obvious differences from those of the ground state. For the ground state transitions, the decay time is determined by the recombination between electrons and holes, while for the excited state transitions it is determined not only by the recombination rate but also by the intersubband relaxation rate. Thus in the case of effective intersubband relaxation, a remarkably different decay time is observed between transitions from the ground state and the excited states [14].

Phonon scattering is the likely dominant mechanism for the undoped sample due to the close separation of the hole levels and the availability of various energy-broadened phonons [22, 28]. In this case, a perfect match between the intersubband and LO phonon energies is not critical for a fast carrier relaxation. A fast carrier relaxation is possible even through multiphonon relaxation involving optical and acoustic phonons [14, 19, 34]. At low temperature, an ineffective phonon emission results in a slow relaxation rate. At room temperature, this phonon emission is strengthened and thus a significantly faster relaxation rate is observed.

From the time evolution of the PL, we deduce decay times of 750 ps, 620 ps and 400 ps for the undoped, direct doped and modulation doped samples, respectively. Generally, the lifetime of the ground state of the QDs is determined by radiative and non-radiative recombination. Because the structures of all samples are similar except for the doping, the lifetime should be related to the doping process or doping density. Experiment reveals that the lifetime of the doped samples decreases with doping density, which should result from a small number of dopant-related defects acting as nonradiative recombination centres as observed in other doped QDs [51, 59]. The exact nature of the defects is still unknown. Shchekin et al have shown that the presence of doping-induced excess carriers can increase the number of certain kinds of defects because of the free carrier influence on inter-diffusion occurring during the dot overgrowth [48]. For example, in a p-type doping structure, the concentration of interstitials will increase, which leads to a positive charge. Thus a small number of point defects could result from p- or n-doping [49, 50].

5-2 State filling effect in InGaAs quantum dots

The state filling effect is an interesting phenomenon that has been extensively investigated in various quantum structures using various techniques and gives detailed information about the optical and dynamical properties [60, 61]. However, only a few studies have been reported on the state filling effect and carrier dynamics of modulation doped QD structures. The influence of doping on the state filling effect and relaxation dynamics in these QD heterostructures is still not clear [18, 51, 62].

The atomic-like discrete energy states of QDs is expected to lead to a state filling effect due to the Pauli exclusion principle taking effect when only a few carriers populate the lower states. This will also lead to hindered intersubband relaxation and to the observation of excited-state interband transitions as the excitation intensity is increased.

Phonon bottleneck, state filling and segregated inhomogeneous broadening [56] can give rise to higher energy emission peaks, but they possess different characteristic features. The state filling effect is the only one which will show clear saturation effects. In a general experiment, the intersubband relaxation is significantly more efficient than the interband recombination of the corresponding excited state if there is no significant phonon bottleneck effect. Thus only the transition from the ground state is observed at low excitation intensity. With increasing the excitation intensity, a progressive saturation of the lower energy transitions is combined with the emergence of emission peaks originating from the excited state interband radiative transitions. The intersubband carrier relaxation toward the lower level is slowed down due to the reduced number of available final states. By contrast, the phonon bottleneck effect will permit excited state interband transitions even under low excitation conditions because the intersubband and interband relaxation dynamics are comparable. On the other hand, in the case of segregated inhomogeneous broadening, multiple peaks with the same relative amplitude are usually observed over a broad range of excitation intensity, since they reflect the relative abundance of a given ground state energy relative to the other available ground state energies in the probed area. Consequently, in the case of segregated inhomogeneous broadening in QWs, the energy position of the peaks can be observed following the energy predicted for a QW with a fluctuation of a few WL from its mean deposited thickness. By contrast, in self-assembled QDs the energy spectra of the excited states are typically quite different from the monolayer fluctuation energies due to lateral confinement [60].

The observed PL peak separation between the radiative recombination of adjacent excited states in self-assembled QDs is typically about 50-80 meV [63, 64]. This allows excited state transitions to be resolved in the presence of Gaussian inhomogeneous broadening which for self-assembled QDs typically has a full width at half maximum of similar size. This broadening arises from small fluctuations in the QD size, variation in alloy composition, and shifts due to strain-field effects. The major contribution to the inhomogeneous broadening comes from the variation of dot size due to the large confining potentials and the small volumes. However, due to self-organizing processes, segregated inhomogeneous broadening is not normally observed in InGaAs/GaAs self-assembled QDs. Under favourable growth conditions, alloy fluctuations can be minimized, and would certainly never lead to segregated inhomogeneous alloy broadening under normal conditions [56].

In addition, many-body phenomena such as biexcitons, charge excitons, exciton complexes, and band-gap renormalization can also contribute to the broadening at higher excitation intensities. However for a large ensemble of QDs they will be difficult to resolve in the presence of the above inhomogeneous broadening mechanisms, as they can only shift the emission energy by a few meV [41, 65].

The QD sample used in this work is similar to the modulation p-doped InGaAs/GaAs sample already described in section 5-1-1 except for a different dot size due to a different growth time and a III/V ratio of 0.4 in the doping process.

The CWPL spectrum excited by a low intensity (2 mW) 532 nm laser shows a good fit to a single Gaussian distribution (similar to the spectra of figure 5-5), which can be attributed to the ground state transition. No evidence of a phonon bottleneck is observed. The CWPL for high excitation (52 mW) shows evidence of asymmetry on the high energy side, which suggests saturation takes place in the ground state transition and the contribution of the excited state transitions increases. We can fit the CWPL with a multi-Gaussian function and deduce the locations of the ground state and the excited state to have an energy separation of 76 meV. However, the state filling effect is difficult to identify under these excitation conditions because the contribution of the excited states is markedly smaller than that of the ground state and inhomogeneous broadening is very large.

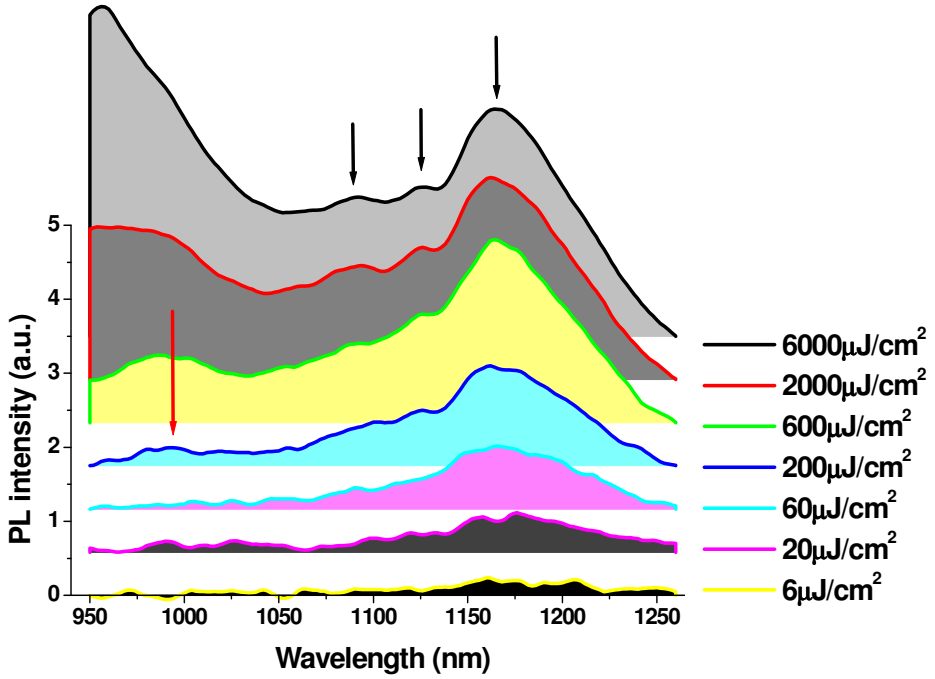

Figure 5-8 Time-integrated PL spectrum of modulation p-doped InGaAs/GaAs QDs excited by various intensities of 800 nm laser at room temperature

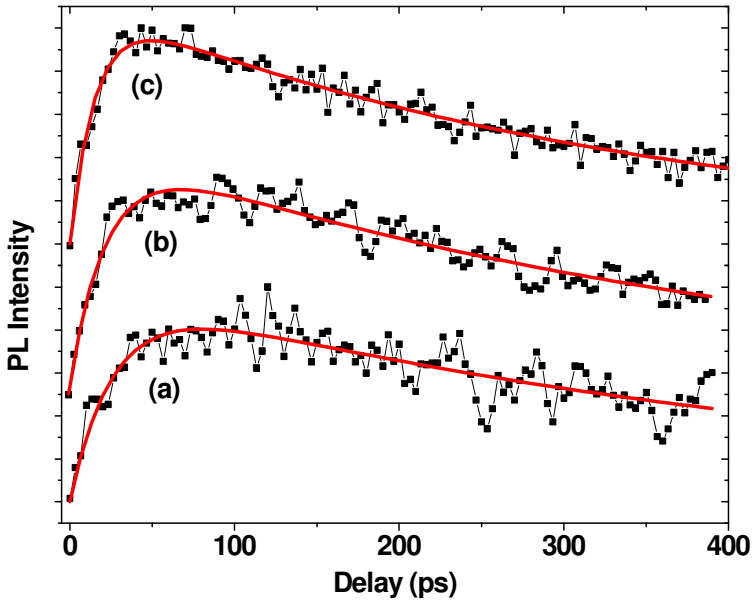

Figure 5-9 Evolution of PL of InGaAs/GaAs modulation p-doped QDs in the ground state (a), excited states (b) and (c) of the QDs. Solid lines are fits of an exponential rise and decay function

The high excitation experiment was performed using excitation by a 800 nm femtosecond laser. The spectra are shown in figure 5-8. At low excitation intensity, only the ground state transition is observed. This is similar to the PL spectrum excited by a CW laser. Both spectra indicate there is no clear phonon bottleneck. With increasing excitation intensity, in addition to transitions from the ground state, the transitions from the excited states and the WL are clearly identified, which suggests high energy peaks originate from a state filling effect rather than the phonon bottleneck. In this situation, the intersubband relaxation times of the QDs should be significantly shorter than the lifetime of the excited states, otherwise excited state luminescence should be observed even at low excitation intensity (phonon bottleneck effect). With further increase in the excitation intensity, the strong state filling effect leads to intense PL from the wetting layer.

The PL evolution is well fitted by an exponential rise and decay function $A \cdot [\exp(-t/\tau_D) - \exp(-t/\tau_R)]$, where τ_D and τ_R are the decay time and rise time, respectively. At 77K we deduce a rise time of 35 ps and a decay time of 600 ps for the ground state at an excitation intensity of about 30 μJ /cm^2. At room temperature, as shown in figure 5-9, the PL evolution of the ground state (a) and the excited states (b) and (c) at an excitation intensity of about 100 μJ/cm^2 is well fitted using an exponential rise and decay function. The squares correspond to the experimental data and the solid line represents the fitting curve. We deduce rise times of 30 ps for the ground state and 25 ps and 18 ps for the

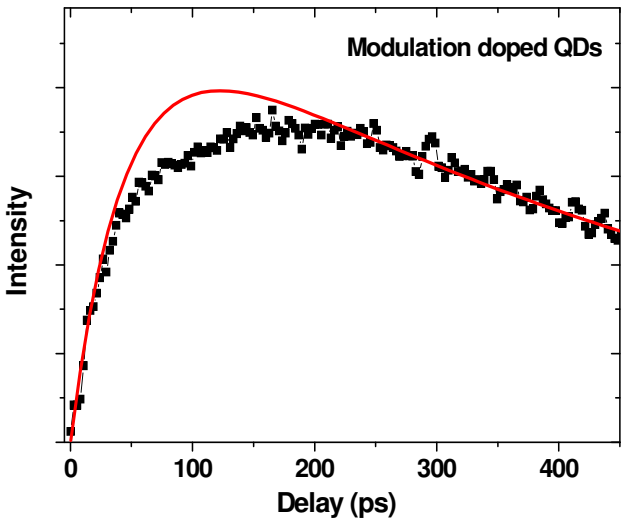

Figure 5-10 PL plateau at high excitation intensity indicates saturation due to state filling

excited states, and decay times of 445 ps, 390 ps and 340 ps, respectively. At high excitation, the PL evolution exhibits a non-exponential plateau, as shown in figure 5-10, which has been attributed to the state filling effect according to calculations and observations [60, 62].

For the p-doped QDs, the lowest few levels of the valence band are occupied prior to optical excitation. Basically, electrons are excited into the GaAs barrier under 800 nm laser excitation because the photon energy is larger than the band gap of the GaAs barrier. These photoexcited electrons then relax quickly into the low levels of the barrier and the InGaAs WL through effective LO phonon scattering. Electrons could be captured from the WL directly into the ground state of the QDs or firstly captured into the excited state of the QDs below the wetting layer before relaxing into the ground state of the QDs [41]. As discussed earlier and in other investigations [22, 26], the dominant relaxation channel for p-doped QDs is electron hole scattering. In this process electrons release their excess energy through scattering with holes built-in the valence band of the QDs. The hole energy states in the valence band are closely spaced and strongly broadened by phonon scattering, thereby providing a wide phase space of available energy conserving transitions.

The excitation intensity dependence of the PL evolution was measured at room temperature with 800 nm laser excitation. The PL evolution spectra can basically be fitted with an exponential rise and decay function. Figure 5-11 compares the rise time and decay time of the ground and excited states as a function of excitation intensity. The rise times of the ground state and excited state show a similar tendency, e.g., fairly long rise times of 60 ps and 40 ps appear at very low excitation intensity. The rise times decrease significantly with increasing excitation intensity until about 100 $\mu J /cm^2$, where the rise times are 30 ps and 25 ps for the ground state and excited state, respectively. With further increase of excitation intensity, however, the rise times do not show a further decrease.

At low excitation intensity, the electron states of the QDs are almost empty and therefore the state filling effect plays an insignificant role. On the other hand, the density of photoexcited electrons in the WL is very low so that the probability of electron-hole scattering is very low, and thus a long rise time is observed. With increasing excitation intensity, the density of photoexcited electrons increases and thus electron-hole scattering is enhanced, which leads to a decrease of the rise time. With increasing excitation intensity, however, the density of electrons in the QD states increases as well. The state filling effect begins to play an increasing role, which results in a reduced relaxation channel. With further increase of excitation, the state filling effect becomes the dominant mechanism, and thus the rise time does not shorten further although there is a sufficient density of electrons and holes available.

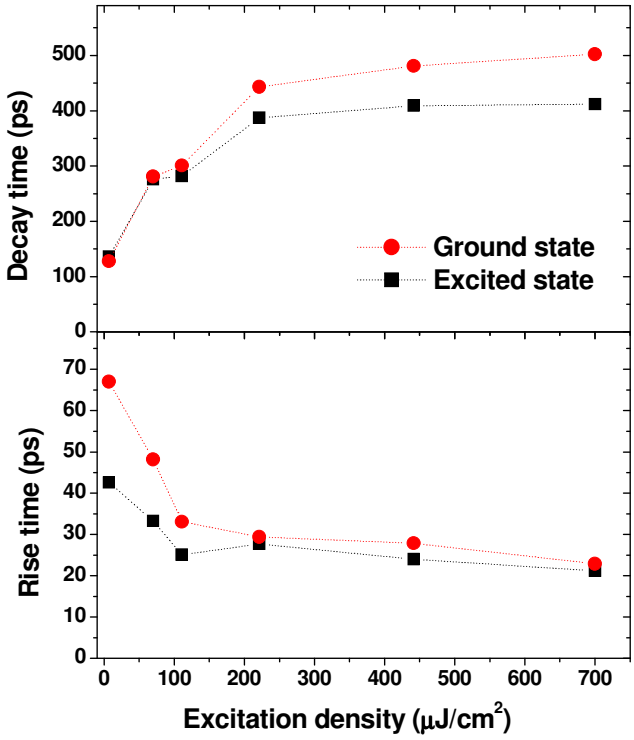

Figure 5-11 Rise time and decay time as a function of excitation intensity in modulation p-doped InGaAs/GaAs QDs. The circles and squares represent the ground state and excited state, respectively

Therefore, at low excitation, the rise time decreases with increasing excitation intensity due to enhancement of electron-hole scattering, whereas at high excitation the state filling effect results in reduced relaxation and thus a flat rise time variation.

As for the decay time, in principle, this is determined mainly by radiative and nonradiative recombination, and intersubband relaxation also makes a limited contribution for excited states because intersubband relaxation is not very effective in this doped sample. For the doped sample, the nonradiative centres are most likely a few defects introduced by the doping and these have a relatively short lifetime [45, 55]. For low excitation, nonradiative centres play the main role and thus a short decay time is obtained. With increasing excitation, the nonradiative channel appears to saturate due to the low density of the defects. Radiative recombination becomes the dominant mechanism and thus a long decay time is observed.

We present a simplified rate equation model to understand quantitatively the main microscopic processes involved in the observed PL transition in modulation doped

QDs [47, 66]. The PL intensity of the transition is proportional to the number of respective electron-hole pairs. For a p-doped QD discrete level system, the PL intensity for transition i is proportional only to the electron density N_i in the level i of the conduction band due to the excess built-in holes in the QD region prior to the excitation. The electron levels can be made to have an energy spacing as large as 80 meV, while the hole levels are much more closely spaced at 5-10 meV [67, 68]. The closely spaced hole levels result in thermal smearing of the hole population among many hole states. In this situation, the electrons have a high probability of residing in the ground level of the QDs and the injected electrons easily find holes with which to recombine due to the excess built-in hole population. Thus the transition wavelength difference could correspond to the energy spacing of the electrons, and the carrier capture is mostly related to electrons.

The carrier relaxation from j to i ($j > i$) is proportional to the non-occupancy of the level. The rate equation for level i can then be written

$$\frac{dN_i(t)}{dt} = -\frac{N_i(t)}{\tau_{el}^i} + \sum_{j>i} \frac{N_j(t)}{\tau_{rel}^{ji}} \frac{D_i - N_i(t)}{D_i} - \sum_{j<i} \frac{N_i(t)}{\tau_{rel}^{ij}} \frac{D_j - N_j(t)}{D_j} + G_i(t) \qquad (5\text{-}1)$$

where τ_{el}^i is the effective lifetime of the i th level, τ_{rel}^{ij} and τ_{rel}^{ji} are relaxation times between the i th and j th level of the electrons, D_i is the state density, $G_i(t)$ is the population captured from the WL and can be expressed as $\frac{\eta \sigma N_0 I_{ex}}{\tau_{Cap}^i} \cdot \frac{D_i - N_i(t)}{D_i}$, where τ_{cap}^i is the capture time, σ is the absorption cross section, I_{ex} is the laser intensity, N_0 is the total state density in the wetting layer and η is the capture efficiency. The factor $[D_i - N_i(t)]/D_i$ is a state filling factor which takes account of the fact that the electron can only relax to a lower-lying unoccupied dot level (Pauli blocking).

Equation (5-1) cannot be solved analytically and numerical calculation can provide a rough physical understanding. Based on the PL and TRPL experiments, electrons relax from the WL mainly through electron-hole scattering while intersubband relaxation is not very effective. According to the electronic structure of the WL and QDs, there are three electronic states below the WL. We set the parameters as follows: lifetimes of 500 ps, 450 ps and 400 ps for the i=1, 2, 3 electronic states; intersubband relaxation 100 ps; and capture time 30 ps.

Figure 5-12 shows the calculated results, where the red, green and blue curves represent the PL evolution of the ground state, the first excited state and the second excited state, respectively. At low excitation I_0 (a), the excited states have a short lifetime and small amplitude and thus a weak integrated intensity. With increasing excitation intensity, the amplitudes of the excited states increase, which results in an increase of the integrated intensity. With further increase of the excitation intensity, the PL evolution of the ground state deviates gradually from an exponential function and a plateau appears in the vicinity of the

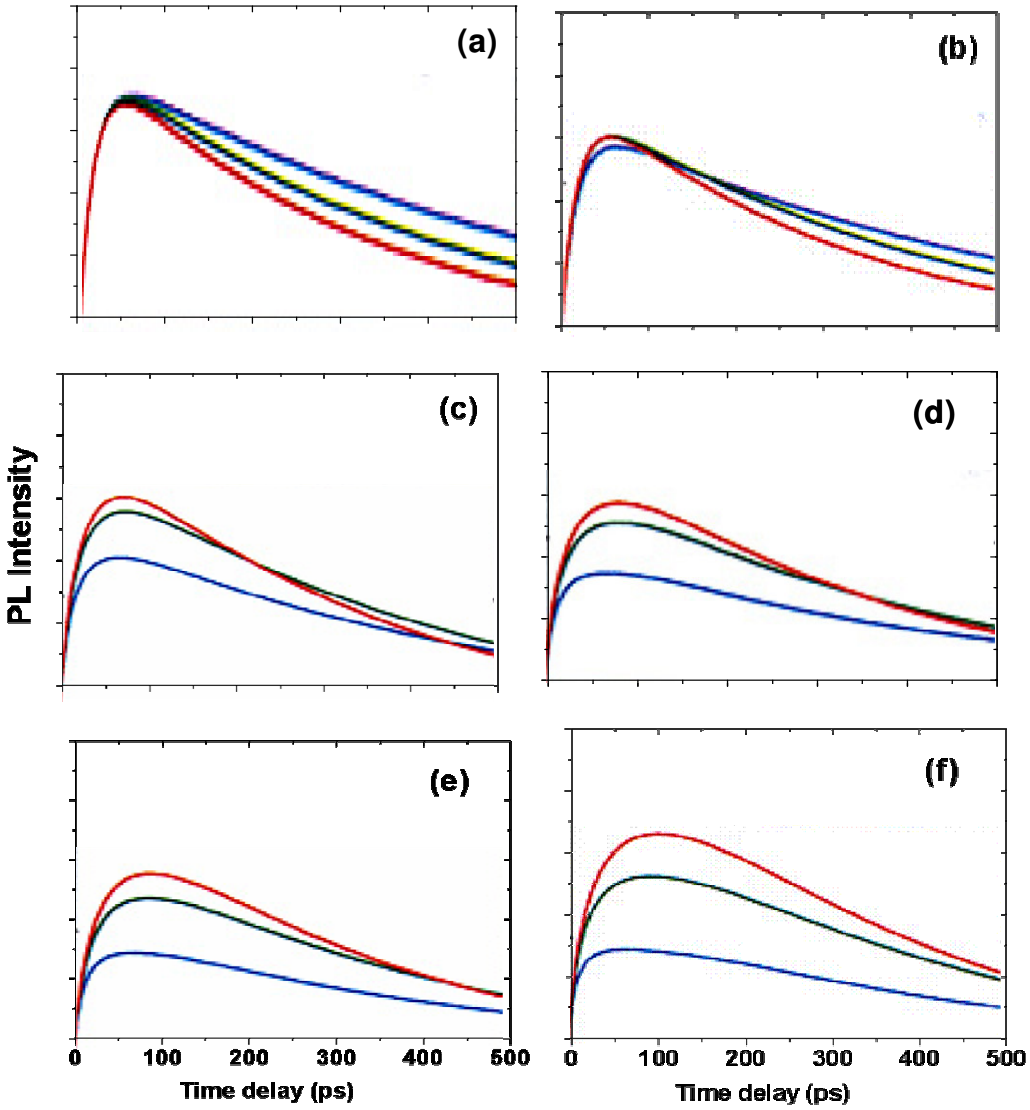

Figure 5-12 Numerical simulation for the rate equations for the ground state (blue) and excited state transitions (green and red) corresponding to different excitation intensities (a) I_0, (b) $5\,I_0$, (c) $15\,I_0$, (d) $25\,I_0$, (e) $30\,I_0$, (f) $40\,I_0$

maximum, which suggests strong saturation, followed by a plateau in the excited states, which is similar to the experiment (figure 5-10).

For the modulation doped QDs, electron relaxation from the WL is the dominant channel while intersubband relaxation plays only a minor role in the energy relaxation. It is reasonable to neglect the intersubband relaxation in equation (5-1), and the rate equations can then be written in a simple form

$$\frac{dN_i(t)}{dt} = -\frac{N_i(t)}{\tau_{el}^i} + \frac{\eta\sigma I_{ex} N_0}{\tau_{cap}^i}\frac{D_i - N_i(t)}{D_i} \tag{5-2}$$

At the maximum point of population N(t_m), the peak of the PL evolution, $dN_i(t_m)/dt = 0$, is satisfied. Thus the population of level i is found to be

$$N_i(t = t_m) \propto D_i/(1 + \alpha_i D_i / I_{ex}) \tag{5-3}$$

where $\alpha_i D_i$ is a saturation factor which depends on the level, and $\alpha_i = \tau_{cap}^i/(\sigma N_0 \tau_{el}^i)$. The

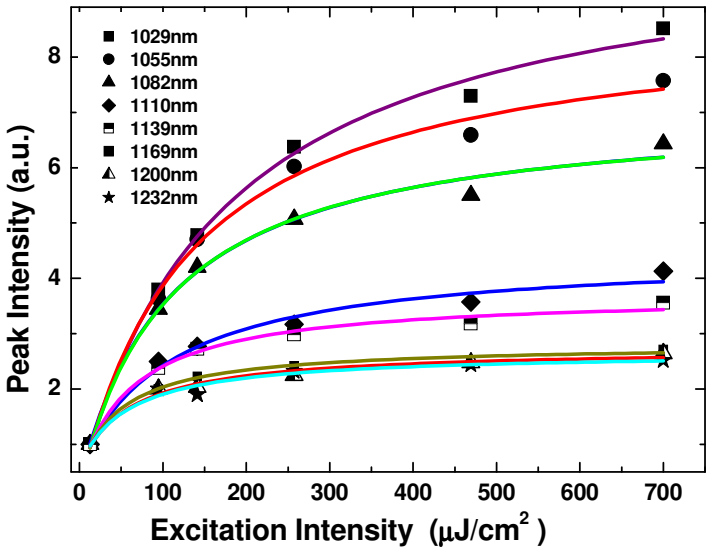

Figure 5-13 Peak intensity dependence of the excitation intensity at different detection wavelengths for modulation p-doped InGaAs QDs. The solid lines represent the best fits using equation (5-4)

corresponding intensity at the maximum point is given by

$$I^{i}_{\max}(I_{ex}) \propto \eta_{QEi} N_i \propto \eta_{QEi} D_i /(1+\alpha_i D_i / I_{ex}) \tag{5-4}$$

where η_{QEi} is the quantum efficiency.

We measure the excitation intensity dependence of the PL at different detection wavelengths and extract the peak intensity from the fitted curves, as plotted in figure 5-13. It is evident that a significantly different saturation occurs for the different wavelengths. In order to compare the saturation characteristics we fit the curves with equation (5-4) and deduce the saturation factor as a function of detection energy, as shown in figure 5-14.

The potential function of the QDs can be described by the expression $V_j = m^* \omega_j^2 r^2 / 2$ using a harmonic oscillator model for parabolic quantum confinement [69], where j represents an electron or a hole and m^*, ω_j and r are the effective mass, the frequency and the radial coordinate of the dots, respectively. The eigenenergies for a single electron or hole are given by $E^j_{lm} = \hbar\omega_j(2\ell + m + 1)$, where ℓ and m are the radial and angular momentum quantum numbers, and $\hbar = h/2\pi$ with h Planck's constant. The

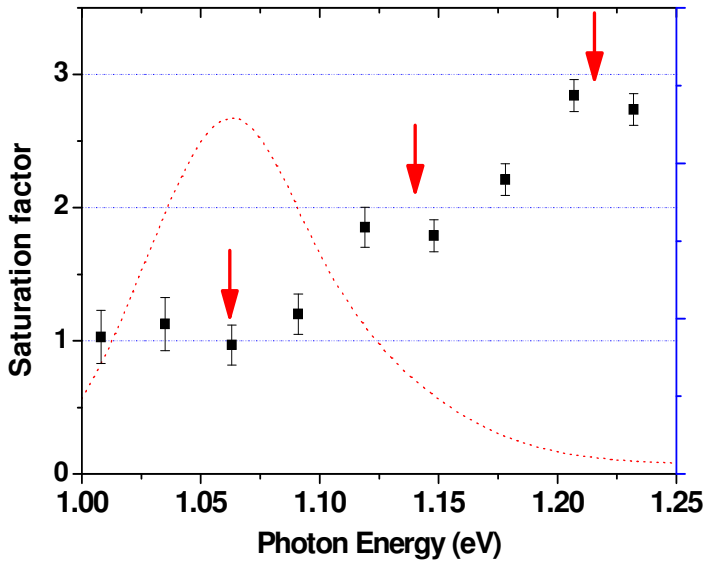

Figure 5-14 Saturation factor as a function of photon energy deduced from the time-resolved photoluminescence for the modulation p-doped InGaAs quantum dots. The arrows indicate the energy of the lowest three states of the QDs and the dotted curve is the corresponding PL curve

eigenenergies can also be written as $E_{lm}^{j} = \hbar\omega_j(i+1)$, setting $i = 2\ell + m$. The degeneracy of each state is $g_i = 2(i+1)$ with i=0, 1, 2,… when taking the spin degeneracy into account.

The saturation factor $\alpha_i D_i$ increases with increasing detection photon energy. Considering the ratio $\tau_{cap}^{i} / \tau_{el}^{i}$ can be weakly dependent on the dot levels we deduce the ratio of the saturation factor of the excited states to the ground state to be $\alpha_i D_i / \alpha_0 D_0 \propto g_i / 2 = i + 1$, with i=0 for the ground level. In other words, if the saturation factor of the ground state is normalized to be one then the saturation factor of the excited states can be expressed as $S(i) = 2, 3, 4\cdots$. Taking into account the inhomogeneous broadening of the QD ensemble, due mainly to fluctuations in dot size, the saturation factor should increase with increasing detection photon energy.

The saturation factors deduced from the excitation intensity dependence experiment are shown in figure 5-14 (squares). The dotted line is the PL curve and the arrows indicate the locations of the lowest three transitions according to the CWPL experiment. It is evident that the saturation factor increases with increasing detection energy, which is consistent with the prediction of the rate equations.

5-3 Implantation effect in InGaAs quantum wells

InGaAs/InP quantum wells have proven to be important semiconductor materials because of their potential in producing a laser that operates in the wavelength range 1.3 to 1.55 μm, which is suitable for long haul optical-fibre communication [70]. There has been a strong motivation in developing effective quantum well intermixing (QWI) technology to tune the quantum well properties at the post-growth level due to extensive applications in optoelectronics and photonics. It has been demonstrated that interdiffusion or intermixing in quantum confined structures is a simple alternative to selective area growth/re-growth for the fabrication of photonic integrated circuits. Intermixing leads to modification of the band gap as well as the optical and electrical properties of the quantum structures [71, 72].

During the past decades, many kinds of QWI techniques have been developed, such as plasma induced intermixing [73, 74], low-energy ion-implantation induced intermixing [75, 76], impurity induced disordering [77, 78], focused ion beam irradiation

[79-81] and laser induced disordering [82]. Implantation enhanced interdiffusion is one method of compositional intermixing that has the advantage of being able to modify in a controlled way buried heterostructures with a relatively simple processing step and effectiveness. Ion irradiation with subsequent thermal annealing has been shown to be very effective due to its advantage of precise control and reproducibility to generate intermixing by varying the irradiation parameters. Ion implantation enhanced interdiffusion has been extensively studied in InGaAs/InP systems using heavy ions but there have been fewer studies using protons [83-85]. In contrast to large atoms such as Al and Ga, protons may be useful for intermixing quantum wells that are far removed from the surface due to their light mass and rapid diffusion through the semiconductor during annealing, leaving few added atoms in the quantum well region [86, 87].

The carrier capture dynamics play an important role in the determination of the electronic and optical properties in quantum structures [88, 89]. Many groups have studied carrier capture and transport in intermixed QWs. To date carrier capture in InGaAs/InP, especially the variation of the electronic and optical properties by proton implantation enhanced interdiffusion, is still unclear due to the quite rapid and complicated process in the dynamics [90-92].

In this study we investigate atomic intermixing in the barrier/QW interface in $In_xGa_{1-x}As$/InP induced by proton irradiation. The carrier dynamics from the PL and TRPL experiments in the various strained InGaAs/InP QWs lead to a discussion of the mechanism of group V and group III interdiffusion in InGaAs/InP QWs.

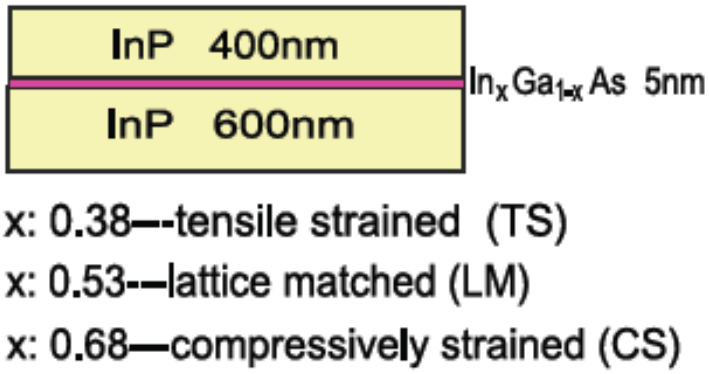

Figure 5-15 Structure of an InGaAs/InP quantum well

5-3-1 Experiment

The samples of $In_xGa_{1-x}As$/InP QWs used in this work were grown on a semi-insulating (100) InP substrate by low-pressure metalorganic chemical vapour deposition at 650℃. The indium composition was nominally x=0.38, 0.53 and 0.68 corresponding to tensile strained (TS), lattice matched (LM) and compressively strained (CS) QWs, respectively. Each structure consists of a 600 nm InP buffer layer, a 5 nm layer of $In_xGa_{1-x}As$ QW and a 400 nm InP capping layer, as shown in figure 5-15. Ion implantation was carried out with protons at 50 keV with doses of 5×10^{15} H/cm^2 and 1×10^{15} H/cm^2 and fluxes ranging from 0.26-0.55 $\mu A/cm^2$. TRIM simulation shows the damage peak is located in the vicinity of the QW layer for 50 keV. A reference was provided from a masked sample and was oriented 7^0 off from the proton beam axis to minimize channelling effects during implantation. Subsequent annealing was performed under Ar flow in a rapid thermal anneal (RTA) at 750 ℃ for 60 s. During the annealing process the samples were sandwiched using an InP proximity cap to minimize phosphorus loss from the sample surface. The PL and time-resolved PL experiments are the same as described in section 5-1-1.

5-3-2 Time-integrated photoluminescence

It is well known that quantum well/barrier interdiffusion affects the PL wavelength by changing the effective width of the well and, therefore, the energy of the confined levels, and also by modifying the well composition and band gap value [93, 94]. Figure 5-16 shows the PL spectra at 77 K for implanted TS, LM and CS QW samples annealed at $750°C$ for 60 s for doses ranging from 5×10^{14} H/cm^2 to 1×10^{16} H/cm^2. For the LM and CS QWs, each of the peaks corresponds to the recombination between electrons and heavy holes (HH) from the n = 1 subband levels (C-HH), while for TS QWs, the peak is related to the recombination of electrons and light holes (LH) from the n = 1 subband levels (C-LH) of InGaAs QWs. The peak position of a TS QW, which has a smaller indium composition than the other two samples, is at 1280 nm. This peak position is shifted to a higher wavelength of 1393 nm for the LM structure and 1555 nm for the CS structure, as the indium composition in the InGaAs QWs is increased. These changes in the peak position of the quantum wells are due to changes in the indium composition, and thus the lattice constant and the strain in the interface between the barrier and the QW. Also, it is worth noting that the high PL peak intensity and the narrow

and symmetrical lineshape of the peak emission of the samples are similar for LM, TS and CS, which indicates the smoothness of the interfaces and the homogeneous thickness of each of the InGaAs QWs after growth.

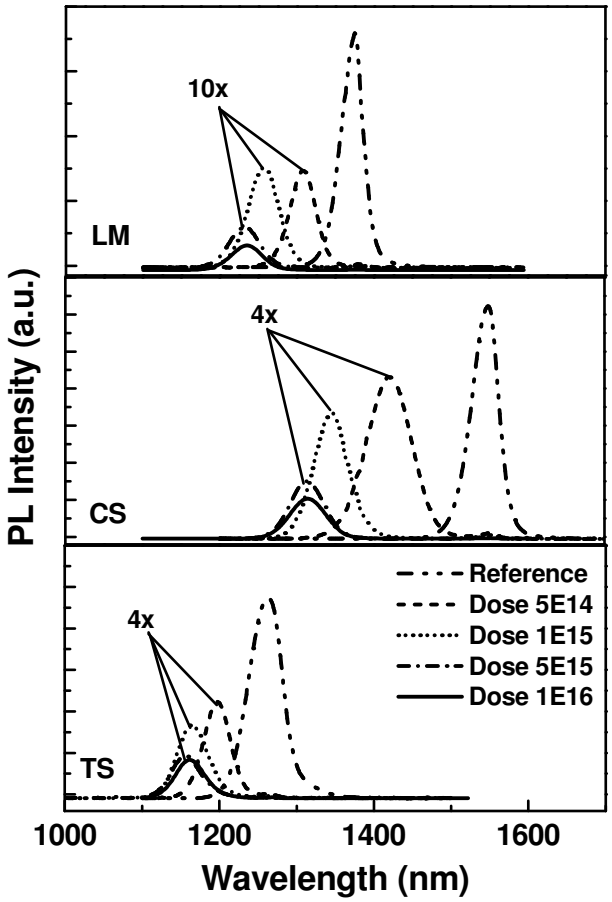

Figure 5-16 PL spectra of InGaAs QW samples with lattice matched (LM), compressively strained (CS) and tensile strained (TS) at 77 K

It can be clearly seen from this figure that after implantation a blue shift is observed for all implanted and annealed samples compared to the reference samples (unimplanted and annealed). However, the magnitude of the energy shift becomes saturated at high implantation doses, followed by a reduction of the PL intensity and a broadening of the PL lineshape. It is worth mentioning that, prior to annealing, the PL emission was too weak to observe due to defects formed after proton irradiation which act as non-radiative recombination centres. After annealing, the PL emission was recovered, but the PL intensities are still lower than for unirradiated samples, which suggests that defects are still present and not sufficiently removed

after annealing. Figure 5-17 shows the energy shift as a function of implantation dose for TS, LM and CS samples after annealing at 750 °*C* for 60 s. For each of the samples, the energy shift initially increases as the dose is increased, reaching a maximum at 5×10^{15} H/cm^2. As the dose is further increased to 1×10^{16} H/cm^2, a saturation in the energy shift is observed. These results are in contrast to previous studies of InGaAs/AlGaAs and AlGaAs/GaAs QWs using proton irradiation in which the energy shift was not saturated even at the highest doses

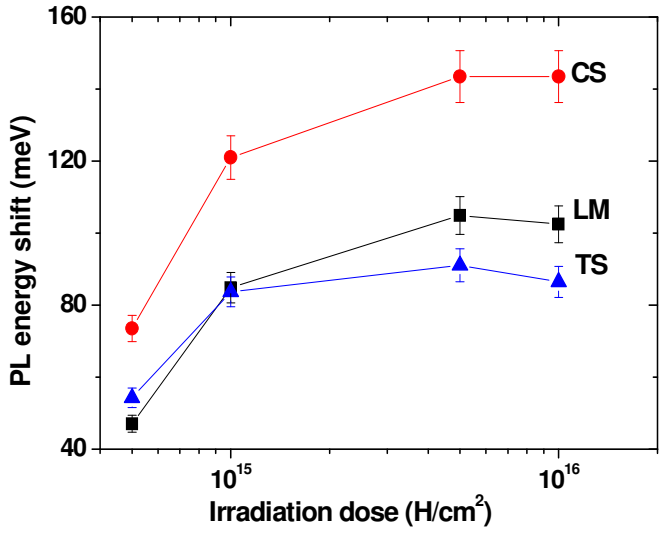

Figure 5-17 PL energy shift of lattice matched (LM), compressively strained (CS) and tensile strained (TS) InGaAs/InP QWs as a function of implantation dose after annealing

(5×10^{16} H/cm^2) [85]. The difference may be due to different types of defects formed in various material systems. In addition to this, it is well known that in AlGaAs/GaAs and InGaAs/AlGaAs systems the well-barrier interdiffusion during the annealing occurs only on the group III sublattice (In, Ga, Al). However, in the InGaAs/InP system both the group III and group V sublattices may contribute to interdiffusion. A blue shift is observed when the diffusion rate of the group V sublattice is larger than the diffusion rate of the group III sublattice, while a red shift is observed if the group III sublattice diffusion is dominant. At low doses, the results show that group V diffusion is dominant. At high doses, it is possible that the group III diffusion rate is enhanced (or there is a reduction in the group V diffusion rate), thereby leading to saturation in the blue shift. However, it is more likely that at high doses extended defects such as large clusters are formed and these defects are thermally more stable than simple point defects. Since only point defects (vacancies, interstitials) contribute to

the well-barrier intermixing, these clusters would result in lowering the concentration of available point defects to promote intermixing during annealing. Our results also consistently show that at high doses the recovery of the PL intensity is worse which strongly supports this argument. Protons create only point defects and dilute damage clusters whereas, in contrast, heavier ions create denser and larger damage clusters [95]. The denser and larger clusters result in the trapping of the available point defects to induce intermixing, particularly at higher doses. Therefore, a saturation effect of the energy shift is observed with increasing dose and is followed by a reduction in the energy shift. Indeed, this has been reported in several studies where heavier ions were used [96]. In addition, these results show that the concentration of residual defects after annealing is higher in samples implanted with heavier ions, resulting in poorer recovery of the optical properties.

The PL experiment also reveals that, at the same irradiation dose, the CS sample gives the largest blue shift, while the smallest blue shift is observed for the TS QW. It is expected that the group III sublattice diffusion rate will be highest for the TS samples since they have the highest In–Ga concentration gradient, followed by the LM and CS samples. Assuming that the group V sublattice diffusion rate is the same for all the samples, the higher group III diffusion rate of the TS samples would compensate the effect of the blue shift caused by the group V diffusion being more efficient than the group III diffusion in the other two samples. Hence, a similar energy shift is observed. However, this simplistic argument does not take into account the effect of the strain during interdiffusion. It is known that compressive strain may enhance the interdiffusion during annealing whereas tensile strain suppresses it [97].

5-3-3 Time-resolved photoluminescence

Figure 5-18 shows the time evolution of PL emission from the LM (a), CS (b) and TS (c) QWs for the unimplanted (reference) and implanted samples with doses of $1\times10^{15} H/cm^2$ and $5\times10^{15} H/cm^2$. The time evolution of the PL intensity $I_{PL}(t)$ can be fit with the equation

$$I_{PL}(t) = A\exp(-t/\tau_{LW}) - B\exp(-t/\tau_C) \qquad (5\text{-}4)$$

where τ_{LW} is the effective lifetime of carriers in the QWs, τ_C is the effective capture time of carriers in the QWs, and A and B are fitting parameters associated with the lifetime and effective capture time, respectively. As seen from the fitting results in table 5-3, the effective lifetime decreases as the implantation dose is increased. In the case of the TS samples, the PL lifetime of intermixed samples (5×10^{15} H/cm^2) is significantly decreased compared with the reference samples.

A smaller reduction of the effective lifetime (420 ps for reference samples and 220 ps for the sample implanted with 5×10^{15} H/cm^2) was measured for the CS sample. Reduction of the effective lifetime in an intermixed QW can be attributed to residual non-radiative defects in the quantum well or in the barrier layers after implantation and annealing. These defects act

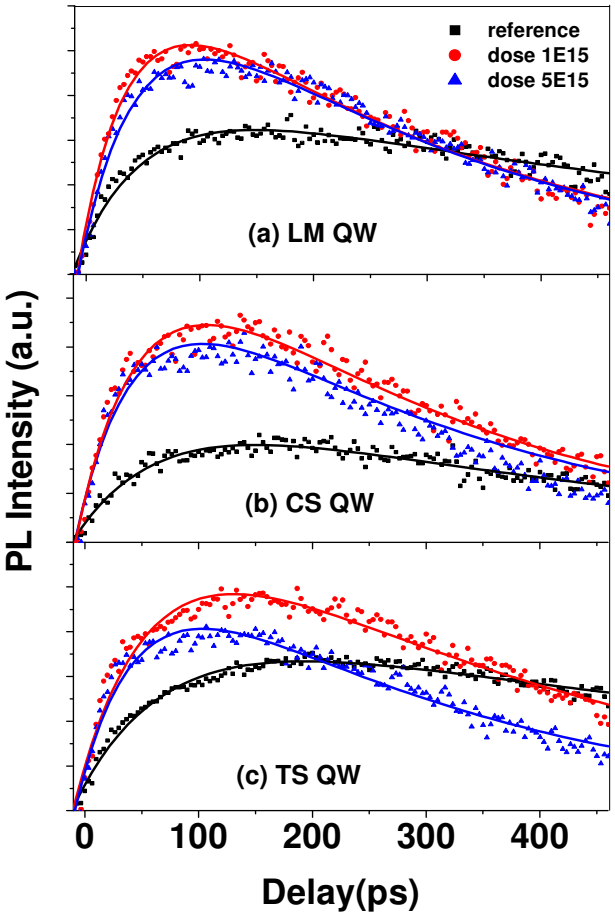

Figure 5-18 Time evolution of PL of InGaAs/InP quantum wells at room temperature for the reference samples and samples implanted with 1×10^{15} H/cm^2 and 5×10^{15} H/cm^2 with (a) lattice matched (LM), (b) compressively-strained (CS) and (c) tensile-strained (TS). The points are experimental data and the solid lines are fitted curves using equation (5-4)

as non-radiative centres thereby reducing the effective lifetime of the photoexcited carriers which has been reported in previous studies [98]. These results are consistent with the reduction of the CW-PL intensity and the broadening of the PL emission linewidth for intermixed samples.

Table 5-3 PL effective capture times (τ_C) and lifetimes (τ_{LW}) in the quantum well region for the reference and intermixed samples

Indium composition	Reference (as-grown+RTA)		Intermixed ($1x10^{15}$ H/cm^2)		Intermixed ($5x10^{15}$ H/cm^2)	
x	τ_C(ps)	τ_{LW} (ps)	τ_C (ps)	τ_{LW} (ps)	τ_C (ps)	τ_{LW} (ps)
0.38 (TS)	85	750	70	350	60	270
0.53 (LM)	60	700	45	290	55	280
0.68 (CS)	80	420	60	270	60	220

Table 5-4 PL effective lifetime of carriers localized in the barrier layer for the reference and intermixed samples

Indium composition	Reference (as-grown+RTA)		Intermixed ($5x10^{15}$ H/cm^2)	
x	A_1/A_0	τ_{LB} (ps)	A_1/A_0	τ_{LB} (ps)
0.38 (TS)	0.35	450	2.5	100
0.53 (LM)	1.2	410	0.4	110
0.68 (CS)	0.3	350	0	60

At room temperature where the origin of light emission in the quantum well region is due to the recombination of free electrons and holes, the PL rise time is determined by the rate of capture carriers into the QW. The effective carrier capture from the barrier into the quantum well consists of two processes, fast quantum capture (~1 ps) that involves carrier–carrier or carrier–phonon scattering and a longer process related to carrier diffusion across the barrier into the well. For this thick barrier layer, the carrier diffusion is much longer than the quantum capture and thus is dominant in the effective capture [90]. Although all samples have

the same barrier thickness, for the reference samples the capture times of the CS (80 ps) and TS (85 ps) samples are longer than those of the LM (60 ps) samples (see table 5-3). Because the thickness of the InP barriers is the same in all cases, the difference in the effective capture times for the CS, TS and LM samples suggests the presence of a 'potential barrier' at the hetero-interfaces due to strain and/or internal electric fields (i.e., concentration gradients).

Previous studies have shown that the carrier capture time in the quantum well is

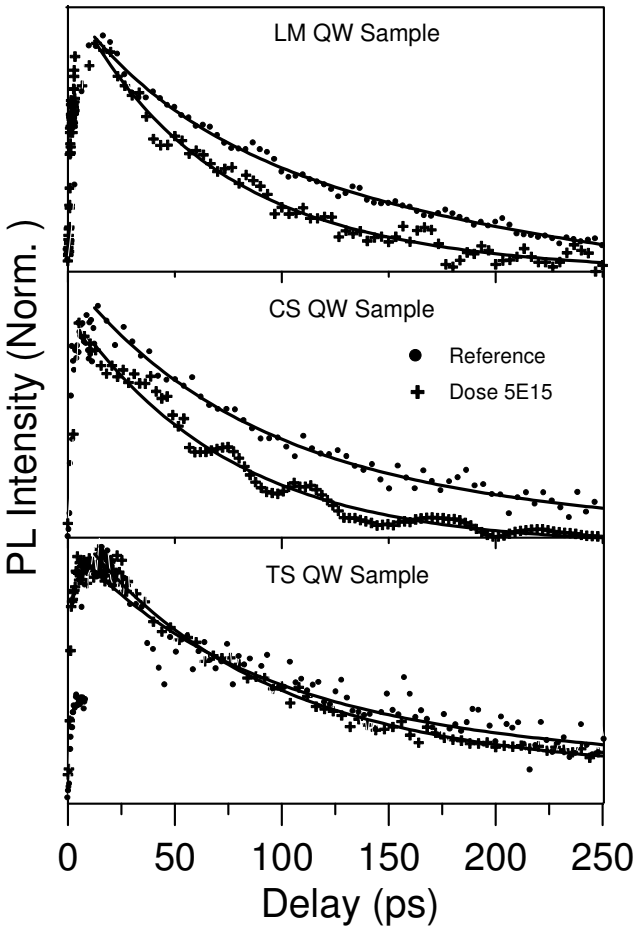

Figure 5-19 Time evolution of PL at 930 nm of InP barriers at room temperature for the reference samples and samples implanted with 1×10^{15} H/cm^2 and 5×10^{15} H/cm^2 with (a) lattice matched (LM), (b) compressively-strained (CS) and (c) tensile-strained (TS). The points are experimental data and the solid lines are fitting curves using a single exponential decay function

reduced in intermixed samples as a result of a change in the quantum well potential caused by intermixing [89, 99]. For samples implanted with 5×10^{15} H/cm^2, the effective capture times

are similar for all the samples (55–60 ps). The reduction in capture times after irradiation is due to a modification of the strain and the internal field profile. It is unlikely that the carrier diffusion/transport component of the effective carrier capture time is reduced since irradiation creates defects which will actually increase this transport component. This is further supported by the results when the irradiation dose is increased (i.e., more defects) and yet the effective carrier capture time is further reduced. At higher irradiation doses, this 'potential barrier' is reduced and hence the effective carrier captures times are shortened.

The influence of the additional potential energy barriers at the quantum well-barrier interface on the carrier capture can be studied from the time evolution of the barrier PL. After 800 nm laser excitation, hot electrons and holes are generated in the barrier layer. These hot carriers can release the extra energy into the band edge through LO phonons. Figure 5-19 shows the time evolution of the luminescence signal at 930 nm corresponding to the recombination of electrons and holes from InP barrier layers for the reference and intermixed samples (LM, CS, TS) at room temperature. Since the photoexcited carriers were generated in the barrier layer directly at 800 nm excitation, a very short rise time is observed at room temperature (~ 1 ps). In the barrier, the decay originates from two mechanisms: one is carrier capture into the QW and the other is the recombination of electrons and holes localized in the barrier. The decay time of the PL intensity can be fit with

$$I_{PL}(t) = A_1 \exp(-t/\tau_{LB}) + A_0 \exp(-t/\tau_C) \qquad (5\text{-}5)$$

where τ_{LB} is the effective lifetime of carriers localized in the barrier layer and τ_C is the effective capture time of carriers in the QWs which we deduce from the PL evolution of the QWs in table 5-3. A/A_0 reflects the contribution of localized states in the barrier which is dependent on the strain. The results of fitting for the reference samples and for the 5×10^{15} H/cm^2 implanted samples are summarized in table 5-4. The lifetimes of the localized carriers in the barrier were less than 100 ps for the intermixed samples which were much shorter than those for the reference samples. The ion-induced damage to the lattice can lead to a drastic reduction of its optical quality but with thermal annealing the heterostructures usually recovered most of their optical properties, although some defects were still left in the samples. Increasing the concentration of non-radiative defects leads to a shorter decay time of the barrier PL. This observation supports the additional potential energy barrier at the QW interfaces which can be reduced by intermixing. Atomic diffusion by intermixing leads to a reduction of the internal electric field at the interface.

5-4 Conclusion

Electron relaxation and recombination dynamics of InGaAs/GaAs p-type doped self-assembled QDs were investigated using time integrated photoluminescence and time-resolved photoluminescence. Under similar growth conditions, p-type direct doped, modulation doped and undoped self-assembled QDs samples were grown. A different blue shift is observed due to excess hole accumulation in the valence band in the doped samples. The modulation doped sample gives a higher doping density than the direct doped sample. No phonon bottleneck is observed in our experiments. Modulation doping results in a high density of excess holes in the valence band prior to laser excitation and thus electron-hole scattering becomes the dominant energy relaxation mechanism, whilst phonon or multi-phonon scattering is the main relaxation mechanism in the undoped sample. An obvious state filling effect has been observed in modulation doped InGaAs QDs. The rise times and decay times were found to vary with the excitation intensity. At low excitation intensity, increasing the density of photoexcited electrons leads to an increase of the probability of electron-hole scattering, which results in a decrease of the rise time. At high excitation, the state filling effect hinders the increase of rise time. The decay time of the doped samples decreases compared to the undoped sample due to defects introduced by the doping process. A simplified rate equation model shows that the doped QDs exhibit an increased saturation factor with increasing detection energy based on the theory of parabolic confinement of the quantum dots, which is consistently supported by the excitation dependence experiment of the TRPL.

Using time-integrated and time-resolved PL, we have observed a proton irradiation induced intermixing effect in InGaAs/InP quantum wells with different degrees of strain. For various strained QW samples, proton implantation leads to a blue shift of the PL peak, followed by a broadening of the PL linewidth and a reduction of the PL intensity due to residual defects acting as nonradiative centres. The time-resolved PL experiment on the QWs also supports this conclusion. At the same irradiation dose, the CS QW sample exhibits the largest blue shift and the TS sample the smallest blue shift. The time-resolved PL measurement indicates that the capture time of carriers in the quantum well region in which the rise time of the PL intensity is different for different quantum well structures with different strain and the carrier collection efficiency is enhanced in the intermixed QWs.

Chapter 6

Silicon quantum dots

6-1 Introduction

Silicon is the most important material in present-day microelectronics technology. It is well known that *bulk* crystalline silicon is an indirect band-gap semiconductor with an intrinsic band-gap in the near infrared region. In bulk silicon, the only possible scenario for interband optical transitions is that a phonon causes a vertical virtual transition at **k**=0 or 0.86π/a (where a is the lattice constant) with subsequent electron-phonon scattering processes, i.e., optical transitions are allowed only if phonons are absorbed or emitted to conserve the crystal momentum [1], as shown schematically in figure 6-1. In the optical absorption process, a phonon is emitted or absorbed to conserve the crystal momentum, $E_{electron} = E_{photon} \pm E_{phonon}$ and $\mathbf{k}_{electron} = \pm \mathbf{k}_{phonon}$. In optical emission, a similar process takes place, $E_{photon} = E_{electron} \pm E_{phonon}$ and $\mathbf{k}_{phonon} = \pm \mathbf{k}_{electron}$. In optical transition processes in bulk silicon, phonons play an important role, including transverse optical (TO) phonons (~56 meV) and transverse acoustic (TA) phonons (~18.7 meV) [1]. In recent years it has been shown that, accompanying the reduction in size of silicon nanostructures, such as in silicon nanocrystals and porous silicon, zero-phonon optical transitions are partially allowed and the oscillator strength of zero-phonon transitions is significantly enhanced. This increases the radiative recombination rate via a direct band-to-band recombination process [2-7]. The quantum confinement effect in silicon nanocrystals causes an enlargement of the band gap and efficient emission in the visible range at room temperature. The discovery in 1990 of efficient visible photoluminescence from silicon nanocrystals and porous silicon has attracted much attention because it can lead to the fabrication of light-emitting devices compatible with silicon-based optoelectronic integrated circuits and result in a new generation of silicon technology from microelectronics to optoelectronics [1, 8-12].

Extensive studies have been carried out in silicon nanostructures and impressive progress has been made towards understanding the nature of the efficient photoluminescence from silicon nanostructures. Many spectroscopy techniques have been used for exploring the

properties of silicon nanostructures, including PL, time-resolved PL, pump-probe and photon echoes amongst others [13-20]. However, many of the physical processes are still unclear and under debate, such as the mechanism of the visible emission, carrier capture and relaxation. In particular, the coherence properties of silicon nanostructures remain essentially unexplored due to the extreme complexity of these materials [1, 16, 21-23]. Silicon nanocrystal ensembles are heterogeneous in several aspects, such as the crystalline network configuration, the hydride or oxide surface passivation, which can influence the optical properties, and the residual size and shape distribution, which leads to large inhomogeneous broadening in the emission. This can obscure the inherent spectroscopic information.

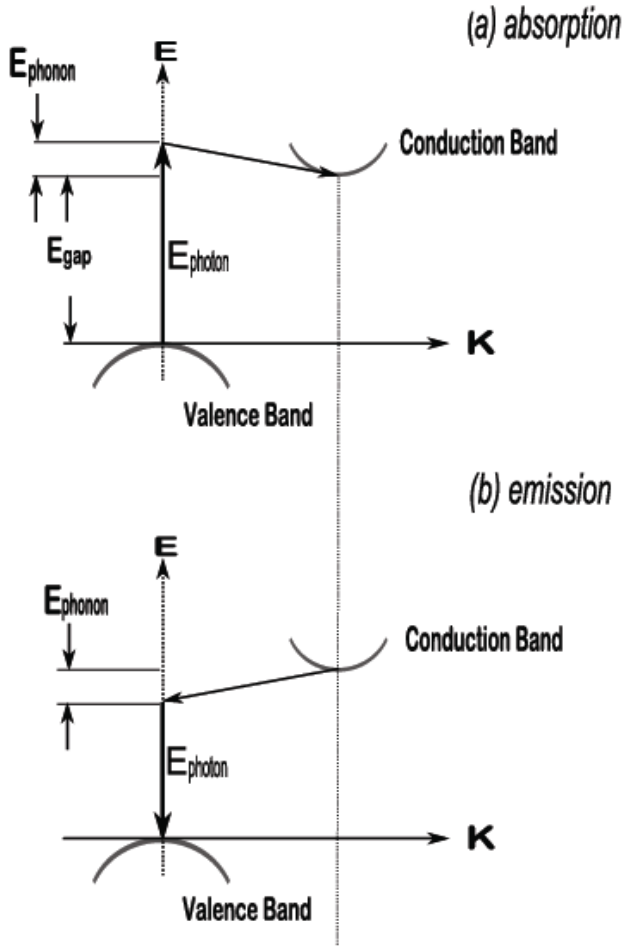

Figure 6-1 The band structure of bulk silicon and possible optical transitions

In this investigation, we study the optical properties of silicon quantum dots using various spectroscopies. With time-resolved and time-integrated photoluminescence we study the state filling effect which leads to discussion about the origin of the broad red band and parabolic confinement of quantum dot structures and the corresponding energy state splitting. Furthermore, using two-colour three-pulse photon echo spectroscopy for the special case of $t_{12} = 0$ (transient grating), we explore the ultrafast population relaxation of silicon QDs.

6-2 Experiment

The silicon quantum dot samples used in this work were provided by Dr. Eunchel Cho from the University of New South Wales. An excess of silicon in substoichiometric oxide, also known as silicon-rich oxide (SRO), i.e., SiO_x (x<2), generates silicon precipitations attributed to the diffusion of silicon atoms leaving the stoichiometric oxide (SiO_2) during high temperature thermal annealing [24]. A deposited SRO film is thermodynamically unstable below 1173 °C and phase separation and diffusion of the silicon atoms in the amorphous SiO_2 matrix creates nanoscale silicon quantum dots [25, 26]. The size of the silicon quantum dots depends on the thermal budget, film thickness, and stoichiometry of the SRO. In our experiment the silicon QD superlattices were fabricated by alternate deposition of silicon oxide and SRO with differing thicknesses. Conventional furnace annealing under a nitrogen atmosphere (1100 °C, 1 h) was performed to precipitate silicon and stimulate nanocrystalline silicon growth by the diffusion of silicon in the oxide. Only lateral silicon diffusion and silicon grain growth within thin SRO films enclosed by amorphous silicon oxide occurs so that the maximum size of the silicon quantum dots is determined by the SRO thickness. Figure 6-2(a) shows a transmission electron microscopy (TEM) image of eight layers of silicon quantum dots in an oxide matrix, where the dots in the white regions (glue) originate from particles collected during the TEM sample preparation. A typical high-resolution TEM image is shown in figure 6-2(b). The thickness of the SRO layer, and hence the size of the silicon quantum dots, was controlled by the deposition time and other optimized sputtering parameters (gas mixing ratio, deposition pressure, and rf power). The spacing or distance between the dots is determined by the amount of silicon in the SRO layer. The sample used in this study has an average dot size of 4.3 nm on a sapphire substrate, and the dot density is about $10^{12} - 10^{13}$ dots/cm^2.

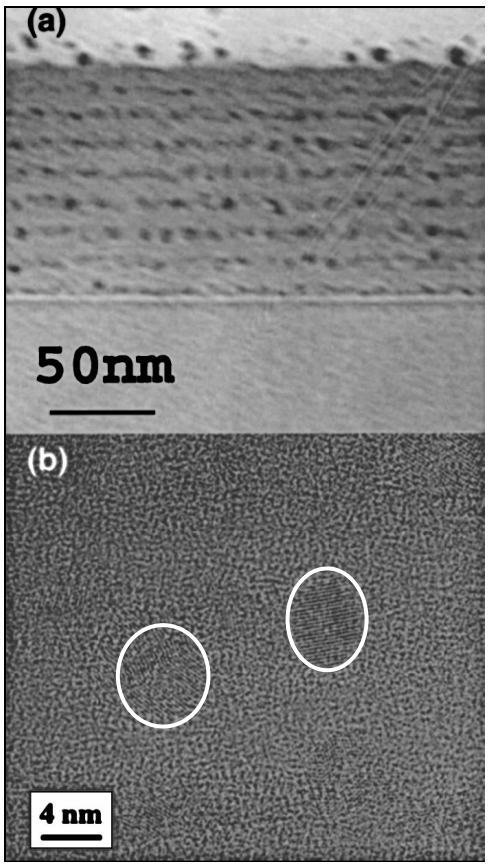

Figure 6-2 TEM image (a) and high resolution TEM image (b) of Si quantum dots in an oxide matrix

In the time-resolved and time-integrated PL experiments, the PL signal is dispersed by a 0.27 m grating spectrometer and detected with a PMT. The sample was mounted in a closed-cycle helium cryostat with a variable temperature in the range 15–300 K. For the time-integrated PL measurements the spectra were recorded using a lock-in amplifier. For the time-resolved measurements the response function of the PMT was reduced to have a time resolution of about 5 ns, which is much shorter than the decay time of the signals (in the microsecond range) and the signal was recorded by a 500 MHz digital oscilloscope. Two kinds of femtosecond pulses with 80 fs duration and similar average power were used for excitation. One has a 1 kHz repetition rate of pulses from an OPA, and the other has a repetition rate of 82 MHz from the femtosecond oscillator such that the excitation pulse separation of 12 ns is much shorter than the decay time of the PL signal. In the latter case, which can be regarded as continuous excitation, the peak energy density is much lower than the case of 1 kHz excitation. The excitation wavelength was tuned to 400 nm, which

corresponds to energy well above the band gap of the silicon QDs. Thus the excited carriers are generated in the SRO layer or in very high excited states of the QDs. The energy of the excitation laser pulses varies from 0.03 mJ to 2 mJ with a photon density of about $10^{13}-10^{15}$ photons/cm^2 in the low repetition rate case. Under these high excitation conditions we expect more than 10 electrons/dot can be generated by a single pulse [16].

The details of the photon echo experiment are described in chapter 2. In this experiment three ultrashort pulses are used. Two pump pulses with wave-vectors $\mathbf{k_1}$ and $\mathbf{k_2}$ and one probe pulse with wave-vector $\mathbf{k_3}$ are generated from two independently tunable OPAs. The OPAs are pumped by a 1 mJ amplified pulse (80 fs, 800 nm, 1 kHz) and tuned to give wavelengths in the range 600-750 nm where transitions between the energy states of the QDs are expected. Three beams with time delays t_{12} (between pulses $\mathbf{k_1}$ and $\mathbf{k_2}$) and t_{23} (between pulses $\mathbf{k_2}$ and $\mathbf{k_3}$) are aligned in a triangular configuration and focused by a 20 cm focal length lens on to the same spot (diameter 300 μm) where the sample is placed. The energy density of each pulse is about $1\ \mathrm{mJ/cm^2}$. The signal was detected in the phase-matched direction ($\mathbf{k_4 = k_1 - k_2 + k_3}$) by a spectrometer equipped with a CCD array (spectral resolution <1 nm) and measured for a range of fixed coherence times t_{12} or population times t_{23} by scanning the other delay time. Positive time is when the pulse $\mathbf{k_2}$ precedes $\mathbf{k_1}$ for the t_{12} delay or $\mathbf{k_3}$ for the t_{12} delay [19, 27].

6-3 Photoluminescence and time-resolved photoluminescence

6-3-1 Photoluminescence

Figure 6-3 shows PL spectra of the sample excited by 1 kHz pulses with various intensities at room temperature. A very broad PL band is observed ranging from 600 nm to 860 nm and centred around 750 nm with no clear structure [11, 28]，hereafter called the S-band due to the very slow decay time. This broad PL band has been observed by many other groups and its origin is still under debate. It is most likely due to the variable structure of the samples and the many possible states in silicon nanostructures [11, 29-34]. Many authors

favour a "pure" quantum confinement model in which the emission is due to electron-hole pair recombination [16, 35-38]. However, some other authors do not agree with this model, and they propose that this broad red luminescence originates from carrier trapping and recombination at surface Si=O bonds that produce stable states in the band gap [39-41]. More recently, Sychugov *et al*. [42, 43] have measured the micro-PL of single silicon QDs and found the luminescence linewidth to be less than the thermal broadening at low temperature, thus confirming the atomic-like energetic states of silicon QDs. The emission observed here mainly involves electron-hole recombination between QD states in the conduction band (CB) and the valence band (VB). The broad band is due to the strongly inhomogeneous dot size and thermal broadening, which leads to overlapping between the transitions from the ground and excited states.

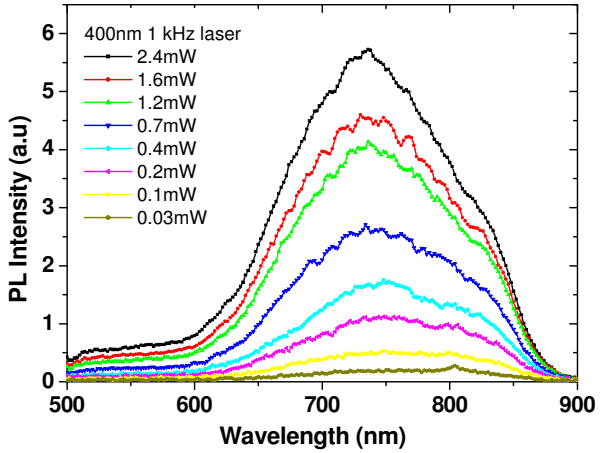

Figure 6-3 PL spectra of silicon QDs excited by the 1 kHz laser at various intensities

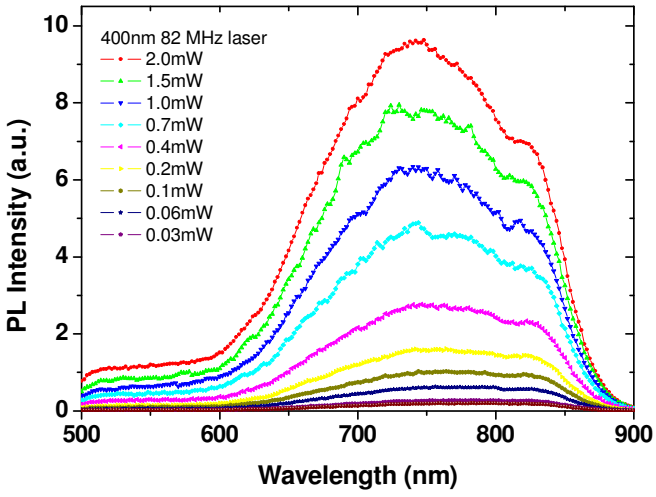

Figure 6-4 PL spectra of silicon QDs excited by the 82 MHz laser at various intensities

With decreasing excitation intensity, the PL intensity at the low energy part of the spectrum decreases more slowly than that of the high energy part and a small red shift of the maximum of the PL spectrum is observed (peak position at about 780 nm for 0.03 mW and 740 nm for 2.3 mW excitation (see figure 6-5). This most likely originates from the state filling effect. With increasing excitation intensity, the availability of the low energy levels of silicon QDs decreases due to the state filling, which leads to a significantly slower increase of carriers; that is, a saturation effect appears in the lower states of silicon QDs, as observed in many other QD systems [44, 45]. In order to identify the state filling phenomenon we performed the following experiments.

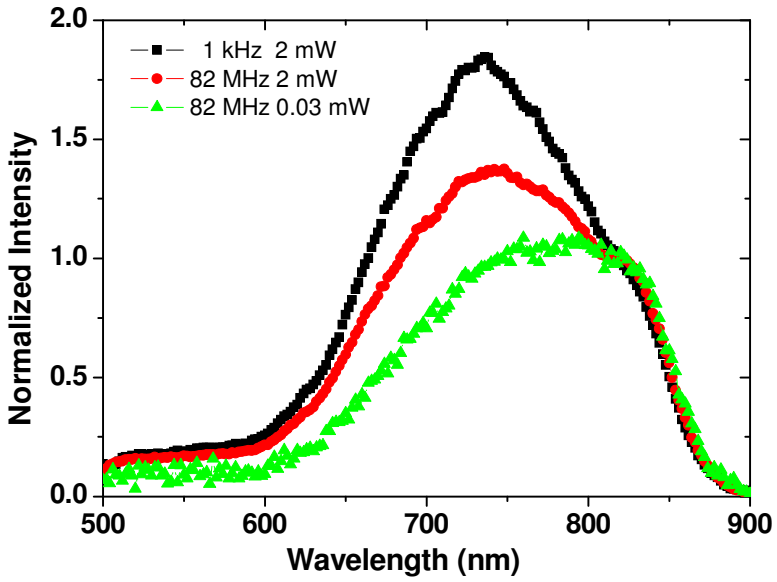

Figure 6-5 Comparison of PL spectra for different excitations at room temperature

We measured the PL spectra using the excitation laser with repetition rate of 82 MHz. In this case, the laser creates a continuum excitation due to the pulse separation being much shorter than the decay time of the silicon QDs, and thus a lower energy density and reduced saturation effect are expected and observed, as shown in figure 6-4. A peak can be seen at around 830 nm and the PL intensity is relatively high on the long wavelength side compared to the spectra excited by the 1 kHz laser. With decreased excitation intensity, this effect becomes even more pronounced. We compare the spectra following excitation by 2 mW from the 1 kHz laser with those for 2 mW and 0.03 mW excitation from the 82 MHz laser in figure 6-5. A red shift of the peak with decreasing excitation intensity is clearly seen. At the

low excitation of 0.03 mW, the intensity on the high energy side decreases significantly. A shoulder appears on the high energy side, corresponding to transitions from the excited states. The centre of the ground state transition of 835 nm can be identified.

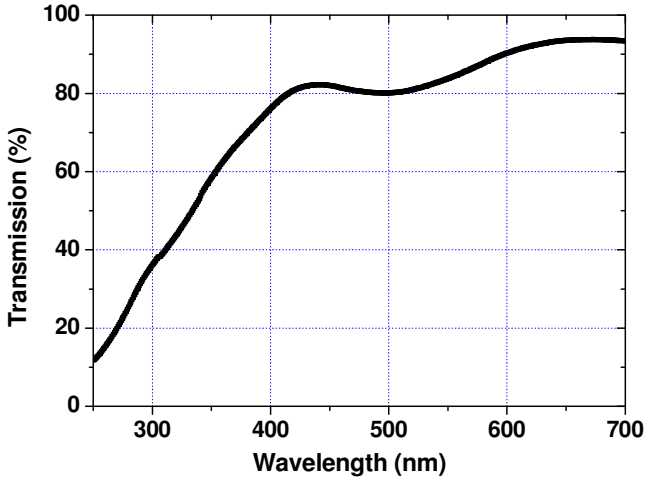

Figure 6-6 Transmission of Si QD sample at room temperature

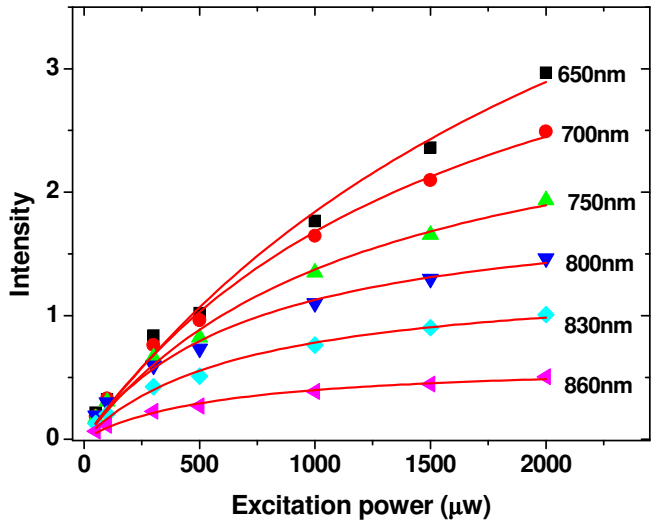

Figure 6-7 Excitation dependence of PL intensity taken from the PL spectra

As can be seen from figure 6-6 of the spectral transmission of the silicon QD sample, there is no obvious absorption structure between 500 nm and 700 nm and the absorption is fairly low. Following the discussion of the InGaAs state filling effect presented in chapter 5, we apply equation (5-2) to the state filling effect of the silicon QD sample. The case of 82 MHz laser excitation can be regarded as continuum excitation because the pulse separation of 12 ns is much shorter than the lifetime of the red band which is in the microsecond range. Therefore, the equilibrium condition $dN/dt = 0$ is satisfied. The carrier density in level i corresponding to an excitation intensity I_{ex} is given by

$$N_i(I_{ex}) \propto D_i/(1+\alpha_i D_i / I_{ex}) \tag{6-1}$$

where $\alpha_i D_i$ is a saturation factor which depends on the level, and $\alpha_i = \tau^i_{cap}/(\sigma N_0 \tau^i_{el})$. The corresponding time-integrated luminescence intensity can be expressed as

$$I^i(I_{ex}) \propto \eta_i N_i \propto \eta_i D_i/(1+\alpha_i D_i / I_{ex}) \tag{6-2}$$

where η_i is the quantum efficiency. Equation 6-2 provides a good fit for the intensity

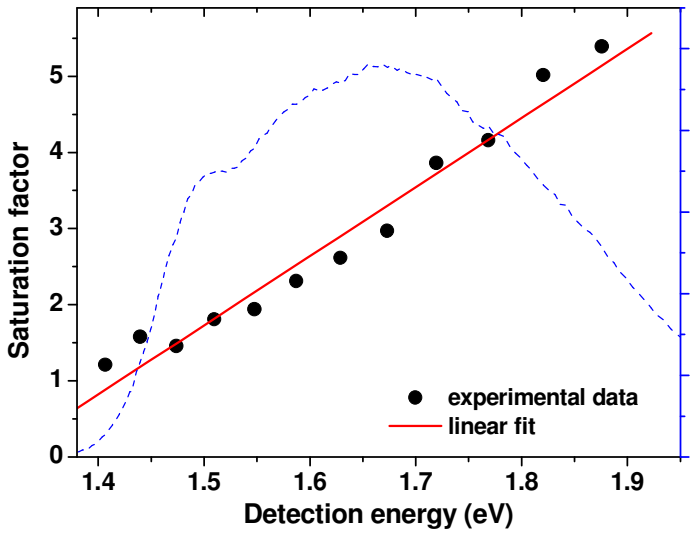

Figure 6-8 Saturation factor as a function of detection wavelength. The points are the saturation factor deduced from experiment and the solid line is a linear fit

dependence of the PL at various detection energies, as shown in figure 6-7, in which the points are the experimental data and the solid curves are the fits. We deduce the saturation factors as a function of detection photon energy, as shown in figure 6-8. The PL spectrum is also plotted as a reference. Considering the ratio $\tau_{cap}^{i} / \tau_{eff}^{i}$ (capture time / effective lifetime) which can be independent of or weakly dependent on the dot levels, we deduce a degeneracy of the energy level in the QD from the saturation factor $\alpha_i D_i / \alpha_0 D_0 \propto g_i / 2 = (i+1)$ with $i = 0$ for the ground level. As shown in figure 6-8 the saturation factors increase linearly with detection photon energy, which is consistent with the prediction of the rate equations. From the linear fit of the saturation factors, we can roughly estimate an energy level separation of 110 meV.

These experiments show that the silicon QD samples reveal a significant saturation effect even at fairly low excitation intensity. This is reasonable because the recombination rate is closely related to the state filling effect and a slow recombination rate will lead to a long lifetime in the states and thus significant filling. The radiative lifetime of electron-hole pairs localized in a silicon nanocrystal is very long, of the order of a microsecond. Therefore there is a large probability to excite a second electron-hole pair before the first one has recombined. In an indirect band gap material, such as silicon, phonon-assisted emission may make some contribution to the broad PL band although the quantum confinement effect results in an enhancement of the direct transition.

6-3-2 Time-resolved photoluminescence

In order to gain insight into the relaxation and recombination of carriers we performed time-resolved photoluminescence experiments. We adjusted the excitation intensity for the PL spectrum to be comparable to the high intensity spectra (e.g., 2 mW, 1 kHz in figure 6-5). This allowed investigation of the carrier relaxation dynamics between distinct QD levels starting with several fully occupied levels (the calculation suggests that more than 10 electron-hole pairs per dot can be generated). Figure 6-9 shows the time evolution of the PL spectrum detected at different wavelengths at room temperature. The rise time is very short, on the order of femtoseconds or picoseconds [18, 46-48], which is much shorter than the time resolution of the measurement system. As for the decay, each PL evolution consists of a very fast component and a slow component. The fast decay component cannot be resolved due to the low temporal resolution of the system and the slow component can be fit with a stretched

exponential function used to describe dispersive processes in a disordered system having a distribution of relaxation times, and is given by

$$I(t) = I_0 \exp[-(t/\tau)^{\beta}] \tag{6-3}$$

where τ is the PL lifetime and $0 \le \beta \le 1$ is the dispersion factor. Figure 6-10 shows the slow component of the PL evolution at the various detection wavelengths (points) and the corresponding stretched exponential function fit (solid lines). The lifetimes are listed in table 6-1 for the different detection wavelengths. As can be seen from the table, each of the lifetimes is on the order of microseconds and increases significantly with increasing detection wavelength. The dispersion factor, $\beta = 0.6$, is essentially independent of the detection wavelength, which suggests that this parameter is related to the macroscopic character of the medium, particularly its disorder characteristics, rather than the microscopic properties which depend on the size of the QDs [49]. Other groups have also experimentally observed or theoretically investigated the stretched exponential decay in silicon nanostructures and various models have been proposed to explain the stretched exponential decay; for instance, a hopping mechanism [50], and migration of excitons in an interconnected disordered network of

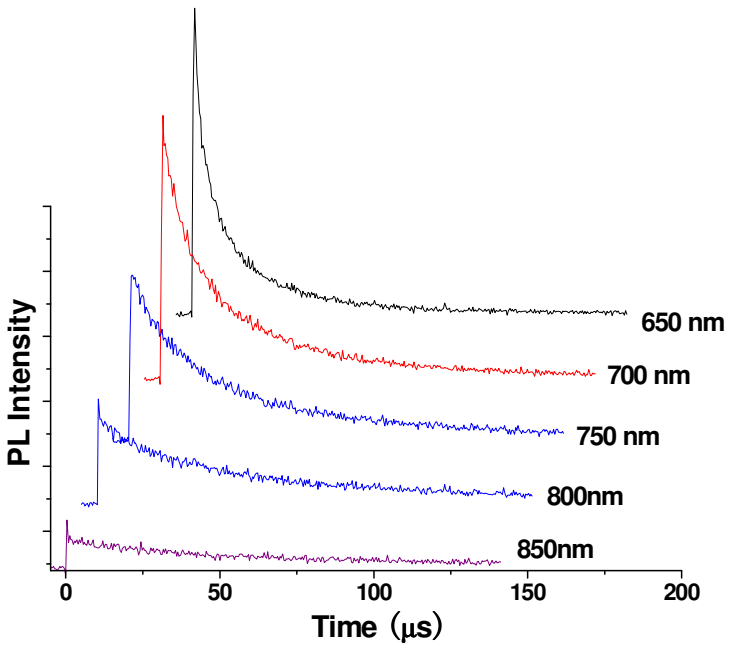

Figure 6-9 Time evolution of PL at different detection wavelengths as labelled

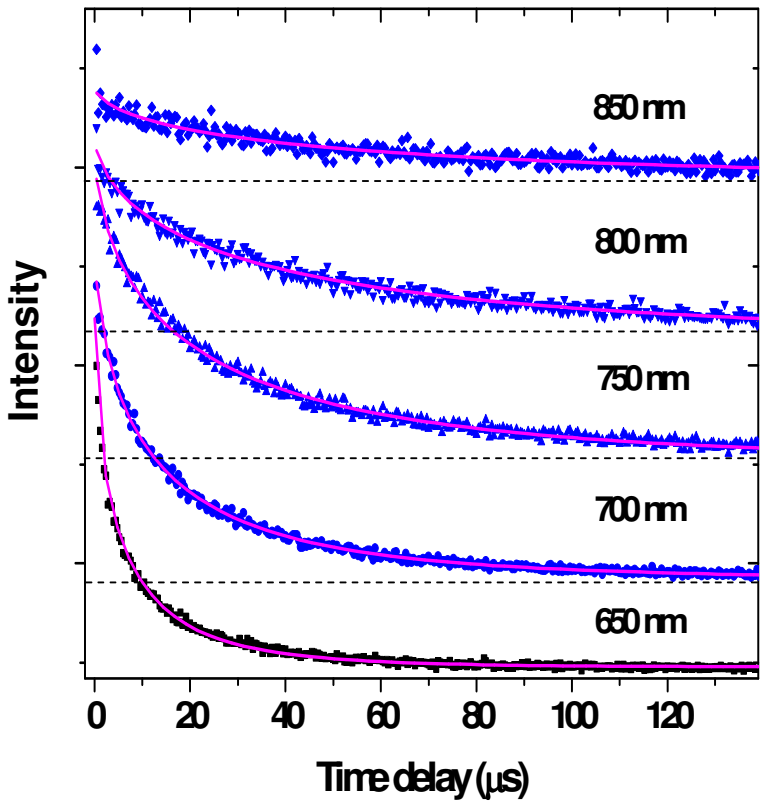

Figure 6-10 Evolution of the PL at various detection wavelengths (points) and fit with the stretched exponential function (solid line)

crystals [51, 52]. According to these models, a dispersive transport and distribution of trap and trap release rates are convolved with a non-exponential decay described by equation (6-3). This stretched exponential function is related to a distribution of relaxation times or a time-dependent relaxation rate, which reflects the interval reflection process in the QDs [49]. In time-resolved PL measurements, the lifetime of the high energy levels is significantly shorter than that of the low energy levels, similar to other observations [49, 53, 54].

Table 6-1 Lifetimes for different detection wavelengths with β=0.6

Detection λ (nm)	600	650	700	750	800	850
S92: τ (μs)	4.1 (±0.2)	7.0 (±0.2)	12.3 (±0.5)	20.1 (±0.5)	35 (±1)	50 (±2)

We measure the PL intensity on a short (nanosecond) time scale at different wavelengths and take the ratio of the intensity for each short wavelength (I_λ) to the maximum intensity at 850 nm (I_0), which is assumed to be approximately the luminescence from the ground level. The maximum of the PL intensity reflects the filling of the dot levels by photo-excited carriers and depends on the density of states of given dot levels. For short times after excitation, when the PL intensity is expected to reach a maximum, the influence of recombination and relaxation is very small and the dependence of the maximum PL intensity can be determined from rate equations with $\tau_R \gg \tau_C$ (recombination time and capture time, respectively). When the capture rate is independent of the dot energy level, we find the ratio $I_\lambda^{\max} / I_0^{\max} \sim g_i$, where $I_\lambda^{\max}$ and $I_0^{\max}$ are the maximum of the PL intensity at the detection wavelength and at 850 nm, respectively, and g_i is the degeneracy of the detected energy level. The degeneracy is close to $g_n = 2(n+1)$ [16], which suggests that a parabolic potential is a good approximation for these QD structures. From the intensity dependence of the PL spectrum we can explain the PL around 850-800 nm as due to transitions involving the dot ground level (n=0) which shifts to longer wavelength with large dot size. The PL at shorter wavelengths involves recombination of electrons and holes from high excited levels ($n \geq 1$). The energy splitting between the levels can be estimated from figure 6-11 (taken

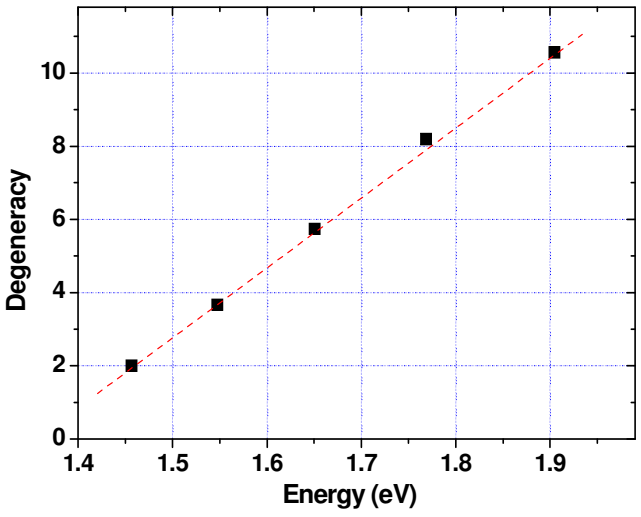

Figure 6-11 Dependence of the degeneracy on detection energy deduced from the evolution of the PL

with $g_i = 2, 4, 6, \cdots$) to be about 105 meV [16], which is consistent with that deduced from the time-integrated PL experiment (figure 6-8).

6-3-3 Temperature dependence

A temperature dependence of the PL spectra was performed at an excitation of 400 nm, as shown in figure 6-12. At 20 K, a similar broad S-band was observed ranging from 600 nm to 860 nm. With increasing temperature, the intensity of the S-band increases slightly and has a maximum at around 100-150 K (figure 6-13).

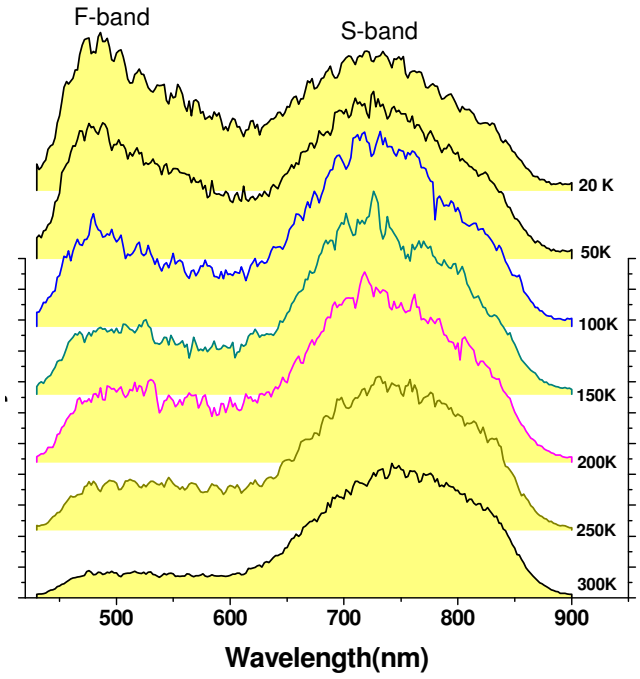

Figure 6-12 Temperature dependence of the PL spectra for an excitation wavelength of 400 nm. The S-band and F-band are clearly observed

The low temperature PL spectrum in the short wavelength region is quite different from that at room temperature. An obvious broad band can be observed ranging from 450 nm to 600 nm with a peak around 480 nm. The intensity of this band is comparable with that of the S-band. This band has been reported previously and is called an F-band because of its fast nanosecond decay time [55]. The F-band is likely to originate from defective silicon oxide since it was only observed in oxidized structures [55-58]. With increasing temperature, the

intensity of the F-band decreases gradually and becomes weak and flat at room temperature (figure 6-12). We measure the PL evolution at a wavelength 480 nm and temperature 20 K. The evolution is well fit by a single exponential decay and a decay time of 72 ns is deduced, which is much shorter than the decay time of the S-band.

The temperature dependence of the PL intensity is shown in figure 6-13 for various detection wavelengths. In the S-band the short wavelengths exhibit different temperature dependence to that of the long wavelengths. In the low temperature regime various wavelengths of the S-band exhibit a similar increase with increasing temperature from 20 K to 150 K except for a slight decrease at 650 nm. With further increase of temperature from 200 K to 293 k the intensity of the short wavelengths decreases more than that of the long

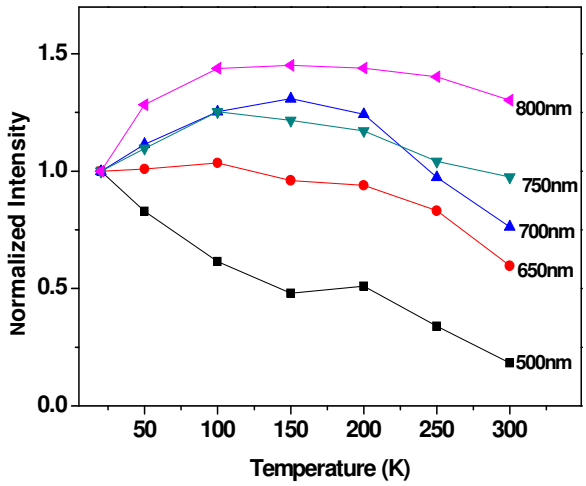

Figure 6-13 PL intensity as a function of temperature at different detection wavelengths.

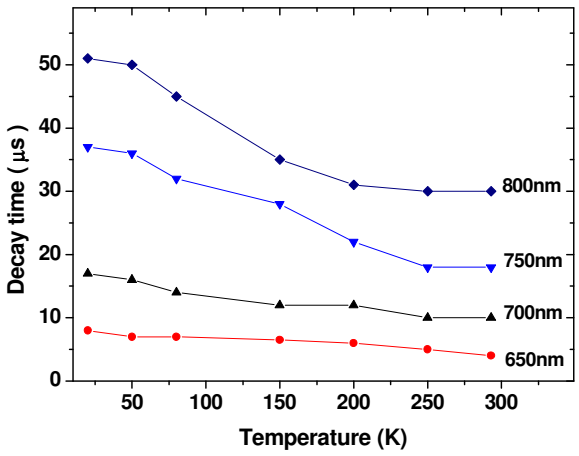

Figure 6-14 Decay time as a function of temperature for various detection wavelengths

wavelengths. Thus a red shift of about 30 nm is observed with increasing temperature from 150 K to 293 K. For a given wavelength the intensity at room temperature is similar to that at 20 K, i.e., the PL intensity varies by no more than 30% for a temperature increase from 20 K to room temperature and it increases at long wavelengths and decreases at short wavelengths.

We compare the decay times of the S-band at various temperatures and detection wavelengths in figure 6-14. At a given temperature, the short wavelengths give a smaller decay time, similar to that at room temperature. For each given detection photon energy, the decay time decreases monotonically with increasing temperature. The decay time decreases by approximately half when the temperature changes from 20 K to 293 K.

6-3-4 Discussion

Compared to bulk silicon, the optical properties of silicon QDs change significantly due to quantum confinement. With decreasing size, both the absorbing and luminescent states shift to higher energies and the density of electronic states is affected due to the increase of the minimum kinetic energy. At the same time, spatial confinement leads to delocalization of the carriers in k-space and the overlapping of the wave-functions of the electrons and holes increases. Thus zero-phonon direct optical transitions are partially allowed and the oscillator strength of direct optical transitions is significantly enhanced. The excitation dependence experiment shows that the PL intensity at short wavelengths decreases significantly with decreasing excitation intensity, which is likely to be a state filling effect. This suggests that this band originates mainly from the direct no-phonon transition of localized electron-hole recombination. However, even at low excitation the bandwidth is still very broad, which implies a fairly strong inhomogeneous broadening.

Furthermore, because of the size confinement effect in silicon QDs, two kinds of different PL mechanisms - zero-phonon transitions and phonon-assisted transitions - are possible. For a direct transition, the detection energy directly reflects the band gap with $E_{Det} = E_{Gap}$. For a phonon-assisted transition, $E_{Det} = E_{Gap} - E_{Phonon}$. Therefore, for a given detected wavelength, the PL may originate from two types of QDs with different dot size and thus different confinement energy (band gap). In other words, the PL of the silicon QDs is based on a competition between indirect (phonon-assisted) and direct (zero-phonon) recombination channels. In the strong confinement regime (small dot size and short wavelength) zero-phonon transitions may be dominant and phonon-assisted transitions hardly

play a role. In the very weak confinement regime, the strength of phonon-assisted transitions increases. Therefore, phonon-assisted transitions may contribute to some extent to the broad S-band. The saturation factor distribution (figure 6-8) based on the state filling effect shows a good linear dependence and is consistent with the rate equation prediction, which may suggest that phonon-assisted transitions have only a negative contribution and the quantum confinement effect is fairly strong.

The intensity of the PL is determined by two factors. One is the number of carriers captured into QDs and the other is the PL quantum yield, which is given by

$$\eta_{PL} = \frac{1/\tau_R}{1/\tau_R + 1/\tau_{NR}} = \frac{\tau}{\tau_R} \tag{6-4}$$

where τ_R and τ_{NR} are the radiative and the nonradiative decay times, respectively, and the total PL decay time in the measurement can be expressed as $1/\tau = 1/\tau_R + 1/\tau_{NR}$. The long decay time and high emission efficiency at room temperature in silicon QDs is not due to a reduction in the radiative decay rate, because the strength of the radiative transitions in the silicon QDs is significantly weaker than that of direct gap semiconductors, but rather it is due to a strong suppression of nonradiative processes [49, 59]. The increase in the nonradiative lifetime is likely to be due to a number of effects, for instance, a reduction of the surface recombination centres per unit area and the small cross section of the dots ensures that the density of nonradiative centres is very small. The nonradiative lifetime may be as long as milliseconds in nanocrystal or porous silicon [59].

The decay time varies with the detection wavelengths because various detection wavelengths correspond to different states of the silicon QDs. In general, radiative lifetimes are inversely proportional to $E^2 f_{osc}$, where f_{osc} is the optical transition oscillator strength and $E = \hbar\omega$ is the emitted photon energy [60]. A small detection wavelength corresponds to a high excited level of the quantum dots and a large emission energy, and thus it will result in a shorter radiative lifetime. Furthermore, a short detection wavelength corresponds to a small size of the QDs due to the strong inhomogeneous broadening in the silicon QDs. The small dot size leads to a strong quantum confinement, and thus results in a large optical transition oscillator strength due to the large overlap of the wave functions. Therefore, a shorter detection wavelength not only means a higher excited level but also a stronger optical transition strength, so that a short decay time can be expected [49].

The temperature behaviour of the PL can be divided into two regimes, the low temperature regime from 20 K to 150 K and the high temperature regime from 200 K to 300 K. At low temperature a large number of the photoexcited carriers are localized by the defect states because of various defect states in the silicon and silicon oxide [59], and thus a strong and broad F-band is observed in the PL from these states. With increasing temperature, the carriers in these states are gradually thermally delocalized and relax into the lower states, mainly the states of the silicon QDs, which results in an increase of the PL intensity in the S-band and a decrease in the F-band. In the low temperature regime, the process of carriers thermally delocalizing from the defect states and being captured into the states of the QDs plays a dominant role and thus carriers captured into the QDs increases with increasing temperature. Therefore, the PL intensity increases for the S-band and decreases for the F-band with increasing temperature. With further increasing temperature, nonradiative recombination for the defect states is significantly enhanced and more photoexcited carriers are captured into these defect states. Thus the carriers captured into the QDs decrease due to the carrier capture competition. Therefore the intensity of the S-band decreases. At the same time the PL quantum yield of the F-band decreases because the nonradiative recombination increases, which results in a decrease in the intensity of the F-band.

Another effect, the state filling effect, may play an important role in this process. In this effect the carriers in higher states cannot relax into lower states until there is a vacancy available in the lower states due to the Pauli exclusion[5,10]. Due to the extremely slow interband recombination rate the intersublevel relaxation in the QDs should be much faster than interband recombination, which will result in a strong state filling effect [5]. With increasing temperature the lifetimes of the QD states decrease, which will increase the availability in these lower states and thus more carriers can relax into the lower states. Hence the PL intensity of the low states increases. In the low temperature regime, the process of carriers delocalizing from the defect states and being captured into the states of the QDs is dominant and thus the carriers for most of the QD states increase though the state filling effect leads to more carriers into the lower states. Therefore the PL intensity for most QD states increases except for a slight decrease of the intensity for the highest states. At this stage we cannot observe a red shift because the PL intensities at low and high energy increase. In the high temperature regime carriers captured into the QDs decrease with temperature and the state filling effect plays an important role, which results in a decrease of the intensity for the high states of the QDs, corresponding to wavelengths of 650 nm and 700 nm, but a moderate decrease for the lower states of the QDs, such as 750 nm and 800 nm. Thus a 30 nm red shift is observed over the temperature range 150 K to room temperature.

6-4 Transient grating experiment

Nonlinear coherent spectroscopy has been shown to provide femtosecond time resolution and valuable information about the coherence properties and dynamics of carriers in quantum structures, which are important for the fabrication of many optoelectronic devices [19, 61-63]. Coherence properties are a very important and interesting subject in silicon quantum dots and porous silicon because of the close relationship with further applications and fundamental understanding. However, there are few reports in this field, and the ultrafast dynamics and the dephasing parameters are still relatively unknown [17, 21]. The main difficulties of coherent spectroscopy in semiconductor quantum dots are the extremely low nonlinear signal intensity and the dispersion of the dot size. Various coherent spectroscopy techniques have been considered for the study of the coherent properties and measurement of the dephasing and ultrafast relaxation in semiconductor quantum dots [62, 64, 65], such as four-wave mixing [17, 61], pump-probe spectroscopy [66], time-resolved photoluminescence [17, 18] and photon echoes [67, 68].

In this study a special case of the photon echoes experiment in which $t_{12} = 0$, i.e. a transient grating experiment, was performed to study ultrafast dynamics of the carriers in order to obtain quantitative information about the ultrafast relaxation. The experiment was performed in the setup of the three pulse photon echoes as described in detail in chapter 2. In this experiment the coherence time (time separation between pulses $\mathbf{k_1}$ and $\mathbf{k_2}$) was fixed at $t_{12} = 0$. When the two pump pulses $\mathbf{k_1}$ and $\mathbf{k_2}$ overlap temporally a transient population grating with wave vector $\mathbf{k_2}$-$\mathbf{k_1}$ is created. The probe pulse is diffracted by this grating in the phase-matched directions and detected as the observed signal. The lifetime of the population grating is related to the lifetime and diffusion time of the excited carriers. By studying the relaxation dynamics in this way, the excited states are probed directly, rather than in time-resolved photoluminescence which relies on the radiative emission of the excited carriers. Transient grating experiments are particularly interesting in indirect band edge silicon QD systems where there is a combination of phonon-assisted and zero-phonon transitions.

In the experiment, the pump pulses $\mathbf{k}_1$ and $\mathbf{k}_2$ with the same wavelength 600 nm and different direction are spatially and temporally overlapped in the sample, creating a population grating. The third pulse $\mathbf{k}_3$, spatially overlapped with the first two pulses but time-delayed, is

then diffracted off this grating in the phase-matched direction $\mathbf{k_4 = k_1 - k_2 + k_3}$ with a signal intensity that decays with the population time t_{23} (time separation between pulses $\mathbf{k_2}$ and $\mathbf{k_3}$) [19, 20]. Figure 6-15 shows the time evolution of the integrated signal intensity versus population time t_{23} with a fixed coherent time $t_{12} = 0$. The third pulse $\mathbf{k}_3$ is tuned to 640 nm (a), 670 nm (b), 700 nm (c) and 740 nm (d). For each given probe wavelength a very fast rise time is observed, which suggests a very effective relaxation, most likely dominated by phonon-assisted transitions. Following the fast rise, a relatively slow decay of the signal is observed. The integrated intensity can be fit with a three-exponential decay function $A_1 \exp(-t/T_1) + A_2 \exp(-t/T_2) + A_3 \exp(-t/T_3)$, where the three time constants $T_3 > T_2 > T_1$. For this silicon QD system, the three time constants correspond to a fast decay time, a slow decay time and a very long electron-hole pair recombination time, respectively. The recombination time is very long, on the order of microseconds, and thus its contribution on the time scale studied is simply as an offset. Indeed, an obvious offset can be observed in each transient grating signal at the various probe wavelengths, which implies the presence of a

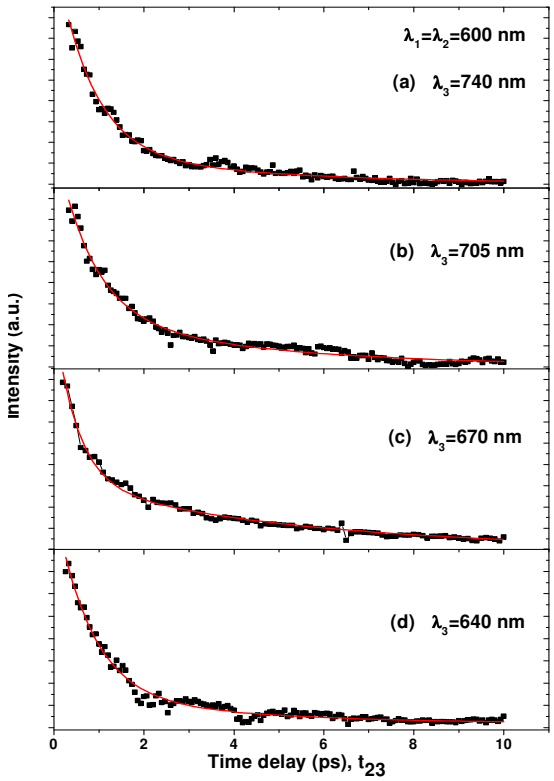

Figure 6-15 Time evolution of the signal intensity at the peak of the probe pulse versus population time t_{23} for fixed t_{12}=0 and different combinations of laser wavelengths

slow decay component. From the fitting, we deduce fast and slow decay times with 800 fs and 4 ps for each detection wavelength. However, the amplitude ratio A_1 / A_2, which represents the relative contribution from the fast and the slow components, varies for the different detected wavelengths. At the probe wavelength 640 nm, a relatively large ratio $A_1 / A_2 = 7$ is deduced, whilst for other wavelengths an amplitude ratio $A_1 / A_2 = 3 \sim 4$ is found.

In indirect semiconductors, such as bulk Si, the phonons play a very important role in optical transitions. The most efficient contribution to the PL is the TO phonon-assisted recombination process, with the TA phonon-assisted process about 10 times weaker than the TO phonon-assisted process [63]. In bulk silicon, direct optical transitions are forbidden. However, due to quantum confinement, the zero-phonon optical transition is significantly enhanced due to the larger overlap of the electron and the hole envelope wavefunctions in silicon QDs. The long decay, on the microsecond scale, is attributed to radiative recombination of electron and hole pairs. On the short time scale, TO and TA momentum conserving phonon-assisted transitions are dominant. Compared with TA phonon-assisted transitions, TO phonon-assisted transitions have a much stronger strength and thus a faster decay rate [63, 69].

Recently, Trojanek *et al*. observed ultrafast decay in silicon nanocrystals using the femtosecond up-conversion technique and interpreted the fast decay components due to

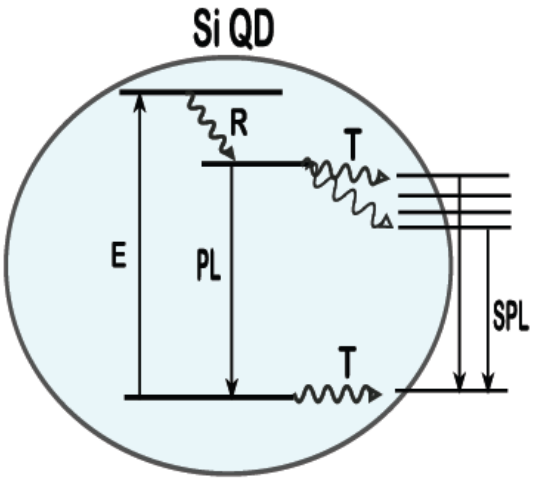

Figure 6-17 Scheme for relaxation and recombination channels in Si QDs. E-excitation, R-relaxation, PL-radiative recombination of interior exciton, T-carrier trapping to the surface state, SPL-recombination of the surface trapped carriers

radiative recombination of interior electrons and holes in the nanocrystal before excited electrons localize at the nanocrystal surface or interface states [18].

Following Trojanek's model [18], we attribute the fast and slow decay components to TO and TA phonon-assisted transitions, respectively, as illustrated schematically in figure 6-17. After laser excitation, photoexcited carriers relax into an interior excited state in the silicon QDs. This relaxation is expected to be very fast with only 30~40 fs for our excitation conditions because of the extremely fast relaxation rate 3.8 eV/ps in silicon nanocrystals [18]. The carriers in the interior excited state will be trapped on the QDs' surface or interface states with phonon-assisted transitions [70], which lead to a fast decay in the transient grating signal. In these relaxation channels TO phonon-assisted transitions contribute to the fast component and TA or various multi-phonon-assisted transitions (TO+nTA with n an integer) give the slow component because the TA phonon-assisted transitions have a much weaker strength and thus a slower relaxation rate. It is worth noting that $E_{TO} \approx 3E_{TA} = 56\,meV$. In this case, TO phonon-assisted transitions give a dominant contribution if the energy separation matches the TO energy very well. However, it is relatively easy to match the relaxation energy for TA phonons because of the smaller phonon energy. Therefore, TA phonon-assisted transitions can give a larger contribution when the energy separation is mismatched to the TO energy. For the short detection wavelength, 640 nm, it is likely that the energy separation matches the TO energy well. Therefore, the TO phonon-assisted trap is dominant and a larger A_1 / A_2 can be obtained. For the other probe wavelengths, however, the relaxation energy does not match the TO energy well, so that TA phonon-assisted relaxation has an increased contribution and thus a relatively small amplitude ratio is observed. Because of the strong inhomogeneous broadening and the large relaxation energy (100~300 meV), together with the strong TO phonon-assisted transitions, the TO phonon-assisted transitions are dominant for each of the detection wavelengths. The surface trapping, leading to a separation of electrons and holes, thus effectively quenches the photoluminescence and contributes an ultrafast component. At the same time, it is this separation that also results in a much slower carrier recombination on the time scale of microseconds.

6-5 Conclusions

We have investigated the optical properties of silicon quantum dots using time integrated photoluminescence, time-resolved photoluminescence and photon echo spectroscopies. A broad band was observed at 600-900 nm which originates mainly from recombination of electrons and holes due to the quantum confinement effect. A significant state filling effect was observed in an excitation dependent experiment, which suggests that the emission of the broad S-band originates from various levels of silicon quantum dots. Time-resolved photoluminescence experiments confirm that the S-band has a stretched exponential decay with lifetimes on the order of microseconds. In this band, the lifetimes of the short wavelengths are significantly shorter than those of the long wavelengths. Another band is observed at low temperatures whose centre is located at around 480 nm. This F-band is likely to originate from defective silicon oxide. In the low temperature regime (20-150 K) with increasing temperature the process of carriers delocalizing from the defect states and being captured into the QDs is the dominant mechanism, which results in an intensity increase in the S-band and a decrease in the F-band. In the high temperature regime (200-300 K), the carriers captured into the QDs decrease due to competition of the capturing into the defect states, which results in a intensity decrease both in the S-band and the F-band. Within the S-band the PL intensities of the shorter wavelengths decrease more slowly due to the state filling effect, which results in a red shift of the S-band.

A fast decay is observed in the transient grating experiment that includes a fast and a slow component with time constants of 800 fs and 4 ps. These components are attributed to TO and TA phonon-assisted trapping into surface states or interface states of the QDs. The separation of the electrons and holes results in a very small recombination rate.

Chapter 7

Summary and Recommendations for Further Work

In this thesis, ultrafast spectroscopy has been applied to study the characteristics of semiconductor nanostructures, especially the ultrafast dynamics of energy relaxation, which is one of the most important areas for the understanding, improvement and further application of these novel materials. By applying various ultrafast spectroscopy techniques and conventional photoluminescence, we have investigated dynamical phenomena in ZnO/ZnMgO multiple quantum wells, InGaAs/GaAs p-doped self-assembled quantum dots, InGaAs/InP proton implantation-induced intermixing and silicon quantum dots embedded in a SiO_2 matrix.

During the last decade, ZnO has attracted special attention due to the attractive properties of its various nanostructures. In particular, ZnO is regarded as a potential UV laser material. We have observed clear evidence of biexcitons in ZnO/ZnMgO multiple quantum wells (MQWs) at room temperature, and have measured the dephasing times of biexcitons and excitons. To our knowledge, this is the first observation of biexcitons in ZnO at room temperature. The decay times of the MQW samples were measured by the pump-probe technique at room temperature. In the high photon energy region a very short decay time (a few hundreds femtoseconds) confirms an effective phonon relaxation for the hot carriers, whilst in the exciton region a tens of picoseconds decay time originates mainly from exciton recombination, which is consistent with previous investigations. An interesting implantation effect was observed in these MQW samples. With a suitable dose of oxygen ion implantation, the MQW sample can achieve not only a tuning of the QW emission over 10-20 nm but also an improvement of the properties, such as a significant improvement of the temperature quenching of the PL and a small increase of the luminescence quantum efficiency. This is very different from the implantation effect in other materials reported in which tuning the wavelength results in a decrease in quantum efficiency.

InGaAs is an important material because it can cover the near infrared wavelength range for the optical communications and optical information industry. The slow relaxation in the quantum dots can be a barrier for a high repetition rate laser and ultrafast data transfer and communication. Modulation doping is predicted as a potential technique to overcome the

barrier and achieve high quantum efficiency and high modulation rates. We observe a fast relaxation rate in a modulation doped InGaAs sample at low temperature compared with a similar undoped sample, suggesting that electron-hole scattering is the dominant relaxation mechanism. At high excitation intensity, a significant state filling effect is observed. Ion implantation is known to be an effective post-growth technique to tune the emission wavelength in semiconductors. Implantation in InGaAs quantum wells results in a variation in the carrier capture and energy relaxation. We have investigated the variation of the optical properties by ion implantation and the effect of different strains in the interface between the quantum well and the barrier.

Silicon is the most commonly used semiconductor material. Silicon quantum dots and porous silicon are very interesting materials because they can achieve a relatively high luminescence efficiency even at room temperature in this indirect band gap material. At the same time, silicon is a very complicated material because of various luminescence mechanisms, various defects or localized states in the silicon and silicon oxide (matrix) and very strong inhomogeneous broadening. Thus different mechanisms have been proposed in silicon nanostructures. Using direct measurements on a microsecond time scale and femtosecond photon echo techniques, we have investigated the dynamics on the different time scales, in the femtosecond and microsecond regions. In the ultrafast photon echoes, we detected a very short decay time (a few hundred femtoseconds to a few picoseconds), which corresponds to transverse optical and transverse acoustic phonon-assisted relaxation. Through these ultrafast relaxation processes, hot electrons and holes are captured into localized states where they recombine and emit effectively, and exhibit a microsecond lifetime. A stretched exponential function decay was observed in a silicon QD sample that originates mainly from recombination of electrons and holes. A state filling effect was also observed in the silicon QD sample, which is quite different from the case of InGaAs QDs due to very strong inhomogeneous broadening.

However, we are still quite limited in acquiring comprehensive and detailed information from ultrafast spectroscopy, mainly due to the range of laser excitation wavelengths and intensities, the detection sensitivity at a given wavelength, and the low quantum efficiency in the materials. Various ZnO nanostructures have shown many interesting properties and an understanding of their coherence properties is still at an early stage. To explore the coherence properties comprehensively and to develop further new applications, ultrafast spectroscopy and especially ultrafast coherence spectroscopy can play a major role. It has been shown that ZnO quantum wells reveal an interesting improvement through oxygen irradiation induced implantation. However, it is still unclear which kind of

defects plays a dominant role and how they are affected by the implantation. In InGaAs QDs, the details of the relaxation mechanisms are not clear and some of the experimental observations are not consistent with each other. A comprehensive understanding of the ultrafast dynamical processes is the key to achieving higher relaxation rates and high performance QD lasers. Ion implantation has been demonstrated as an effective post-growth technique to tune the emission wavelength. The strain between the quantum well and the barrier is still a problem. How the various strains exactly affect the shape of the potential of the quantum well and the interface is a further subject of research. There have been a large number of papers reporting the properties of silicon nanocrystals and porous silicon, and various different mechanisms have been proposed as being responsible for the emission from silicon nanostructures, and its coherence properties are still at the initial stage. The great potential applications warrant a thorough investigation and a deep understanding in silicon nanostructures. With the progress of lasers and detection techniques, ultrafast spectroscopy will certainly play an increasingly important role as a powerful versatile tool, and will make further contributions to the progress of semiconductor nanostructures.

Bibliography

Chapter 1

[1] T. Steiner, *Semiconductor Nanostructures for Optoelectronic Applications*. Norwood: Artech House Inc., 2004.

[2] O. Manasreh, *Semiconductor Heterojunctions and Nanostructures*. New York: McGraw Hill, 2005.

[3] N. Zurauskiene, S. S. Asmontas, A. Dargys, J. Kundrotas, G. Janssen, E. Goovaerts, S. Marcinkevicius, P. M. Koenraad, J. H. Wolter, and R. Leon, "Semiconductor nanostructures for infrared applications," in *Functional Nanomaterials for Optoelectronics and Other Applications*, vol. 99-100, *Solid State Phenomena*, 2003, pp. 99-108.

[4] V. N. Lutskii, "Quantum size effect-present state and perspectives of experimental investigations," *Physica Status Solidi A*, vol. 1, pp. 199-200, 1970.

[5] L. Esaki and R. Tsu, "Superlattice and negative differential conductivity in semiconductors," *IBM Journal of Research and Development*, vol. 14, pp. 61-65, 1970.

[6] R. F. KaZarinov and R. A. Suris, "Possibility of amplification of electromagnetic waves in a semiconductor with a superlattice," *Soviet Physics Semiconductor*, vol. 5, pp. 797-800, 1971.

[7] J. Faist, F. Capasso, D. L. Sivco, A. L. Hutchinson, C. Sirori, S. N. G. Chu, and A. Y. Cho, "Quantum cascade laser: temperature dependence of the performance characteristics and high To operation," *Applied Physics Letters*, vol. 65, pp. 2901-2903, 1994.

[8] E. Bockenhoff and H. Benisty, "Evolution of 3d Growth-Patterns on Nonplanar Substrates," *Journal of Crystal Growth*, vol. 114, pp. 619-632, 1991.

[9] T. C. Hasenberg, P. S. Day, E. M. Shaw, D. J. Magarreli, J. T. Olesberg, C. Yu, T. F. Boggess, and M. E. Flatte, "Molecular beam epitaxy growth and characterization of broken-gap (type II) superlattices and quantum wells for midwave-infrared laser diodes," *Journal of Vacuum Science & Technology B*, vol. 18, pp. 1623-1627, 2000.

[10] M. Geiger, A. Bauknecht, F. Adler, H. Schweizer, and F. Scholz, "Observation of the 2D-3D growth mode transition in the InAs/GaAs system," *Journal of Crystal Growth*, vol. 170, pp. 558-562, 1997.

[11] M. Grundmann and D. Bimberg, "Formation of quantum dots in twofold cleaved edge overgrowth," *Physical Review B*, vol. 55, pp. 4054-4056, 1997.

[12] F. Heinrichsdorff, A. Krost, M. Grundmann, D. Bimberg, F. Bertram, J. Christen, A. Kosogov, and P. Werner, "Self organization phenomena of InGaAs/GaAs quantum dots grown by metalorganic chemical vapour deposition," *Journal of Crystal Growth*, vol. 170, pp. 568-573, 1997.

[13] T. R. Ramachandran, A. Madhukar, I. Mukhametzhanov, R. Heitz, A. Kalburge, Q. Xie, and P. Chen, "Nature of Stranski-Krastanow growth of InAs on GaAs(001)," *Journal of Vacuum Science & Technology B*, vol. 16, pp. 1330-1333, 1998.

[14] W. W. R. Dingle, H. Henry, "Quantum states of confined carriers in very thin $Al_xGa_{1-x}As/GaAs/Al_xGa_{1-x}As$ heterostructures," *Physical Review Letters*, vol. 33, pp. 827,

1974.

[15] X. Q. Liu, N. Li, W. Lu, X. Z. Yuan, S. C. Shen, L. Fu, H. H. Tan, and C. Jagadish, "Wavelength tuning of GaAs/AlGaAs quantum-well infrared photo-detectors by proton implantation induced intermixing," *Japanese Journal of Applied Physics Part 1-Regular Papers Short Notes & Review Papers*, vol. 39, pp. 1687-1689, 2000.

[16] P. W. M. Blom, C. Smit, J. E. M. Haverkort, and J. H. Wolter, "Carrier Capture into a Semiconductor Quantum-Well," *Physical Review B*, vol. 47, pp. 2072-2081, 1993.

[17] G. Bacher, C. Hartmann, H. Schweizer, T. Held, G. Mahler, and H. Nickel, "Exciton Dynamics in $In_xGa_{1-X}As$/GaAs Quantum-Well Heterostructures - Competition between Capture and Thermal Emission," *Physical Review B*, vol. 47, pp. 9545-9555, 1993.

[18] R. Heitz, O. Stier, I. Mukhametzhanov, A. Madhukar, and D. Bimberg, "Quantum size effect in self-organized InAs/GaAs quantum dots," *Physical Review B*, vol. 62, pp. 11017-11028, 2000.

[19] K. Brunner, U. Bockelmann, G. Abstreiter, M. Walther, G. Bohm, G. Trankle, and G. Weimann, "Photoluminescence from a Single GaAs/AlGaAs Quantum Dot," *Physical Review Letters*, vol. 69, pp. 3216-3219, 1992.

[20] U. Bockelmann, W. Heller, A. Filoramo, and P. Roussignol, "Microphotoluminescence studies of single quantum dots. 1. Time-resolved experiments," *Physical Review B*, vol. 55, pp. 4456-4468, 1997.

[21] W. Demtröder, *Laser Spectroscopy*. Berlin: Springer-Verlag, 1998.

[22] L. V. Dao, C. N. Lincoln, R. M. Lowe, M. T. T. Do, P. Eckle, and P. Hannaford, "Spectrally resolved two-colour femtosecond photon echoes: A new multidimensional technique for studying molecular dynamics," *Laser Physics*, vol. 15, pp. 1257-1268, 2005.

[23] L. Van Dao, C. Lincoln, M. Lowe, and P. Hannaford, "Spectrally resolved femtosecond two-colour three-pulse photon echoes: Study of ground and excited state dynamics in molecules," *Journal of Chemical Physics*, vol. 120, pp. 8434-8442, 2004.

[24] L. Van Dao, M. Lowe, P. Hannaford, H. Makino, T. Takai, and T. Yao, "Femtosecond three-pulse photon echo and population grating studies of the optical properties of CdTe/ZnSe quantum dots," *Applied Physics Letters*, vol. 81, pp. 1806-1808, 2002.

[25] R. Heitz, M. Veit, N. N. Ledentsov, A. Hoffmann, D. Bimberg, V. M. Ustinov, P. S. Kopev, and Z. I. Alferov, "Energy relaxation by multiphonon processes in InAs/GaAs quantum dots," *Physical Review B*, vol. 56, pp. 10435-10445, 1997.

[26] L. V. Dao, M. Gal, C. Carmody, H. H. Tan, and C. Jagadish, "A comparison of impurity-free and ion-implantation-induced intermixing of InGaAs/InP quantum wells," *Journal of Applied Physics*, vol. 88, pp. 5252-5254, 2000.

[27] P. Borri, W. Langbein, S. Schneider, U. Woggon, R. L. Sellin, D. Ouyang, and D. Bimberg, "Exciton relaxation and dephasing in quantum-dot amplifiers from room to cryogenic temperature," *IEEE Journal of Selected Topics in Quantum Electronics*, vol. 8, pp. 984-991, 2002.

[28] L. V. Dao, C. Lincoln, M. Lowe, and P. Hannaford, "Spectrally Resolved Two-Colour Femtosecond Photon Echoes," in *Femtosecond Laser Spectroscopy* P. Hannaford, Ed. New York: Springer, 2005, pp. 197-224.

[29] L. Van Dao and P. Hannaford, "Femtosecond nonlinear coherence spectroscopy of carrier dynamics in porous silicon," *Journal of Applied Physics*, vol. 98, 2005.

[30] J. Shah, *Ultrafast Spectroscopy of Semiconductors and Semiconductor Nanostructures*. Berlin: Springer-Verlag, 1999.

[31] L. E. Vorobjev, A. V. Glukhovskoy, S. N. Danilov, V. Y. Panevin, D. A. Firsov, N. K. Fedosov, V. A. Shalygin, A. D. Andreev, B. V. Volovik, N. N. Ledentsov, D. A. Livshits, V. M. Ustinov, A. F. Tsatsul'nikov, Y. M. Shernyakov, M. Grundmann, A. Weber, F. Fossard, and F. H. Julien, "Nonequilibrium spectroscopy of inter-and intraband transitions in quantum dot structures," in *Ultrafast Phenomena in Semiconductors 2001*, vol. 384-3, *Materials Science Forum*, 2002, pp. 39-42.

[32] T. Muller, F. F. Schrey, G. Strasser, and K. Unterrainer, "Ultrafast intraband spectroscopy of electron capture and relaxation in InAs/GaAs quantum dots," *Applied Physics Letters*, vol. 83, pp. 3572-3574, 2003.

[33] F. Eickemeyer, K. Reimann, M. Woerner, T. Elsaesser, S. Barbieri, C. Sirtori, G. Strasser, T. Muller, R. Bratschitsch, and K. Unterrainer, "Ultrafast coherent electron transport in semiconductor quantum cascade structures," *Physical Review Letters*, vol. 89, 2002.

[34] K. Gundogdu, K. C. Hall, T. F. Boggess, D. G. Deppe, and O. B. Shchekin, "Ultrafast electron capture into p-modulation-doped quantum dots," *Applied Physics Letters*, vol. 85, pp. 4570-4572, 2004.

[35] U. Bockelmann, "Phonon-Scattering between Zero-Dimensional Electronic States - Spatial Versus Landau Quantization," *Physical Review B*, vol. 50, pp. 17271-17279, 1994.

[36] T. R. Nielsen, P. Gartner, M. Lorke, J. Seebeck, and F. Jahnke, "Coulomb scattering in nitride-based self-assembled quantum dot systems," *Physical Review B*, vol. 72, 2005.

[37] T. Inoshita and H. Sakaki, "Electron-phonon interaction and the so-called phonon bottleneck effect in semiconductor quantum dots," *Physica B*, vol. 227, pp. 373-377, 1996.

[38] T. Inoshita and H. Sakaki, "Electron Relaxation in a Quantum Dot - Significance of Multiphonon Processes," *Physical Review B*, vol. 46, pp. 7260-7263, 1992.

[39] R. Heitz, A. Schliwa, and D. Bimberg, "Exciton-LO-phonon coupling in self-organized InAs/GaAs quantum dots," *Physica Status Solidi B-Basic Research*, vol. 237, pp. 308-319, 2003.

[40] C. Amman, M. A. Dupertuis, U. Bockelmann, and B. Deveaud, "Electron relaxation by LO phonons in quantum wires: An adiabatic approach," *Physical Review B*, vol. 55, pp. 2420-2428, 1997.

[41] U. Bockelmann, "Exciton Relaxation and Radiative Recombination in Semiconductor Quantum Dots," *Physical Review B*, vol. 48, pp. 17637-17640, 1993.

Chapter 2

[1] F. Dausinger, F. Lichtner, and H. Lubatschowski, "Femtosecond technology for technical and medical application," in *Topics in Applied Physics*. vol. 96 Berlin: Springer-Verlag, 2004.

[2] M. E. Fermann, A. Galvanauskas, and G. Sucha, "Ultrafast Lasers-Technology and Application," New York: Marcel Dekker, 2003.

[3] P. M. W. French, "The Generation of Ultrashort Laser-Pulses," *Reports on Progress in Physics,* vol. 58, pp. 169-262, Feb 1995.

[4] F. Eickemeyer, K. Reimann, M. Woerner, T. Elsaesser, S. Barbieri, C. Sirtori, G. Strasser, T. Muller, R. Bratschitsch, and K. Unterrainer, "Ultrafast coherent electron transport in semiconductor quantum cascade structures," *Physical Review Letters,* vol. 89, 047402, Jul 2002.

[5] L. V. Dao, C. Lincoln, M. Lowe, and P. Hannaford, "Spectrally Resolved Two-Colour Femtosecond Photon Echoes," in *Femtosecond Laser Spectroscopy* P. Hannaford, Ed. New York: Springer, 2005, pp. 197-224.

[6] L. Allen and J. H. Eberly, *Optical Resonance and Two-Level Atoms*. New York: Interscience, 1975.

[7] Y. R. Shen, *The Principles of Nonlinear Optics*. New York: Wiley, 1984.

[8] J. Shah, *Ultrafast Spectroscopy of Semiconductors and Semiconductor Nanostructures*: Springer, 1999.

[9] H. Haug and S. W. Koch, *Quantum Theory of the Optical and Electronic Properties of Semiconductors*. Singapore: World Scienftific, 1993.

[10] J. Shah, "Ultrafast luminescence spectroscopy using sum frequency generation," *IEEE Journal of Quantum Electronics,* vol. 24, pp. 276-288, 1988.

[11] S. Mukamel, "Multidimensional femtosecond correlation spectroscopies of electronic and vibrational excitations," *Annual Reviews of Physical Chemistry,* vol. 51, pp. 691-729, 2000.

[12] L. Van Dao, M. Lowe, and P. Hannaford, "Femtosecond nonlinear spectroscopy investigation of the yellow band of GaN," *Journal of Physics B:Atomic Molecular and Optical Physics,* vol. 36, pp. 1719-1729, May 2003.

[13] L. Van Dao, C. Lincoln, M. Lowe, and P. Hannaford, "Spectrally resolved femtosecond two-colour three-pulse photon echoes: Study of ground and excited state dynamics in molecules," *Journal of Chemical Physics,* vol. 120, pp. 8434-8442, May 2004.

[14] W. Zinth and W. Kaiser, "Ultrafast laser pulses," in *Topics in Applied Physics* vol. 60, W. Kaiser, Ed. Berlin: Springer-Verlag, , 1988, p. 235.

[15] L. Van Dao and P. Hannaford, "Femtosecond nonlinear coherence spectroscopy of carrier dynamics in porous silicon," *Journal of Applied Physics,* vol. 98, 083508, Oct 2005.

[16] S. Mukamel, *Principles of nonlinear optical Spectroscopy.* New York: Oxford University Press, 1995.

[17] T. R. Nielsen, P. Gartner, and F. Jahnke, "Many-body theory of carrier capture and relaxation in semiconductor quantum-dot lasers," *Physical Review B,* vol. 69, p. 235314, 2004.

[18] M. Ando, T. J. Inagaki, Y. Kanemitsu, T. Kushida, K. Maehashi, Y. Murase, T. Ota, and H. Nakashima, "Photoluminescence properties of highly excited CdSe quantum dots," *Journal of Luminescence,* vol. 94, pp. 403-406, Dec 2001.

[19] F. Guffarth, R. Heitz, C. M. A. Kapteyn, F. Heinrichsdorff, and D. Bimberg, "State-filling and renormalization in charged InGaAs/GaAs quantum dots," *Physica E - Low-Dimensional Systems & Nanostructures,* vol. 13, pp. 278-282, Mar 2002.

[20] E. H. Bottcher, N. Kirstaedter, M. Grundmann, D. Bimberg, R. Zimmermann, C. Harder, and H. P. Meier, "Nonspectroscopic Approach to the Determination of the Chemical-Potential and Band-Gap Renormalization in Quantum-Wells," *Physical Review B,* vol. 45, pp. 8535-8541, Apr 15 1992.

[21] H. C. Schneider, W. W. Chow, and S. W. Koch, "Many-body effects in the gain spectra of highly excited quantum-dot lasers," *Physical Review B,* vol. 64, 115315, Sep 15 2001.

[22] M. Gatti and G. Onida, "Effects of local fields in time-dependent density functional theory shown in oxidized silicon clusters," *Physical Review B,* vol. 72, 045442, Jul 2005.

[23] H. L. Wang, K. Ferrio, D. G. Steel, Y. Z. Hu, R. Binder, and S. W. Koch, "Transient Nonlinear-Optical Response from Excitation Induced Dephasing in Gaas," *Physical Review Letters,* vol. 71, pp. 1261-1264, Aug 1993.

[24] H. L. Wang, J. Shah, T. C. Damen, and L. N. Pfeiffer, "Polarization-Dependent Coherent Nonlinear-Optical Response in Gaas Quantum-Wells - Dominant Effects of 2-Photon Coherence between Ground and Biexciton States," *Solid State Communications,* vol. 91, pp. 869-874, Sep 1994.

Chapter 3

[1] P. Y. Yu and M. Cardona, *Fundamentals of Semiconductors-physics and Materials properties*, third ed. Berlin: Springer-Verlag, 2005.

[2] B. D. Yacobi, *Semiconductor Materials-An Introduction to Basic Principles*. New York: Kluwer Academic /Plenum Publishers, 2003.

[3] O. Manasreh, *Semiconductor Heterojunctions and Nanostructures*. New York: McGraw Hill, 2005.

[4] J. A. Wang, U. A. Griesinger, F. Adler, H. Schweizer, V. Harle, and F. Scholz, "Size effect upon emission dynamics of 1.5 μm quasi-quantum wire distributed feedback semiconductor lasers," *Applied Physics Letters,* vol. 69, pp. 287-289, Jul 15 1996.

[5] R. Heitz, O. Stier, I. Mukhametzhanov, A. Madhukar, and D. Bimberg, "Quantum size effect in self-organized InAs/GaAs quantum dots," *Physical Review B,* vol. 62, pp. 11017-11028, Oct 15 2000.

[6] M. V. Maximov, A. F. Tsatsul'nikov, B. V. Volovik, D. A. Bedarev, Y. M. Shernyakov, I. N. Kaiander, E. Y. Kondrat'eva, A. E. Zhukov, A. R. Kovsh, N. A. Maleev, S. S. Mikhrin, V. M. Ustinov, Y. G. Musikhin, P. S. Kop'ev, Z. I. Alferov, R. Heitz, N. N. Ledentsov, and D. Bimberg, "Optical properties of quantum dots formed by activated spinodal decomposition for GaAs-based lasers emitting at similar to 1.3 μm," *Microelectronic Engineering,* vol. 51-2, pp. 61-72, May 2000.

[7] T. Winzell, I. Maximov, L. Landin, Y. Zhang, A. Gustafsson, L. Samuelson, and H. J. Whitlow, "Bandgap modification in GaInAs/InP quantum well structures using switched ion channelling lithography," *Semiconductor Science and Technology,* vol. 16, pp. 889-894, Nov 2001.

[8] C. Jagadish, G. Li, M. B. Johnston, and M. Gal, "Si and C delta-doping of GaAs grown by metal organic vapour phase epitaxy for fabrication of nipi doping superlattices," *Materials Science and Engineering B - Solid State Materials for Advanced Technology,* vol. 51, pp. 103-105, Feb 27 1998.

[9] L. Fu, R. W. van den Heijden, H. H. Tan, C. Jagadish, L. V. Dao, and M. Gal, "Study of intermixing in a GaAs/AlGaAs quantum-well structure using doped spin-on silica layers," *Applied Physics Letters,* vol. 80, pp. 1171-1173, Feb 18 2002.

[10] T. Steiner, *Semiconductor Nanostructures for Optoelectronic Applications*. Norwood: Artech House Inc., 2004.

[11] C. Rulliere, *Femtosecond Laser Pulses*, 2 ed: Springer, 2005.

[12] T. T. Yasuaki Masumoto, *Semiconductor Quantum Dots*, Heidelberg: Springer, 2002.

[13] P. Lever, H. H. Tan, C. Jagadish, P. Reece, and M. Gal, "Proton-irradiation-induced intermixing of InGaAs quantum dots," *Applied Physics Letters,* vol. 82, pp. 2053-2055, Mar 31 2003.

[14] L. V. Dao, M. Gal, C. Carmody, H. H. Tan, and C. Jagadish, "A comparison of impurity-free and ion-implantation-induced intermixing of InGaAs/InP quantum wells," *Journal of Applied Physics,* vol. 88, pp. 5252-5254, Nov 1 2000.

[15] O. Manasreh, *Semiconductor Heterojuctions and Nanostructures*: McGraw-Hill, 2005.

[16] M. Grundmann, *Nano-Optoelectronics-Concepts, Physics and Devices*. Berlin: Springer, 2002.

[17] K. Mukai, N. Ohtsuka, H. Shoji, and M. Sugawara, "Phonon bottleneck in self-formed InxGa1-xAs/GaAs quantum dots by electroluminescence and time-resolved photoluminescence," *Physical Review B,* vol. 54, pp. R5243-R5246, Aug 15 1996.

[18] T. Inoshita and H. Sakaki, "Electron Relaxation in a Quantum Dot - Significance of Multiphonon Processes," *Physical Review B,* vol. 46, pp. 7260-7263, Sep 15 1992.

[19] K. Seeger, *Semiconductor Physics*. Berlin: Springer, 1997.

[20] J. Shah, *Ultrafast Spectroscopy of Semiconductors and Semiconductor Nanostructures*. Berlin: Springer-Verlag, 1999.

[21] Y. Masumoto and T. Takagahara, *Semiconductor Quantum Dots - Physics, Spectroscopy and Applications*. Berlin: Springer-Verlag, 2002.

[22] B. K. Ridley, *Quantum processes in semiconductors*. Clarendon: Oxford, 1982.

[23] U. Bockelmann and G. Basterd, "Phonon scattering and energy relaxation in two-, one-, and zero-dimensional electron gases," *Physical Review B,* vol. 42, p. 8947, Nov. 1990.

Chapter 4

[1] C. Jagadish and S. J. Pearton, *Zinc Oxide Bulk, Thin Films and Nanostructures*. Oxford: Elsevier Ltd, 2006.

[2] T. Makino, Y. Segawa, M. Kawasaki, and H. Koinuma, "Optical properties of excitons in ZnO-based quantum well heterostructures," *Semiconductor Science and Technology*, vol. 20, pp. S78-S91, 2005.

[3] U. Ozgur, Y. I. Alivov, C. Liu, A. Teke, M. A. Reshchikov, S. Dogan, V. Avrutin, S. J. Cho, and H. Morkoc, "A comprehensive review of ZnO materials and devices," *Journal of Applied Physics*, vol. 98, 2005.

[4] S. J. Pearton, C. R. Abernathy, M. E. Overberg, G. T. Thaler, D. P. Norton, N. Theodoropoulou, A. F. Hebard, Y. D. Park, F. Ren, J. Kim, and L. A. Boatner, "Wide band gap ferromagnetic semiconductors and oxides," *Journal of Applied Physics*, vol. 93, pp. 1-13, 2003.

[5] F. K. Shan and Y. S. Yu, "Band gap energy of pure and Al-doped ZnO thin films," *Journal of the European Ceramic Society*, vol. 24, pp. 1869-1872, 2004.

[6] S. H. Park, K. J. Kim, S. N. Yi, D. Ahn, and S. J. Lee, "ZnO/ZnMgO quantum well lasers for optoelectronic applications in the blue and the UV spectral regions," *Journal of the Korean Physical Society*, vol. 47, pp. 448-453, 2005.

[7] I. Sakaguchi, S. Hishita, and H. Haneda, "Combinatorial ion implantation techniques application to optical characteristics of ZnO," *Japanese Journal of Applied Physics Part 1 - Regular Papers Short Notes & Review Papers*, vol. 43, pp. 5562-5563, 2004.

[8] Y. Y. Tay, S. Li, C. Q. Sun, and P. Chen, "Size dependence of Zn 2p 3/2 binding energy in nanocrystalline ZnO," *Applied Physics Letters*, vol. 88, 173118, 2006.

[9] C. H. Chia, T. Makino, K. Tamura, Y. Segawa, M. Kawasaki, A. Ohtomo, and H. Koinuma, "Confinement-enhanced biexciton binding energy in ZnO/ZnMgO multiple quantum wells," *Applied Physics Letters*, vol. 82, pp. 1848-1850, 2003.

[10] G. Coli and K. K. Bajaj, "Excitonic transitions in ZnO/MgZnO quantum well heterostructures," *Applied Physics Letters*, vol. 78, pp. 2861-2863, 2001.

[11] H. D. Sun, Y. Segawa, M. Kawasaki, A. Ohtomo, K. Tamura, and H. Koinuma, "Phonon replicas in ZnO/ZnMgO multiquantum wells," *Journal of Applied Physics*, vol. 91, pp. 6457-6460, 2002.

[12] H. D. Sun, T. Makino, Y. Segawa, M. Kawasaki, A. Ohtomo, K. Tamura, and H. Koinuma, "Enhancement of exciton binding energies in ZnO/ZnMgO multiquantum wells," *Journal of Applied Physics*, vol. 91, pp. 1993-1997, 2002.

[13] I. Ozerov, M. Arab, V. I. Safarov, W. Marine, S. Giorgio, M. Sentis, and L. Nanai, "Enhancement of exciton emission from ZnO nanocrystalline films by pulsed laser annealing," *Applied Surface Science*, vol. 226, pp. 242-248, 2004.

[14] F. Kreller, J. Puls, and F. Henneberger, "Temperature-dependent study of optical gain in (Zn,Cd)Se/ZnSe multiple-quantum-well structures," *Applied Physics Letters,* vol. 69, pp. 2406-2408, Oct 1996.

[15] F. Y. Jen, Y. C. Lu, C. Y. Chen, H. C. Wang, C. C. Yang, B. P. Zhang, and Y. Segawa, "Ultrafast biexciton dynamics in a ZnO thin film," *Applied Physics Letters*, vol. 87, 072103, 2005.

[16] S. Adachi, "Polarization and wave-vector-dependent measurements by four-wave mixing in ZnO: valence-band ordering and biexcitons," *Journal of Luminescence*, vol. 112, pp. 34-39, 2005.

[17] K. Hazu, T. Sota, K. Suzuki, S. Adachi, S. F. Chichibu, G. Cantwell, D. B. Eason, D. C. Reynolds, and C. W. Litton, "Strong biexcitonic effects and exciton-exciton correlations in ZnO," *Physical Review B*, vol. 68, 033205, 2003.

[18] J. A. Davis, L. Van Dao, X. M. Wen, P. Hannaford, V. A. Coleman, H. H. Tan, C. Jagadish, K. Koike, S. Sasa, M. Inoue, and M. Yano, "Observation of coherent biexcitons in ZnO/ZnMgO multiple quantum wells at room temperature," *Applied Physics Letters,* vol. 89, Art No 182109, Oct 2006.

[19] F. Z. Wang, H. P. He, Z. Z. Ye, and L. P. Zhu, "Photoluminescence properties of quasialigned

ZnCdO nanorods," *Journal of Applied Physics*, vol. 98, 084301, 2005.

[20] L. Vaillant, O. Vigil, G. Contreras-Puente, and C. Mejia-Garcia, "Optical and morphological characterization of (ZnO)(x)(CdO)(1-x) thin films," *Modern Physics Letters B*, vol. 15, pp. 663-666, 2001.

[21] B. S. Zou, V. V. Volkov, and Z. L. Wang, "Optical properties of amorphous ZnO, CdO, and PbO nanoclusters in solution," *Chemistry of Materials*, vol. 11, pp. 3037-3043, 1999.

[22] S. E. Paje, J. Llopis, M. E. Zayas, E. Rivera, A. Clark, and J. M. Rincon, "Photoluminescence in ZnO-CdO-SiO_2 Glasses," *Applied Physics A - Materials Science & Processing*, vol. 54, pp. 239-243, 1992.

[23] T. Gruber, C. Kirchner, R. Kling, F. Reuss, and A. Waag, "ZnMgO epilayers and ZnO-ZnMgO quantum wells for optoelectronic applications in the blue and UV spectral region," *Applied Physics Letters*, vol. 84, pp. 5359-5361, 2004.

[24] M. Fujita, R. Suzuki, M. Sasajima, T. Kosaka, Y. Deesirapipat, and Y. Horikoshi, "Molecular beam epitaxial growth of ZnMgO/ZnO/ZnMgO single quantum well structure on Si(111) substrate," *Journal of Vacuum Science & Technology B*, vol. 24, pp. 1668-1670, 2006.

[25] C. W. Sun, P. Xin, Z. W. Liu, and Q. Y. Zhang, "Room-temperature photoluminescence of ZnO/MgO multiple quantum wells on Si (001) substrates," *Applied Physics Letters*, vol. 88, 221914, 2006.

[26] V. A. Coleman, M. Buda, H. H. Tan, C. Jagadish, M. R. Phillips, K. Koike, S. Sasa, M. Inoue, and M. Yano, "Observation of blue shifts in ZnO/ZnMgO multiple quantum well structures by ion-implantation induced intermixing," *Semiconductor Science and Technology*, vol. 21, pp. L25-L28, 2006.

[27] S. H. Park, K. J. Kim, S. N. Yi, D. Ahn, and S. J. Lee, "Optical gain in wurtzite ZnO/ZnMgO quantum well lasers," *Japanese Journal of Applied Physics Part 2 - Letters & Express Letters*, vol. 44, pp. L1403-L1406, 2005.

[28] T. Makino, K. Tamura, C. H. Chia, Y. Segawa, M. Kawasaki, A. Ohtomo, and H. Koinuma, "Photoluminescence properties of ZnO epitaxial layers grown on lattice-matched $ScAlMgO_4$ substrates," *Journal of Applied Physics*, vol. 92, pp. 7157-7159, 2002.

[29] H. D. Sun, T. Makino, N. T. Tuan, Y. Segawa, Z. K. Tang, G. K. L. Wong, M. Kawasaki, A. Ohtomo, K. Tamura, and H. Koinuma, "Stimulated emission induced by exciton-exciton scattering in ZnO/ZnMgO multiquantum wells up to room temperature," *Applied Physics Letters*, vol. 77, pp. 4250-4252, 2000.

[30] T. Makino, C. H. Chia, N. T. Tuan, H. D. Sun, Y. Segawa, M. Kawasaki, A. Ohtomo, K. Tamura, and H. Koinuma, "Room-temperature luminescence of excitons in ZnO/(Mg, Zn)O multiple quantum wells on lattice-matched substrates," *Applied Physics Letters*, vol. 77, pp. 975-977, 2000.

[31] A. Ohtomo, M. Kawasaki, I. Ohkubo, H. Koinuma, T. Yasuda, and Y. Segawa, "Structure and optical properties of ZnO/$Mg_{0.2}Zn_{0.8}O$ superlattices," *Applied Physics Letters*, vol. 75, pp. 980-982, 1999.

[32] K. Koike, K. Hama, I. Nakashima, S. Sasa, M. Inoue, and M. Yano, "Molecular beam epitaxial growth of Al-doped ZnMgO alloy films for modulation-doped ZnO/ZnMgO heterostructures," *Japanese Journal of Applied Physics Part 1 - Regular Papers Short Notes & Review Papers*, vol. 44, pp. 3822-3827, 2005.

[33] H. M. Zhong, X. S. Chen, J. B. Wang, C. S. Xia, S. W. Wang, Z. F. Li, W. L. Xu, and W. Lu, "Preparation of ZnMnO by ion implantation and its spectral characterization," *Acta Physica Sinica*, vol. 55, pp. 2073-2077, 2006.

[34] G. Yaron, A. Many, and Y. Goldstein, "Quantized Electron Accumulation Layers on ZnO Surfaces Produced by Low-Energy Hydrogen-Ion Implantation," *Journal of Applied Physics*, vol. 58, pp. 3508-3514, 1985.

[35] G. Yaron, J. Levy, A. Many, Y. Goldstein, S. Z. Weisz, and O. Resto, "Low-Energy Hydrogen-Ion Implantation on Thermally Treated ZnO Surfaces," *Journal of Physics and Chemistry of Solids*, vol. 47, pp. 401-407, 1986.

[36] G. Braunstein, A. Muraviev, H. Saxena, N. Dhere, V. Richter, and R. Kalish, "p-type doping of zinc oxide by arsenic ion implantation," *Applied Physics Letters*, vol. 87, 192103, 2005.

[37] A. Tsukazaki, A. Ohtomo, T. Onuma, M. Ohtani, T. Makino, M. Sumiya, K. Ohtani, S. F. Chichibu, S. Fuke, Y. Segawa, H. Ohno, H. Koinuma, and M. Kawasaki, "Repeated temperature modulation epitaxy for p-type doping and light-emitting diode based on ZnO," *Nature Materials*, vol. 4, pp. 42-46, 2005.

[38] P. Vasa, B. P. Singh, and P. Ayyub, "Coherence properties of the photoluminescence from CdS-ZnO nanocomposite thin films," *Journal of Physics - Condensed Matter*, vol. 17, pp. 189-197, 2005.

[39] K. Koike, G. Takada, K. Fujimoto, S. Sasa, M. Inoue, and M. Yano, "Characterization of [ZnO](m)[ZnMgO](n) multiple quantum wells grown by molecular beam epitaxy," *Physica E - Low-Dimensional Systems & Nanostructures*, vol. 32, pp. 191-194, 2006.

[40] Z. W. Zhao, B. K. Tay, J. S. Chen, J. F. Hu, X. W. Sun, and S. T. Tan, "Optical properties of nanocluster-assembled ZnO thin films by nanocluster-beam deposition," *Applied Physics Letters*, vol. 87, 251912, 2005.

[41] J. Antony, X. B. Chen, J. Morrison, L. Bergman, Y. Qiang, D. E. McCready, and M. H. Engelhard, "ZnO nanoclusters: Synthesis and photoluminescence," *Applied Physics Letters*, vol. 87, 241917, 2005.

[42] S. Sadofev, S. Blumstengel, J. Cui, J. Puls, S. Rogaschewski, P. Schafer, Y. G. Sadofyev, and F. Henneberger, "Growth of high-quality ZnMgO epilayers and ZnO/ZnMgO quantum well structures by radical-source molecular-beam epitaxy on sapphire," *Applied Physics Letters*, vol. 87, 091903, 2005.

[43] H. M. Cheng, K. F. Lin, H. C. Hsu, and W. F. Hsieh, "Size dependence of photoluminescence and resonant Raman scattering from ZnO quantum dots," *Applied Physics Letters*, vol. 88, 261909, 2006.

[44] L. Q. Jing, F. L. Yuan, H. G. Hou, B. F. Xin, W. M. Cai, and H. G. Fu, "Relationships of surface oxygen vacancies with photoluminescence and photocatalytic performance of ZnO nanoparticles," *Science in China Series B - Chemistry*, vol. 48, pp. 25-30, 2005.

[45] T. Bretagnon, P. Lefebvre, P. Valvin, B. Gil, C. Morhain, and X. D. Tang, "Time resolved photoluminescence study of ZnO/(Zn,Mg)O quantum wells," *Journal of Crystal Growth*, vol. 287, pp. 12-15, 2006.

[46] T. Makino, N. T. Tuan, H. D. Sun, C. H. Chia, Y. Segawa, M. Kawasaki, A. Ohtomo, K. Tamura, T. Suemoto, H. Akiyama, M. Baba, S. Saito, T. Tomita, and H. Koinuma, "Temperature dependence of near ultraviolet photoluminescence in ZnO/(Mg, Zn)O multiple

quantum wells," *Applied Physics Letters*, vol. 78, pp. 1979-1981, 2001.

[47] Y. Zhang, B. X. Lin, X. K. Sun, and Z. X. Fu, "Temperature-dependent photoluminescence of nanocrystalline ZnO thin films grown on Si (100) substrates by the sol-gel process," *Applied Physics Letters*, vol. 86, 131910, 2005.

[48] S. Monticone, R. Tufeu, and A. V. Kanaev, "Complex nature of the UV and visible fluorescence of colloidal ZnO nanoparticles," *Journal of Physical Chemistry B*, vol. 102, pp. 2854-2862, 1998.

[49] W. Shan, W. Walukiewicz, J. W. Ager, K. M. Yu, H. B. Yuan, H. P. Xin, G. Cantwell, and J. J. Song, "Nature of room-temperature photoluminescence in ZnO," *Applied Physics Letters*, vol. 86, 2005.

[50] C. Morhain, T. Bretagnon, P. Lefebvre, X. Tang, P. Valvin, T. Guillet, B. Gil, T. Taliercio, M. Teisseire-Doninelli, B. Vinter, and C. Deparis, "Internal electric field in wurtzite ZnO/Zn0.78Mg0.22O quantum wells," *Physical Review B,* vol. 72, 241305, Dec 2005.

[51] B. Gil, P. Lefebvre, T. Bretagnon, T. Guillet, J. A. Sans, T. Taliercio, and C. Morhain, "Spin-exchange interaction in ZnO-based quantum wells," *Physical Review B,* vol. 74, 153302, Oct 2006.

[52] K. P. Vijayakumar, P. M. R. Kumar, C. S. Kartha, K. C. Wilson, F. Singh, K. G. M. Nair, and Y. Kashiwaba, "Effects of oxygen ion implantation in spray-pyrolyzed ZnO thin films," *Physica Status Solidi A - Applications and Materials Science,* vol. 203, pp. 860-867, Apr 2006.

[53] S. O. Kucheyev, J. S. Williams, C. Jagadish, J. Zou, C. Evans, A. J. Nelson, and A. V. Hamza, "Ion-beam-produced structural defects in ZnO," *Physical Review B,* vol. 67, 094115, Mar 2003.

[54] T. Makino, K. Tamura, C. H. Chia, Y. Segawa, M. Kawasaki, A. Ohtomo, and H. Koinuma, "Temperature quenching of exciton luminescence intensity in ZnO/(Mg,Zn)O multiple quantum wells," *Journal of Applied Physics,* vol. 93, pp. 5929-5933, May 2003.

[55] X. M. Wen, N. Ohno, and Z. M. Zhang, "Time-resolved photoluminescence of sintered ZnO ceramics," *Chinese Physics,* vol. 10, pp. 874-876, Sep 2001.

[56] S. F. Chichibu, T. Onuma, M. Kubota, A. Uedono, T. Sota, A. Tsukazaki, A. Ohtomo, and M. Kawasaki, "Improvements in quantum efficiency of excitonic emissions in ZnO epilayers by the elimination of point defects," *Journal of Applied Physics,* vol. 99, 093505, May 2006.

[57] T. Koida, A. Uedono, A. Tsukazaki, T. Sota, M. Kawasaki, and S. F. Chichibu, "Direct comparison of photoluminescence lifetime and defect densities in ZnO epilayers studied by time-resolved photoluminescence and slow positron annihilation techniques," *Physica Status Solidi A - Applied Research,* vol. 201, pp. 2841-2845, Sep 2004.

[58] Z. Q. Chen, M. Maekawa, T. Sekiguchi, R. Suzuki, and A. Kawasuso, "Ion-implantation induced defects in ZnO studied by a slow positron beam," in *Positron Annihilation, ICPA-13, Proceedings*. vol. 445-4, 2004, pp. 57-59.

[59] Z. Q. Chen, T. Sekiguchi, X. L. Yuan, M. Maekawa, and A. Kawasuso, "N+ ion-implantation-induced defects in ZnO studied with a slow positron beam," *Journal of Physics - Condensed Matter,* vol. 16, pp. S293-S299, Jan 2004.

[60] A. F. Kohan, G. Ceder, D. Morgan, and C. G. Van de Walle, "First-principles study of native point defects in ZnO," *Physical Review B,* vol. 61, pp. 15019-15027, Jun 2000.

[61] C. G. Van de Walle, "Defect analysis and engineering in ZnO," *Physica B - Condensed Matter,*

vol. 308, pp. 899-903, Dec 2001.

[62] Z. Q. Chen, M. Maekawa, A. Kawasuso, S. Sakai, and H. Naramoto, "Annealing process of ion-implantation-induced defects in ZnO: Chemical effect of the ion species," *Journal of Applied Physics,* vol. 99, 093507, May 2006.

[63] S. O. Kucheyev, J. S. Williams, and C. Jagadish, "Ion-beam-defect processes in group-III nitrides and ZnO," *Vacuum,* vol. 73, pp. 93-104, Mar 2004.

[64] K. Ip, M. E. Overberg, Y. W. Heo, D. P. Norton, S. J. Pearton, S. O. Kucheyev, C. Jagadish, J. S. Williams, R. G. Wilson, and J. M. Zavada, "Thermal stability of ion-implanted hydrogen in ZnO," *Applied Physics Letters,* vol. 81, pp. 3996-3998, Nov 2002.

[65] Z. X. Mei, X. Q. Zhang, Z. J. Wang, Q. F. Li, and X. R. Xu, "Properties of the stimulated emission in the ZnO thin film," *Spectroscopy and Spectral Analysis,* vol. 23, pp. 461-464, Jun 2003.

[66] J. Wang, Y. Q. Mang, X. Y. Teng, D. P. Xiong, P. Lin, L. Wang, and S. H. Huang, "Stimulated emission characteristics of ZnO thin films deposited by magnetron sputtering on SiO2 substrates," *Spectroscopy and Spectral Analysis,* vol. 24, pp. 775-778, Jul 2004.

[67] H. D. Sun, T. Makino, Y. Segawa, M. Kawasaki, A. Ohtomo, K. Tamura, and H. Koinuma, "Biexciton emission from ZnO/Zn0.74Mg0.26O multiquantum wells," *Applied Physics Letters,* vol. 78, pp. 3385-3387, May 2001.

[68] K. Hazu, T. Sota, K. Suzuki, S. Adachi, S. F. Chichibu, G. Cantwell, D. B. Eason, D. C. Reynolds, and C. W. Litton, "Strong biexcitonic effects and exciton-exciton correlations in ZnO," *Physical Review B,* vol. 68, 033205, Jul 2003.

[69] H. D. Sun, Y. Segawa, T. Makino, C. H. Chia, M. Kawasaki, A. Ohtomo, K. Tamura, and H. Koinuma, "Observation of biexciton emission in ZnO/ZnMgO multi-quantum wells," *Physica Status Solidi B - Basic Research,* vol. 229, pp. 867-870, Jan 2002.

[70] W. Langbein, J. M. Hvam, M. Umlauff, H. Kalt, B. Jobst, and D. Hommel, "Binding-energy distribution and dephasing of localized biexcitons," *Physical Review B,* vol. 55, pp. R7383-R7386, Mar 1997.

[71] J. Shah, *Ultrafast Spectroscopy of Semiconductors and Semiconductor Nanostructures*. Berlin: Springer, 1999.

[72] B. F. Feuerbacher, J. Kuhl, and K. Ploog, "Biexcitonic Contribution to the Degenerate-4-Wave-Mixing Signal from a GaAs/$Al_xGa_{1-X}As$ Quantum-Well," *Physical Review B,* vol. 43, pp. 2439-2441, Jan 1991.

[73] H. L. Wang, J. Shah, T. C. Damen, and L. N. Pfeiffer, "Polarization-Dependent Coherent Nonlinear-Optical Response in GaAs Quantum-Wells - Dominant Effects of 2-Photon Coherence between Ground and Biexciton States," *Solid State Communications,* vol. 91, pp. 869-874, Sep 1994.

[74] C. K. Sun, S. Z. Sun, K. H. Lin, K. Y. J. Zhang, H. L. Liu, S. C. Liu, and J. J. Wu, "Ultrafast carrier dynamics in ZnO nanorods," *Applied Physics Letters,* vol. 87, 023106, Jul 2005.

Chapter 5

[1] L. Jacak, P. Hawrylak, and A. Wojs, *Quantum dots*. Berlin: Springer Verlag, 1998.

[2] D. Bimberg, M. Grundmann, and N. N. Ledentsov, *Quantum Dot Heterostructures*. New York: John Wiley & Son Ltd, 1999.

[3] D. G. Deppe, H. Huang, and O. B. Shchekin, "Modulation characteristics of quantum-dot lasers: The influence of p-type doping and the electronic density of states on obtaining high speed," *IEEE Journal of Quantum Electronics,* vol. 38, pp. 1587-1593, Dec 2002.

[4] H. Drexler, D. Leonard, W. Hansen, J. P. Kotthaus, and P. M. Petroff, "Spectroscopy of Quantum Levels in Charge-Tunable InGaAs Quantum Dots," *Physical Review Letters,* vol. 73, pp. 2252-2255, Oct 17 1994.

[5] J. Y. Marzin, J. M. Gerard, A. Izrael, D. Barrier, and G. Bastard, "Photoluminescence of Single InAs Quantum Dots Obtained by Self-Organized Growth on GaAs," *Physical Review Letters,* vol. 73, pp. 716-719, Aug 1 1994.

[6] L. Fu, R. Lever, K. Sears, H. H. Tan, and C. Jagadish, "$In_{0.5}Ga_{0.5}As$/GaAs quantum dot infrared photodetectors grown by metal-organic chemical vapor deposition," *IEEE Electron Device Letters,* vol. 26, pp. 628-630, Sep 2005.

[7] N. Li, W. Lu, X. Q. Liu, X. Z. Yuan, Z. F. Li, H. F. Dou, S. C. Shen, Y. Fu, M. Willander, L. Fu, H. H. Tan, C. Jagadish, M. B. Johnston, and M. Gal, "Proton implantation and rapid thermal annealing effects on GaAs/AlGaAs quantum well infrared photodetectors," *Superlattices and Microstructures,* vol. 26, pp. 317-324, Nov 1999.

[8] H. S. Park and V. G. Mokerov, "High electric field transport in modulation-doped InAs self-assembled quantum dots for high-frequency applications," *Applied Physics Letters,* vol. 79, pp. 418-420, Jul 16 2001.

[9] K. C. Hall, W. H. Lau, K. Gundogdu, M. E. Flatte, and T. F. Boggess, "Nonmagnetic semiconductor spin transistor," *Applied Physics Letters,* vol. 83, pp. 2937-2939, Oct 6 2003.

[10] H. W. Li and T. H. Wang, "Memory and tunneling effects in metal-semiconductor-metal contacts," *Physics of Low-Dimensional Structures,* vol. 5-6, pp. 129-137, 2001.

[11] M. Grundmann, F. Heinrichsdorff, C. Ribbat, M. H. Mao, and D. Bimberg, "Quantum dot lasers: recent progress in theoretical understanding and demonstration of high-output-power operation," *Applied Physics B - Lasers and Optics,* vol. 69, pp. 413-416, Nov-Dec 1999.

[12] H. Bensity, C. M. Sotomayor-Torres, and C. Weisbuch, "Intrinsic mechanism for the poor luminescence properties of quantum-box systems," *Physical Review B,* vol. 44, p. 10945, 1991.

[13] U. Bockelmann and G. Basterd, "Phonon scattering and energy relaxation in two-, one-, and zero-dimensional electron gases," *Physical Review B,* vol. 42, p. 8947, Nov. 1990 1990.

[14] F. Adler, M. Geiger, A. Bauknecht, F. Scholz, H. Schweizer, M. H. Pilkuhn, B. Ohnesorge, and A. Forchel, "Optical transitions and carrier relaxation in self assembled InAs/GaAs quantum dots," *Journal of Applied Physics,* vol. 80, pp. 4019-4026, Oct 1 1996.

[15] H. Benisty, "Reduced Electron-Phonon Relaxation Rates in Quantum-Box Systems - Theoretical-Analysis," *Physical Review B,* vol. 51, pp. 13281-13293, May 15 1995.

[16] U. Bockelmann and T. Egeler, "Electron relaxation in quantum dots by means of Auger processes," *Physical Review B,* vol. 46, p. 15574, 1992 1992.

[17] D. G. Deppe, O. Shchekin, G. Park, T. F. Boggess, and L. Zhang, "Carrier dynamics, laser characteristics, and microcavity effects based on InAs and InGaAs quantum dot light emitters," *Journal of the Korean Physical Society,* vol. 39, pp. S398-S401, Dec 2001.

[18] K. Gundogdu, K. C. Hall, T. F. Boggess, D. G. Deppe, and O. B. Shchekin, "Ultrafast electron capture into p-modulation-doped quantum dots," *Applied Physics Letters,* vol. 85, pp. 4570-4572, Nov 15 2004.

[19] R. Heitz, M. Veit, N. N. Ledentsov, A. Hoffmann, D. Bimberg, V. M. Ustinov, P. S. Kopev, and Z. I. Alferov, "Energy relaxation by multiphonon processes in InAs/GaAs quantum dots," *Physical Review B,* vol. 56, pp. 10435-10445, Oct 15 1997.

[20] T. Inoshita and H. Sakaki, "Electron relaxation in a quantum dot: Significance of multiphonon processes," *Physical Review B,* vol. 46, p. 7260, Sep. 1992 1992.

[21] T. R. Nielsen, P. Gartner, and F. Jahnke, "Many-body theory of carrier capture and relaxation in semiconductor quantum-dot lasers," *Physical Review B,* vol. 69, p. 235314, 2004.

[22] T. S. Sosnowski, T. B. Norris, H. Jiang, J. Singh, K. Kamath, and P. Bhattacharya, "Rapid carrier relaxation in $In_{0.4}Ga_{0.6}As$/GaAs quantum dots characterized by differential transmission spectroscopy," *Physical Review B,* vol. 57, pp. R9423-R9426, Apr 15 1998.

[23] T. Inoshita and H. Sakaki, "Electron-phonon interaction and the so-called phonon bottleneck effect in semiconductor quantum dots," *Physica B,* vol. 227, pp. 373-377, Sep 1996.

[24] X. Q. Li, H. Nakayama, and Y. Arakawa, "Phonon bottleneck in quantum dots: Role of lifetime of the confined optical phonons," *Physical Review B,* vol. 59, pp. 5069-5073, Feb 15 1999.

[25] K. Mukai, N. Ohtsuka, H. Shoji, and M. Sugawara, "Phonon bottleneck in self-formed InxGa1-xAs/GaAs quantum dots by electroluminescence and time-resolved photoluminescence," *Physical Review B,* vol. 54, pp. R5243-R5246, Aug 15 1996.

[26] J. Urayama, T. B. Norris, J. Singh, and P. Bhattacharya, "Observation of phonon bottleneck in quantum dot electronic relaxation," *Physical Review Letters,* vol. 86, pp. 4930-4933, May 21 2001.

[27] A. V. Uskov, J. McInerney, F. Adler, H. Schweizer, and M. H. Pilkuhn, "Auger carrier capture kinetics in self-assembled quantum dot structures," *Applied Physics Letters,* vol. 72, pp. 58-60, Jan 5 1998.

[28] T. Muller, F. F. Schrey, G. Strasser, and K. Unterrainer, "Ultrafast intraband spectroscopy of electron capture and relaxation in InAs/GaAs quantum dots," *Applied Physics Letters,* vol. 83, pp. 3572-3574, Oct 27 2003.

[29] U. Bockelmann and T. Egeler, "Electron Relaxation in Quantum Dots by Means of Auger Processes," *Physical Review B,* vol. 46, pp. 15574-15577, Dec 15 1992.

[30] V. A. Belyakov, V. A. Burdov, D. M. Gaponova, A. N. Mikhaylov, D. I. Tetelbaum, and S. A. Trushin, "Phonon-assisted radiative electron-hole recombination in silicon quantum dots," *Physics of the Solid State,* vol. 46, pp. 27-31, 2004.

[31] R. Cingolani, R. Rinaldi, H. Lipsanen, M. Sopanen, R. Virkkala, K. Maijala, J. Tulkki, J. Ahopelto, K. Uchida, N. Miura, and Y. Arakawa, "Electron-hole correlation in quantum dots

under a high magnetic field (up to 45 T)," *Physical Review Letters,* vol. 83, pp. 4832-4835, Dec 6 1999.

[32] L. Zhang, T. F. Boggess, K. Gundogdu, M. E. Flatte, D. G. Deppe, C. Cao, and O. B. Shchekin, "Excited-state dynamics and carrier capture in InGaAs/GaAs quantum dots," *Applied Physics Letters,* vol. 79, pp. 3320-3322, Nov 12 2001.

[33] R. D. Schaller, J. M. Pietryga, S. V. Goupalov, M. A. Petruska, S. A. Ivanov, and V. I. Klimov, "Breaking the phonon bottleneck in semiconductor nanocrystals via multiphonon emission induced by intrinsic nonadiabatic interactions," *Physical Review Letters,* vol. 95, p. 196401, Nov 4 2005.

[34] T. Inoshita and H. Sakaki, "Multiphonon Relaxation of Electrons in a Semiconductor Quantum-Dot," *Solid-State Electronics,* vol. 37, pp. 1175-1178, Apr-Jun 1994.

[35] R. Heitz, M. Grundmann, N. N. Ledentsov, L. Eckey, M. Veit, D. Bimberg, V. M. Ustinov, A. Y. Egorov, A. E. Zhukov, P. S. Kopev, and Z. I. Alferov, "Multiphonon-relaxation processes in self-organized InAs/GaAs quantum dots," *Applied Physics Letters,* vol. 68, pp. 361-363, Jan 15 1996.

[36] T. Inoshita and H. Sakaki, "Electron Relaxation in a Quantum Dot - Significance of Multiphonon Processes," *Physical Review B,* vol. 46, pp. 7260-7263, Sep 15 1992.

[37] R. Heitz, H. Born, F. Guffarth, O. Stier, A. Schliwa, A. Hoffmann, and D. Bimberg, "Existence of a phonon bottleneck for excitons in quantum dots," *Physical Review B,* vol. 64, Dec 15 2001.

[38] A. L. Efros, V. A. Kharchenko, and M. Rosen, "Breaking the Phonon Bottleneck in Nanometer Quantum Dots - Role of Auger-Like Processes," *Solid State Communications,* vol. 93, pp. 281-284, Jan 1995.

[39] R. Ferreira and G. Bastard, "Phonon-assisted capture and intradot Auger relaxation in quantum dots," *Applied Physics Letters,* vol. 74, pp. 2818-2820, May 10 1999.

[40] T. Inoshita and H. Sakaki, "Density of states and phonon-induced relaxation of electrons in semiconductor quantum dots," *Physical Review B,* vol. 56, pp. R4355-R4358, Aug 15 1997.

[41] T. R. Nielsen, P. Gartner, and F. Jahnke, "Many-body theory of carrier capture and relaxation in semiconductor quantum-dot lasers," *Physical Review B,* vol. 69, Jun 2004.

[42] A. V. Uskov, F. Adler, H. Schweizer, and M. H. Pilkuhn, "Auger carrier relaxation in self-assembled quantum dots by collisions with two-dimensional carriers," *Journal of Applied Physics,* vol. 81, pp. 7895-7899, Jun 15 1997.

[43] T. R. Nielsen, P. Gartner, M. Lorke, J. Seebeck, and F. Jahnke, "Coulomb scattering in nitride-based self-assembled quantum dot systems," *Physical Review B,* vol. 72, Dec 2005.

[44] X. Q. Li and Y. Arakawa, "Ultrafast energy relaxation in quantum dots through defect states: A lattice-relaxation approach," *Physical Review B,* vol. 56, pp. 10423-10427, Oct 15 1997.

[45] O. B. Shchekin and D. G. Deppe, "The role of p-type doping and the density of states on the modulation response of quantum dot lasers," *Applied Physics Letters,* vol. 80, pp. 2758-2760, Apr 15 2002.

[46] O. B. Shchekin, J. Ahn, and D. G. Deppe, "High temperature performance of self-organised quantum dot laser with stacked p-doped active region," *Electronics Letters,* vol. 38, pp. 712-713, Jul 4 2002.

[47] S. Grosse, J. H. H. Sandmann, G. vonPlessen, J. Feldmann, H. Lipsanen, M. Sopanen, J. Tulkki, and J. Ahopelto, "Carrier relaxation dynamics in quantum dots: Scattering mechanisms and state-filling effects," *Physical Review B,* vol. 55, pp. 4473-4476, Feb 15 1997.

[48] O. B. Shchekin, D. G. Deppe, and D. Lu, "Fermi-level effect on the interdiffusion of InAs and InGaAs quantum dots," *Applied Physics Letters,* vol. 78, pp. 3115-3117, May 14 2001.

[49] J. Siegert, A. Gaarder, S. Marcinkevicius, R. Leon, S. Chaparro, S. R. Johnson, Y. Sadofyev, and Y. H. Zhang, "Photoexcited carrier dynamics in aligned InAs/GaAs quantum dots grown on strain-relaxed InGaAs layers," *Physica E - Low-Dimensional Systems & Nanostructures,* vol. 18, pp. 541-546, Jun 2003.

[50] C. Walther, J. Bollmann, H. Kissel, H. Kirmse, W. Neumann, and W. T. Masselink, "Non-exponential capture of electrons in GaAs with embedded InAs quantum dots," *Physica B-Condensed Matter,* vol. 274, pp. 971-975, Dec 1999.

[51] J. Siegert, S. Marcinkevicius, and Q. X. Zhao, "Carrier dynamics in modulation-doped InAs/GaAs quantum dots," *Physical Review B,* vol. 72, 085316, Aug 2005.

[52] D. V. Regelman, E. Dekel, D. Gershoni, E. Ehrenfreund, A. J. Williamson, J. Shumway, A. Zunger, W. V. Schoenfeld, and P. M. Petroff, "Optical spectroscopy of single quantum dots at tunable positive, neutral, and negative charge states," *Physical Review B,* vol. 64, art. no.165301, Oct 15 2001.

[53] L. Landin, M. S. Miller, M.-E. Pistol, C. E. Pryor, and L. Samuelson, "Optical studies of individal InAs quantum dots in GaAs: Few-particle effects," *Science,* vol. 280, pp. 262-264, April 1998.

[54] K. H. Schmidt, G. Medeiros-Ribeiro, and P. M. Petroff, "Photoluminescence of charged InAs self-assembled quantum dots," *Physical Review B,* vol. 58, pp. 3597-3600, Aug 15 1998.

[55] J. Siegert, S. Marcinkevicius, L. Fu, and C. Jagadish, "Recombination properties of Si-doped InGaAs/GaAs quantum dots," *Nanotechnology,* vol. 17, pp. 5373-5377, Nov 2006.

[56] S. Raymond, X. Guo, J. L. Merz, and S. Fafard, "Excited-state radiative lifetimes in self-assembled quantum dots obtained from state-filling spectroscopy," *Physical Review B,* vol. 59, pp. 7624-7631, Mar 15 1999.

[57] R. Ferreira and G. Bastard, "Carrier capture and intra-dot Auger relaxation in quantum dots," *Physica E - Low-Dimensional Systems & Nanostructures,* vol. 7, pp. 342-345, May 2000.

[58] P. C. Sercel, "Multiphonon-Assisted Tunneling through Deep Levels - a Rapid Energy-Relaxation Mechanism in Nonideal Quantum-Dot Heterostructures," *Physical Review B,* vol. 51, pp. 14532-14541, May 15 1995.

[59] I. C. Sandall, P. M. Smowton, C. L. Walker, T. Badcock, D. J. Mowbray, H. Y. Liu, and M. Hopkinson, "The effect of p doping in InAs quantum dot lasers," *Applied Physics Letters,* vol. 88, 111113, Mar 2006.

[60] S. Raymond, S. Fafard, P. J. Poole, A. Wojs, P. Hawrylak, C. Gould, A. Sachrajda, S. Charbonneau, D. Leonard, R. Leon, P. M. Petroff, and J. L. Merz, "State-filling and magneto-photoluminescence of excited states in InGaAs/GaAs self-assembled quantum dots," *Superlattices and Microstructures,* vol. 21, pp. 541-558, 1997.

[61] S. Osborne, P. Blood, P. Smowton, J. Lutti, Y. C. Xin, A. Stintz, D. Huffaker, and L. F. Lester, "State filling in InAs quantum-dot laser structures," *IEEE Journal of Quantum Electronics,* vol. 40, pp. 1639-1645, Dec 2004.

[62] Y. M. Park, Y. J. Park, K. M. Kim, J. C. Shin, J. D. Song, J. I. Lee, and K. H. Yoo, "State filling phenomena in modulation-doped InAs quantum dots," *Journal of Crystal Growth,* vol. 271, pp. 385-390, Nov 15 2004.

[63] M. Grundmann, R. Heitz, N. Ledentsov, O. Stier, D. Bimberg, V. M. Ustinov, P. S. Kopev, Z. I. Alferov, S. S. Ruvimov, P. Werner, U. Gosele, and J. Heydenreich, "Electronic structure and energy relaxation in strained InAs/GaAs quantum pyramids," *Superlattices and Microstructures,* vol. 19, pp. 81-95, 1996.

[64] W. D. Yang, H. Lee, T. J. Johnson, P. C. Sercel, and A. G. Norman, "Electronic structure of self-organized InAs/GaAs quantum dots bounded by {136} facets," *Physical Review B,* vol. 61, pp. 2784-2793, Jan 15 2000.

[65] H. C. Schneider, W. W. Chow, and S. W. Koch, "Many-body effects in the gain spectra of highly excited quantum-dot lasers," *Physical Review B,* vol. 6411, Sep 15 2001.

[66] L. Van Dao, X. M. Wen, M. T. T. Do, P. Hannaford, E. C. Cho, Y. H. Cho, and Y. D. Huang, "Time-resolved and time-integrated photoluminescence analysis of state filling and quantum confinement of silicon quantum dots," *Journal of Applied Physics,* vol. 97, Jan 1 2005.

[67] W. D. Sheng and J. P. Leburton, "Interband transition distributions in the optical spectra of InAs/GaAs self-assembled quantum dots," *Applied Physics Letters,* vol. 80, pp. 2755-2757, Apr 15 2002.

[68] O. Stier, M. Grundmann, and D. Bimberg, "Electronic and optical properties of strained quantum dots modeled by 8-band k center dot p theory," *Physical Review B,* vol. 59, pp. 5688-5701, Feb 15 1999.

[69] M. Grundmann and D. Bimberg, "Theory of random population for quantum dots," *Physical Review B,* vol. 55, pp. 9740-9745, Apr 15 1997.

[70] J. H. Marsh, O. P. Kowalski, S. D. McDougall, B. C. Qiu, A. McKee, C. J. Hamilton, R. M. De la Rue, and A. C. Bryce, "Quantum well intermixing in material systems for 1.5μm," *Journal of Vacuum Science & Technology A,* vol. 16, pp. 810-816, Mar-Apr 1998.

[71] G. F. Redinbo, H. G. Craighead, and J. M. H. Hong, "Proton Implantation Intermixing of GaAs/AlGaAs Quantum-Wells," *Journal of Applied Physics,* vol. 74, pp. 3099-3102, Sep 1 1993.

[72] J. Micallef, A. Brincat, and W. C. Shiu, "Effects of interdiffusion-induced strain in $Ga_{0.5}In_{0.49}P$-GaAs intermixed quantum wells," *IEEE Journal of Selected Topics in Quantum Electronics,* vol. 4, pp. 675-684, Jul-Aug 1998.

[73] H. S. Djie, T. Mei, J. Arokiaraj, C. Sookdhis, S. F. Yu, L. K. Ang, and X. H. Tang, "Experimental and theoretical analysis of argon plasma-enhanced quantum-well intermixing," *IEEE Journal of Quantum Electronics,* vol. 40, pp. 166-174, Feb 2004.

[74] T. Mei, H. S. Djie, J. Aroklaraj, and C. Sookdhis, "Understanding the inductively coupled argon plasma-enhanced quantum well intermixing," *Journal of Crystal Growth,* vol. 268, pp. 384-388, Aug 1 2004.

[75] M. Paquette, V. Aimez, J. Beauvais, J. Beerens, P. J. Poole, S. Charbonneau, and A. P. Roth, "Blueshifting of InGaAsP-InP laser diodes using a low-energy ion-implantation technique: Comparison between strained and lattice-matched quantum-well structures," *IEEE Journal of Selected Topics in Quantum Electronics,* vol. 4, pp. 741-745, Jul-Aug 1998.

[76] V. Aimez, J. Beauvais, J. Beerens, D. Morris, H. S. Lim, and B. S. Ooi, "Low-energy ion-implantation-induced quantum-well intermixing," *IEEE Journal of Selected Topics in Quantum Electronics,* vol. 8, pp. 870-879, Jul-Aug 2002.

[77] I. Gontijo, T. Krauss, J. H. Marsh, and R. M. Delarue, "Postgrowth Control of GaAs/AlGaAs Quantum-Well Shapes by Impurity-Free Vacancy Diffusion," *IEEE Journal of Quantum Electronics,* vol. 30, pp. 1189-1195, May 1994.

[78] N. Holonyak, "Impurity-induced layer disordering of quantum-well heterostructures: Discovery and prospects," *IEEE Journal of Selected Topics in Quantum Electronics,* vol. 4, pp. 584-594, Jul-Aug 1998.

[79] H. Konig, S. Rennon, J. P. Reithmaier, A. Forchel, J. L. Gentner, and L. Goldstein, "1.55μm single mode lasers with complex coupled distributed feedback gratings fabricated by focused ion beam implantation," *Applied Physics Letters,* vol. 75, pp. 1491-1493, Sep 13 1999.

[80] H. Konig, N. Mais, E. Hofling, J. P. Reithmaier, A. Forchel, H. Mussig, and H. Brugger, "Focused ion beam implantation for opto- and microelectronic devices," *Journal of Vacuum Science & Technology B,* vol. 16, pp. 2562-2566, Jul-Aug 1998.

[81] J. P. Reithmaier and A. Forchel, "Focused ion-beam implantation induced thermal quantum-well intermixing for monolithic optoelectronic device integration," *IEEE Journal of Selected Topics in Quantum Electronics,* vol. 4, pp. 595-605, Jul-Aug 1998.

[82] S. Charbonneau, E. S. Koteles, P. J. Poole, J. J. He, G. C. Aers, J. Haysom, M. Buchanan, Y. Feng, A. Delage, F. Yang, M. Davies, R. D. Goldberg, P. G. Piva, and I. V. Mitchell, "Photonic integrated circuits fabricated using ion implantation," *IEEE Journal of Selected Topics in Quantum Electronics,* vol. 4, pp. 772-793, Jul-Aug 1998.

[83] P. Lever, H. H. Tan, C. Jagadish, P. Reece, and M. Gal, "Proton-irradiation-induced intermixing of InGaAs quantum dots," *Applied Physics Letters,* vol. 82, pp. 2053-2055, Mar 31 2003.

[84] X. Q. Liu, N. Li, W. Lu, X. Z. Yuan, S. C. Shen, L. Fu, H. H. Tan, and C. Jagadish, "Wavelength tuning of GaAs/AlGaAs quantum-well infrared photo-detectors by proton implantation induced intermixing," *Japanese Journal of Applied Physics Part 1 - Regular Papers Short Notes & Review Papers,* vol. 39, pp. 1687-1689, Apr 2000.

[85] L. Fu, H. H. Tan, M. B. Johnston, M. Gal, and C. Jagadish, "Proton irradiation-induced intermixing in InGaAs/(Al)GaAs quantum wells and quantum-well lasers," *Journal of Applied Physics,* vol. 85, pp. 6786-6789, May 1 1999.

[86] X. Q. Liu, X. S. Chen, Z. F. Li, W. Lu, S. C. Shen, H. H. Tan, S. Yuan, and C. Jagadish, "Proton implantation-induced intermixing effects on AlGaAs/GaAs single QW structures," *Physics Letters A,* vol. 278, pp. 99-102, Dec 18 2000.

[87] N. Y. Tang, Y. L. Ji, X. S. Chen, and L. Wei, "Effect of proton implantation on photoluminescence of self-assembled InAs/GaAs quantum dots," *Acta Physica Sinica,* vol. 54, pp. 2904-2909, Jun 2005.

[88] S. Weiss, J. M. Wiesenfeld, D. S. Chemla, G. Raybon, G. Sucha, M. Wegener, G. Eisenstein, C. A. Burrus, A. G. Dentai, U. Koren, B. I. Miller, H. Temkin, R. A. Logan, and T. Tanbunek, "Carrier capture times in 1.5 μm multiple quantum-well optical amplifiers," *Applied Physics Letters,* vol. 60, pp. 9-11, Jan 6 1992.

[89] L. V. Dao, M. Gal, H. Tan, and C. Jagadish, "Carrier capture into InGaAs/GaAs quantum wells via impurity mediated resonant tunnelling," *Applied Physics Letters,* vol. 72, pp. 2008-2010, Apr 20 1998.

[90] S. Marcinkevicius and R. Leon, "Carrier capture and escape in InxGa1-xAs/GaAs quantum dots: Effects of intermixing," *Physical Review B,* vol. 59, pp. 4630-4633, Feb 15 1999.

[91] R. Kersting, R. Schwedler, K. Wolter, K. Leo, and H. Kurz, "Dynamics of Carrier Transport and Carrier Capture in $In_{1-x}Ga_xAs$/InP Heterostructures," *Physical Review B,* vol. 46, pp. 1639-1648, Jul 15 1992.

[92] P. W. M. Blom, C. Smit, J. E. M. Haverkort, and J. H. Wolter, "Carrier Capture into a Semiconductor Quantum-Well," *Physical Review B,* vol. 47, pp. 2072-2081, Jan 15 1993.

[93] H. J. Chen, H. A. McKay, R. M. Feenstra, G. C. Aers, P. J. Poole, R. L. Williams, S. Charbonneau, P. G. Piva, T. W. Simpson, and I. V. Mitchell, "InGaAs/InP quantum well intermixing studied by cross-sectional scanning tunneling microscopy," *Journal of Applied Physics,* vol. 89, pp. 4815-4823, May 1 2001.

[94] T. Yin, G. J. Letal, B. J. Robinson, and D. A. Thompson, "The effects of InP grown by He-plasma assisted epitaxy on quantum-well intermixing," *IEEE Journal of Quantum Electronics,* vol. 37, pp. 426-429, Mar 2001.

[95] H. H. Tan and C. Jagadish, "Wavelength shifting in GaAs quantum well lasers by proton irradiation," *Applied Physics Letters,* vol. 71, pp. 2680-2682, Nov 3 1997.

[96] J. Z. Wan, J. G. Simmons, and D. A. Thompson, "Band gap modification in Ne^+-ion implanted $In_{1-x}Ga_xAs$/InP and $InAs_yP_{1-y}$/InP quantum well structures," *Journal of Applied Physics,* vol. 81, pp. 765-770, Jan 15 1997.

[97] L. Fu, P. Lever, H. H. Tan, C. Jagadish, P. Reece, and M. Gal, "Suppression of interdiffusion in InGaAs/GaAs quantum dots using dielectric layer of titanium dioxide," *Applied Physics Letters,* vol. 82, pp. 2613-2615, Apr 2003.

[98] S. J. Fancey, G. S. Buller, J. S. Massa, A. C. Walker, C. J. McLean, A. McKee, A. C. Bryce, J. H. Marsh, and R. M. DeLaRue, "Time-resolved photoluminescence microscopy of GaInAs/GaInAsP quantum wells intermixed using a pulsed laser technique," *Journal of Applied Physics,* vol. 79, pp. 9390-9392, Jun 15 1996.

[99] L. V. Dao, M. B. Johnston, M. Gal, L. Fu, H. H. Tan, and C. Jagadish, "Improved carrier collection in intermixed InGaAs/GaAs quantum wells," *Applied Physics Letters,* vol. 73, pp. 3408-3410, Dec 7 1998.

Chapter 6

[1] D. Kovalev, H. Heckler, G. Polisski, and F. Koch, "Optical properties of Si nanocrystals," *Physica Status Solidi B - Basic Research,* vol. 215, pp. 871-932, Oct 1999.

[2] P. Q. Zhao, D. S. Hu, and X. L. Wu, "Quantum confinement of Si nanosphere with radius smaller than 1.2 nm," *Chinese Physics Letters,* vol. 22, pp. 1492-1495, Jun 2005.

[3] M. Tabe, M. Kumezawa, Y. Ishikawa, and T. Mizuno, "Quantum confinement effects in Si quantum well and dot structures fabricated from ultrathin silicon-on-insulator wafers," *Applied Surface Science,* vol. 175, pp. 613-618, May 2001.

[4] S. A. Ding, M. Ikeda, M. Fukuda, S. Miyazaki, and M. Hirose, "Quantum confinement effect in self-assembled, nanometer silicon dots," *Applied Physics Letters,* vol. 73, pp. 3881-3883, Dec 1998.

[5] A. Hryciw, A. Meldrum, K. S. Buchanan, and C. W. White, "Effects of particle size and excitation spectrum on the photoluminescence of silicon nanocrystals formed by ion implantation," *Nuclear Instruments & Methods in Physics Research Section B-Beam Interactions with Materials and Atoms,* vol. 222, pp. 469-476, Aug 2004.

[6] D. L. Williamson, S. Roorda, M. Chicoine, R. Tabti, P. A. Stolk, S. Acco, and F. W. Saris, "On the nanostructure of pure amorphous-silicon," *Applied Physics Letters,* vol. 67, pp. 226-228, Jul 1995.

[7] O. Teschke, M. C. Goncalves, and F. Galembeck, "Etching technique for transmission electron-microscopy observation of nanostructure of visible luminescent porous silicon," *Applied Physics Letters,* vol. 63, pp. 1348-1350, Sep 1993.

[8] A. Hryciw, J. Laforge, C. Blois, M. Glover, and A. Meldrum, "Tunable luminescence from a silicon-rich oxide microresonator," *Advanced Materials,* vol. 17, pp. 845, Apr 2005.

[9] D. Kovalev, H. Heckler, M. Ben-Chorin, G. Polisski, M. Schwartzkopff, and F. Koch, "Breakdown of the k-conservation rule in Si nanocrystals," *Physical Review Letters,* vol. 81, pp. 2803-2806, Sep 1998.

[10] T. Muller, K. H. Heinig, and W. Moller, "Size and location control of Si nanocrystals at ion beam synthesis in thin SiO_2 films," *Applied Physics Letters,* vol. 81, pp. 3049-3051, Oct 2002.

[11] K. S. Zhuravlev, A. M. Gilinsky, and A. Y. Kobitsky, "Mechanism of photoluminescence of Si nanocrystals fabricated in a SiO_2 matrix," *Applied Physics Letters,* vol. 73, pp. 2962-2964, Nov 1998.

[12] Y. Kanemitsu, "Light-Emission from Porous Silicon and Related Materials," *Physics Reports-Review Section of Physics Letters,* vol. 263, pp. 1-91, Dec 1995.

[13] I. Kato, T. Matsumoto, and O. P. Agnihotri, "Photoluminescence from thermally oxidized hydrogenated amorphous silicon nanoball films fabricated by double-tubed-coaxial-line-type microwave plasma chemical vapor deposition system," *Japanese Journal of Applied Physics Part 1 - Regular Papers Short Notes & Review Papers,* vol. 40, pp. 6862-6867, Dec 2001.

[14] S. Nihonyanagi and Y. Kanemitsu, "Enhanced luminescence from electron-hole droplets in silicon nanolayers," *Applied Physics Letters,* vol. 85, pp. 5721-5723, Dec 2004.

[15] J. S. Biteen, D. Pacifici, N. S. Lewis, and H. A. Atwater, "Enhanced radiative emission rate and quantum efficiency in coupled silicon nanocrystal-nanostructured gold emitters" *Nano Letters,* vol. 5, pp. 2116-2116, Oct 2005.

[16] L. Van Dao, X. M. Wen, M. T. T. Do, P. Hannaford, E. C. Cho, Y. H. Cho, and Y. D. Huang, "Time-resolved and time-integrated photoluminescence analysis of state filling and quantum confinement of silicon quantum dots," *Journal of Applied Physics,* vol. 97, 013501, Jan 2005.

[17] R. Tomasiunas, J. Moniatte, I. Pelant, P. Gilliot, and B. Honerlage, "Femtosecond dephasing in porous silicon," *Applied Physics Letters,* vol. 68, pp. 3296-3298, Jun 1996.

[18] F. Trojanek, K. Neudert, P. Maly, K. Dohnalova, and I. Pelant, "Ultrafast photoluminescence in silicon nanocrystals studied by femtosecond up-conversion technique," *Journal of Applied Physics,* vol. 99, 116108, Jun 2006.

[19] L. Van Dao and P. Hannaford, "Femtosecond nonlinear coherence spectroscopy of carrier dynamics in porous silicon," *Journal of Applied Physics,* vol. 98, 083508, Oct 2005.

[20] J. P. R. Wells, P. J. Phillips, N. Tomozeiu, F. Habraken, and J. I. Dijkhuis, "Infrared transient grating and photon echo spectroscopy of oxygen vibrational modes in amorphous silicon thin films," *Physical Review B,* vol. 68, 115207, Sep 2003.

[21] J. Moniatte, B. Honerlage, R. Levy, R. Tomasiunas, and I. Pelant, "Femtosecond dephasing in porous silicon," *Thin Solid Films,* vol. 297, pp. 135-137, Apr 1997.

[22] S. Miura, T. Nakamura, M. Fujii, M. Inui, and S. Hayashi, "Size dependence of photoluminescence quantum efficiency of Si nanocrystals," *Physical Review B,* vol. 73, Jun 2006.

[23] J. P. R. Wells, R. E. I. Schropp, L. F. G. van der Meer, and J. I. Dijkhuis, "Ultrafast vibrational dynamics and stability of deuterated amorphous silicon," *Physical Review Letters,* vol. 89, 125504, Sep 2002.

[24] G. Conibeer, M. Green, R. Corkish, Y. Cho, E. C. Cho, C. W. Jiang, T. Fangsuwannarak, E. Pink, Y. D. Huang, T. Puzzer, T. Trupke, B. Richards, A. Shalav, and K. L. Lin, "Silicon nanostructures for third generation photovoltaic solar cells," *Thin Solid Films,* vol. 511, pp. 654-662, Jul 2006.

[25] Y. Kanemitsu, M. Iiboshi, and T. Kushida, "Photoluminescence spectrum of a-Si/ SiO_2 and c-Si/ SiO_2 quantum wells," *Journal of Luminescence,* vol. 87-9, pp. 463-465, May 2000.

[26] N. Pauc, V. Calvo, J. Eymery, F. Fournel, and N. Magnea, "Electronic and optical properties of Si/SiO_2 nanostructures. II. Electron-hole recombination at the Si/SiO_2 quantum-well-quantum-dot transition," *Physical Review B,* vol. 72, Nov 2005.

[27] L. Van Dao, C. Lincoln, M. Lowe, and P. Hannaford, "Spectrally resolved femtosecond two-colour three-pulse photon echoes: Study of ground and excited state dynamics in molecules," *Journal of Chemical Physics,* vol. 120, pp. 8434-8442, May 2004.

[28] J. Y. Jeong, S. Im, M. S. Oh, H. B. Kim, K. H. Chae, C. N. Whang, and J. H. Song, "Defect versus nanocrystal luminescence emitted from room temperature and hot-implanted SiO_2 layers," *Journal of Luminescence,* vol. 80, pp. 285-289, Dec 1998.

[29] G. R. Lin, C. J. Lin, C. K. Lin, L. J. Chou, and Y. L. Chueh, "Oxygen defect and Si nanocrystal dependent white-light and near-infrared electroluminescence of Si-implanted and plasma-enhanced chemical-vapor deposition-grown Si-rich SiO_2," *Journal of Applied Physics,* vol. 97, 094306, May 2005.

[30] L. Khriachtchev, M. Rasanen, S. Novikov, and L. Pavesi, "Systematic correlation between Raman spectra, photoluminescence intensity, and absorption coefficient of silica layers containing Si nanocrystals," *Applied Physics Letters,* vol. 85, pp. 1511-1513, Aug 2004.

[31] C. G. Ahn, T. S. Jang, K. H. Kim, Y. K. Kwon, and B. Kang, "Size and interface state dependence of the luminescence properties in Si nanocrystals," *Japanese Journal of Applied Physics Part 1-Regular Papers Short Notes & Review Papers,* vol. 42, pp. 2382-2386, Apr 2003.

[32] S. Cheylan, R. G. Elliman, K. Gaff, and A. Durandet, "Luminescence from Si nanocrystals in silica deposited by helicon activated reactive evaporation," *Applied Physics Letters,* vol. 78, pp. 1670-1672, Mar 2001.

[33] F. Iacona, G. Franzo, and C. Spinella, "Correlation between luminescence and structural properties of Si nanocrystals," *Journal of Applied Physics,* vol. 87, pp. 1295-1303, Feb 2000.

[34] S. Lee, Y. S. Shim, H. Y. Cho, D. Y. Kim, T. W. Kim, and K. L. Wang, "Optical and electrical properties of Si nanocrystals embedded in SiO_2 layers," *Japanese Journal of Applied Physics Part 1 - Regular Papers Short Notes & Review Papers,* vol. 42, pp. 7180-7183, Dec 2003.

[35] M. L. Brongersma, A. Polman, K. S. Min, E. Boer, T. Tambo, and H. A. Atwater, "Tuning the emission wavelength of Si nanocrystals in SiO_2 by oxidation," *Applied Physics Letters,* vol. 72, pp. 2577-2579, May 1998.

[36] F. Iacona, G. Franzo, V. Vinciguerra, A. Irrera, and F. Priolo, "Influence of the spatial arrangement on the quantum confinement properties of Si nanocrystals," *Optical Materials,* vol. 17, pp. 51-55, Jun-Jul 2001.

[37] C. Garcia, B. Garrido, P. Pellegrino, R. Ferre, J. A. Moreno, J. R. Morante, L. Pavesi, and M. Cazzanelli, "Size dependence of lifetime and absorption cross section of Si nanocrystals embedded in SiO_2," *Applied Physics Letters,* vol. 82, pp. 1595-1597, Mar 2003.

[38] B. G. Fernandez, M. Lopez, C. Garcia, A. Perez-Rodriguez, J. R. Morante, C. Bonafos, M. Carrada, and A. Claverie, "Influence of average size and interface passivation on the spectral emission of Si nanocrystals embedded in SiO_2," *Journal of Applied Physics,* vol. 91, pp. 798-807, Jan 2002.

[39] G. Allan, C. Delerue, and M. Lannoo, "Nature of luminescent surface states of semiconductor nanocrystallites," *Physical Review Letters,* vol. 76, pp. 2961-2964, Apr 1996.

[40] I. Vasiliev, J. R. Chelikowsky, and R. M. Martin, "Surface oxidation effects on the optical properties of silicon nanocrystals," *Physical Review B,* vol. 65, Mar 2002.

[41] M. Lopez, B. Garrido, C. Garcia, P. Pellegrino, A. Perez-Rodriguez, J. R. Morante, C. Bonafos, M. Carrada, and A. Claverie, "Elucidation of the surface passivation role on the photoluminescence emission yield of silicon nanocrystals embedded in SiO_2," *Applied Physics Letters,* vol. 80, pp. 1637-1639, Mar 2002.

[42] I. Sychugov, R. Juhasz, J. Valenta, A. Zhang, P. Pirouz, and J. Linnros, "Light emission from silicon nanocrystals: Probing a single quantum dot," *Applied Surface Science,* vol. 252, pp. 5249-5253, May 2006.

[43] I. Sychugov, R. Juhasz, A. Galeckas, J. Valenta, and J. Linnros, "Single dot optical spectroscopy of silicon nanocrystals: low temperature measurements," *Optical Materials,* vol. 27, pp. 973-976, Feb 2005.

[44] S. Raymond, S. Fafard, P. J. Poole, A. Wojs, P. Hawrylak, C. Gould, A. Sachrajda, S. Charbonneau, D. Leonard, R. Leon, P. M. Petroff, and J. L. Merz, "State-filling and magneto-photoluminescence of excited states in InGaAs/GaAs self-assembled quantum dots," *Superlattices and Microstructures,* vol. 21, pp. 541-558, 1997.

[45] Y. M. Park, Y. J. Park, K. M. Kim, J. C. Shin, J. D. Song, J. I. Lee, and K. H. Yoo, "State filling phenomena in modulation-doped InAs quantum dots," *Journal of Crystal Growth,* vol. 271, pp. 385-390, Nov 15 2004.

[46] K. Luterova, K. Dohnalova, F. Trojanek, K. Neudert, P. Gilliot, B. Honerlage, P. Maly, and I. Pelant, "Porous silicon grains in SiO_2 matrix: Ultrafast photoluminescence and optical gain," *Journal of Non-Crystalline Solids,* vol. 352, pp. 3041-3046, Aug 2006.

[47] J. Kudrna, P. Maly, F. Trojanek, I. Pelant, J. Kocka, A. Poruba, S. Surendran, and J. Jiricka, "Ultrafast carrier dynamics in wide gap hydrogenated amorphous silicon," *Journal of Luminescence,* vol. 80, pp. 435-438, Dec 1998.

[48] T. Matsumoto, T. Futagi, H. Mimura, and Y. Kanemitsu, "Ultrafast decay dynamics of luminescence in porous silicon," *Physical Review B,* vol. 47, pp. 13876-13879, May 1993.

[49] M. Dovrat, Y. Goshen, J. Jedrzejewski, I. Balberg, and A. Sa'ar, "Radiative versus nonradiative decay processes in silicon nanocrystals probed by time-resolved photoluminescence spectroscopy," *Physical Review B,* vol. 69, 155311, Apr 2004.

[50] L. Pavesi and M. Ceschini, "Stretched-Exponential Decay of the Luminescence in Porous Silicon," *Physical Review B,* vol. 48, pp. 17625-17628, Dec 1993.

[51] J. Linnros, N. Lalic, A. Galeckas, and V. Grivickas, "Analysis of the stretched exponential photoluminescence decay from nanometer-sized silicon crystals in SiO_2," *Journal of Applied Physics,* vol. 86, pp. 6128-6134, Dec 1999.

[52] L. Pavesi, "Influence of dispersive exciton motion on the recombination dynamics in porous silicon," *Journal of Applied Physics,* vol. 80, pp. 216-225, Jul 1996.

[53] J. Kudrna, P. Bartosek, F. Trojanek, I. Pelant, and P. Maly, "Time-resolved photoluminescence in porous silicon," *Journal of Luminescence,* vol. 72-4, pp. 347-349, Jun 1997.

[54] A. V. Andrianov, D. I. Kovalev, V. B. Shuman, and I. D. Yaroshetskii, "Time-Resolved Photoluminescence of Porous Silicon," *Semiconductors,* vol. 27, pp. 71-73, Jan 1993.

[55] D. I. Kovalev, I. D. Yaroshetzkii, T. Muschik, V. Petrovakoch, and F. Koch, "Fast and slow visible luminescence bands of oxidized porous Si," *Applied Physics Letters,* vol. 64, pp. 214-216, Jan 1994.

[56] L. Tsybeskov, J. V. Vandyshev, and P. M. Fauchet, "Blue Emission in Porous Silicon - Oxygen-Related Photoluminescence," *Physical Review B,* vol. 49, pp. 7821-7824, Mar 1994.

[57] C. I. Harris, M. Syvajarvi, J. P. Bergman, O. Kordina, A. Henry, B. Monemar, and E. Janzen, "Time-Resolved Decay of the Blue Emission in Porous Silicon," *Applied Physics Letters,* vol. 65, pp. 2451-2453, Nov 1994.

[58] A. Kux, D. Kovalev, and F. Koch, "Time-delayed luminescence from oxidized porous silicon after ultraviolet excitation," *Applied Physics Letters,* vol. 66, pp. 49-51, Jan 1995.

[59] A. G. Cullis, L. T. Canham, and P. D. J. Calcott, "The structural and luminescence properties of porous silicon," *Journal of Applied Physics,* vol. 82, pp. 909-965, Aug 1997.

[60] A. Yariv, *Quantum Electronnics*, 3rd ed. New York: Wiley-Interscience, 1989.

[61] A. Vagov, V. M. Axt, and T. Kuhn, "Impact of pure dephasing on the nonlinear optical response of single quantum dots and dot ensembles," *Physical Review B,* vol. 67, 115338, Mar 2003.

[62] L. Van Dao, M. Lowe, P. Hannaford, H. Makino, T. Takai, and T. Yao, "Femtosecond three-pulse photon echo and population grating studies of the optical properties of CdTe/ZnSe quantum dots," *Applied Physics Letters,* vol. 81, pp. 1806-1808, Sep 2002.

[63] D. Kovalev, H. Heckler, G. Polisski, J. Diener, and F. Koch, "Optical properties of silicon nanocrystals," *Optical Materials,* vol. 17, pp. 35-40, Jun-Jul 2001.

[64] P. Machnikowski and L. Jacak, "Resonant nature of phonon-induced damping of Rabi oscillations in quantum dots," *Physical Review B,* vol. 69, 193302, May 2004.

[65] N. H. Bonadeo, J. Erland, D. Gammon, D. Park, D. S. Katzer, and D. G. Steel, "Coherent optical control of the quantum state of a single quantum dot," *Science,* vol. 282, pp. 1473-1476, Nov 1998.

[66] A. I. Tartakovskii, M. N. Makhonin, J. Cahill, D. M. Whittaker, J. P. R. Wells, A. M. Fox, D. J. Mowbray, M. S. Skolnick, M. J. Steer, K. M. Groom, and M. Hopkinson, "Precise measurement of the fraction of charged dots in self-assembled quantum dot ensembles using ultrafast pump-probe techniques," *Applied Physics Letters,* vol. 85, pp. 2226-2228, Sep 20 2004.

[67] L. Van Dao, C. Lincoln, M. Lowe, and P. Hannaford, "Spectrally resolved two-colour three-pulse photon echo studies of vibrational dynamics of molecules," *Physica B - Condensed Matter,* vol. 327, pp. 123-128, Mar 2003.

[68] G. R. Fleming, B. S. Prall, M. Yang, and D. Y. Parkinson, "Two-colour three-pulse photon echo spectroscopy," *Abstracts of Papers of the American Chemical Society,* vol. 225, pp. U460-U460, Mar 2003.

[69] Y. Kanemitsu and S. Okamoto, "Photoluminescence from Si/ SiO_2 single quantum wells by selective excitation," *Physical Review B,* vol. 56, pp. R15561-R15564, Dec 1997.

[70] V. I. Klimov and D. W. McBranch, "Femtosecond 1P-to-1S electron relaxation in strongly confined semiconductor nanocrystals," *Physical Review Letters,* vol. 80, pp. 4028-4031, May 1998.